TOPOLOGY OPTIMIZATION OF STEEL SHEAR FUSES TO RESIST BUCKLING

Javier A. Avecillas

Thesis submitted to the Faculty of the
Virginia Polytechnic Institute and State University
in partial fulfillment of the requirements for the degree of

Master of Science
in
Civil Engineering

Matthew R. Eatherton, Chair
Finley A. Charney
Ioannis Koutromanos

November 27, 2018
Blacksburg, Virginia

Keywords: Structural Fuses, Topology Optimization, Genetic Algorithms, Hysteretic Dampers, Seismic Energy Dissipation, Finite Element Analysis

Topology Optimization of Steel Shear Fuses to Resist Buckling

Javier A. Avecillas

ABSTRACT

Shear-acting structural fuses are steel plates with cutouts subjected to in-plane lateral displacements during extreme loading events such as earthquakes, that dissipate energy through localized shear or flexural yielding mechanisms. Although previous studies have reported that fuses with specific geometry can develop a stable hysteretic behavior, their small thickness makes them prone to buckling, reducing strength and energy dissipation capacity.

In this work, topology optimization using genetic algorithms is performed to find optimized shapes for structural fuses with a square domain and constant thickness. The objective function uses the fuse's shear buckling load (V_B) obtained from a 3D linear buckling analysis, and shear yield load (V_Y) obtained from a material nonlinear, but geometrically linear 2D plane-stress analysis. The two analyses are shown to be computationally efficient and viable for use in the optimization routine. The variations $V_Y/V_B = 0.1, 0.2, 0.3$ are investigated considering a target volume equal to 30%, 40% and 50% the fuse's original volume. A new set of optimized topologies are obtained, interpreted into smooth shapes, and evaluated using finite elements analyses with models subjected to monotonic and cyclic displacements histories. It was found that the drift angle when out-of-plane buckling occurs can be controlled using the V_Y/V_B ratio, with optimized topologies buckling at drift angles (when subjected to a cyclic displacement protocol) as large as 9% as compared to 6% for previously studied fuses.

Topology Optimization of Steel Shear Fuses to Resist Buckling

Javier A. Avecillas

GENERAL AUDIENCE ABSTRACT

Shear-acting structural fuses are steel plates with cutouts that dissipate energy during extreme loading events such as earthquakes. These structural fuses have a fixed edge and an opposing edge subjected to in-plane lateral displacements. Although previous studies have reported that fuses with specific geometry have a good cyclic performance, their small thickness makes them prone to bend or buckle, reducing strength and energy dissipation capacity.

Considering a structural fuse with a square domain and constant thickness, a mathematical method called topology optimization is implemented to optimize the distribution of material with the goal of controlling the amount of yielding in the structural fuse before it buckles. The optimization routine uses the fuse's shear buckling capacity (V_B) and shear yield strength (V_Y) obtained from relative simple and computationally inexpensive procedures that are also valid to characterize the potential for buckling in a structural fuse. The variations $V_Y/V_B = 0.1, 0.2, 0.3$ are investigated considering a target volume equal to 30%, 40% and 50% the fuse's original volume. A set of optimized topologies are interpreted into smooth shapes and evaluated using finite elements analyses. It was found that the drift angle when out-of-plane buckling occurs can be controlled by using the V_Y/V_B ratio, with optimized topologies buckling at drift angles (when subjected to a cyclic displacement protocol) as large as 9% as compared to 6% for previously studied fuses.

Acknowledgment

I would like to express my total gratitude to my advisor, Dr. Matthew Eatherton for his invaluable guidance over the past two years. His dedication towards research have made me a better academic and technical writer. I would also like to thank to my committee members Dr. Finley Charney and Dr. Ioannis Koutromanos for their constant support throughout the project.

Thanks to The National Secretariat of Higher Education, Science, Technology, and Innovation of Ecuador (SENESCYT) for the support provided through its graduate fellowship program.

Some aspects of this work were supported by the National Science Foundation under Grant No. CMMI-1453960. Any opinions, findings, and conclusions or recommendations expressed in this material are those of the authors and do not necessarily reflect the views of the National Science Foundation or other sponsors.

Finally, I would like to thank my parents for their care and incommensurable love throughout my life and education.

Contents

List of Figures

List of Tables

Chapter 1

Introduction

1.1 Background

A large amount of energy is imparted to a structure during a seismic event. One of the most common design approaches in structural earthquake engineering relies on letting some structural elements undergo inelastic deformations and thus dissipate energy. The benefit of including dissipative devices is based on three key concepts. Firstly, the presence of structural fuses contributes to the increment of hysteretic damping thereby improving the energy dissipation of the structure and reducing its peak drifts. Secondly, since an earthquake acts more like an applied displacement than an applied force, structural fuses provide the inelastic deformation capacity. This ability stems from their highly ductile behavior i.e. they can withstand large inelastic deformations without fracture. Lastly, the structures repairability is enhanced by concentrating damage in the structural fuse and thus limiting the inelastic deformations in the rest of the structure. Therefore, implementing structural fuses in a way that they can be replaced after a big earthquake reduces repair costs and business downtime.

After Kelly et al. (1972) put forward the concept of energy dissipation with metal

energy-dissipation devices, many theoretical and experimental studies have been carried out on structural fuses. Overall, we might categorize structural fuses into three groups: axial acting (e.g. buckling restrained braces), flexural acting (e.g. plastic flexural hinges) and shear acting. Steel shear fuses fall into the last category, because they capitalize on relative shear deformations of two of its edges to accommodate the input seismic energy. In addition, structural fuses are widely used in the seismic design of structures because of their low cost and stable energy dissipation capacity (Deng et al., 2015).

There are two typical approaches to design seismic force resisting systems that rely on ductile elements subjected to shear deformations. The first methodology is shear buckling with tension yielding along the diagonal (Berman and Bruneau, 2003), used in the design of conventional steel shear walls. The second approach is shear yielding of a solid plate, used in the design of conventional eccentrically braced frames (Popov and Engelhardt, 1988). More recently, another option has been explored which is steel plates with cutouts that create local yielding mechanisms. Figure 1.1 illustrates how a structural fuse with cutouts could be implemented in a self-centering steel braced frame (Eatherton et al., 2014), in an eccentrically braced frame, as the yielding mechanism in a hybrid coupled shear wall (Fortney et al., 2007) or used in a damper configuration.

However, each system also has a number of drawbacks. For instance, steel shear walls have challenges related to buckling (Driver et al., 1998), the link in a eccentrically braced frame is prone to fracture (Clifton et al., 2011), and steel shear fuses may be prone to buckling (Ma et al., 2010).

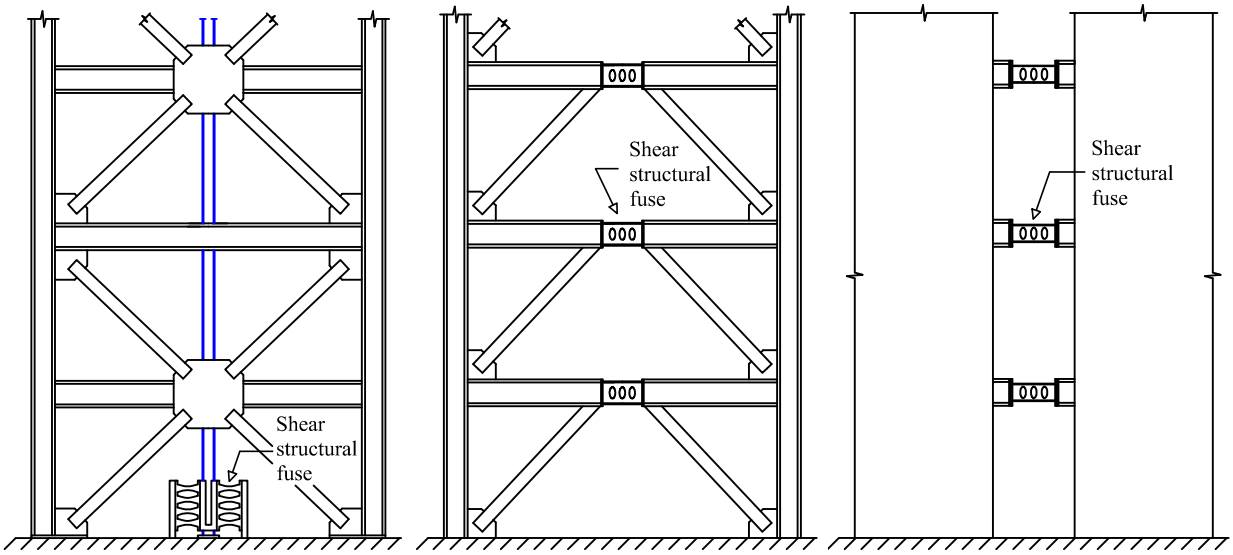

(a) Self-centering steel braced frame (b) Eccentrically braced frames (c) Hybrid coupled shear wall

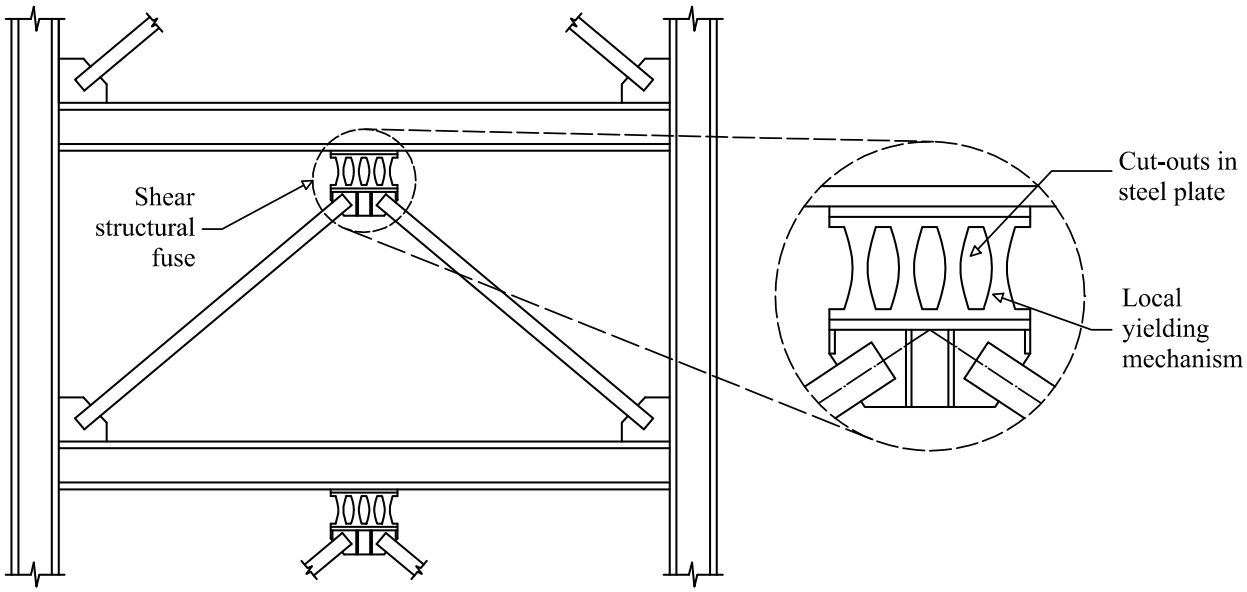

(d) Damper configuration of a structural fuse with cutouts

Figure 1.1: Seismic force resisting systems using steel shear fuses

In a shear structural fuse, a transformation of the global shear deformations into local yielding mechanisms that are highly ductile and dissipate energy is desirable. Nevertheless,

several factors are known to affect this energy exchange, one of the most significant being out-of-plane instabilities. Although shear buckling is not synonymous with failure, it does reduce the energy dissipation capacity of the fuse. Conversely, by controlling buckling it is expected that the structural fuse exhibits a full hysteretic behavior.

As far as developing buckling resistant geometries for shear structural fuses, different solutions have been proposed. Some authors have tried to use multilayer fuses as an alternative to the adoption of significantly thicker plates (He et al., 2016). Such solutions are often associated with the use of low yield stress materials, which are characterized by a significant deformation capacity (De Matteis et al., 2012). Alternatively, Deng et al. (2015) suggested the inclusion of an additional outer stiffener similar to a metal case which helps to mitigate the buckling phenomenon. Also, there are studies oriented toward modifying the shape of the structural fuse to improve its performance. For instance, Ma et al. (2010) described a fairly ductile behavior of a structural fuse with diamond-shape openings that create a butterfly-shape link, similar to the illustrated in Figure 1.1 (d). In addition, a stable hysteretic performance of a ring-shaped structural fuse conceived to prevent shear buckling was reported by Egorova et al. (2014). Similarly, shape optimization analysis were carried out by Liu and Shimoda (2013) and Ghabraie et al. (2010) where the optimized structural fuse was related to a particular shape with the highest deformation capability and an even stress distribution, respectively.

One of the primary reasons for a structural fuse to present a poor hysteretic performance is the presence of out-of-plane instabilities. While implementing cutout patterns (e.g. butterfly-shaped) and the use of engineering concepts (e.g. ring-shaped) have helped to dispose of unnecessary material that could originate buckling, topology optimization procedures have not used an objective function to directly address the buckling problem. Therefore, this research will fill the need for structural fuses with new cutouts that were optimized to help the fuse to resist buckling.

1.2 Research motivation

The purpose of this thesis is to use a topology optimization procedure to enhance the buckling resistant capacity of a structural fuse with cutouts. This need arises from previous topology optimization studies, where the researchers have tended to develop objective functions to improve some mechanical and hysteric properties of the fuses such as: maximum in-plane stiffness, cumulative equivalent plastic strain, stress distribution, etc. rather than treating the buckling problem in detail.

The optimized geometries resulting from these objective functions often have a large width-to-thickness ratio, so that buckling is expected to occur before yielding. An out-of-plane instability is not preferable because it degrades the strength and energy dissipation capacity of the fuse. Hence, interest in enhancing the buckling resistance of steel structural fuses has greatly increased in recent years. The influence of different materials, cut-outs and additional stiffeners has been widely studied by various researchers.

Additionally, none of the previous topology optimization studies explicitly consider the topology of the fuse as the main source to inhibit out-of-plane deformations. Many of the topological studies including shear fuses do not consider 3D elements for the finite element formulation, and if they do, it is very likely that all out-of-plane degrees of freedom were restrained. In conclusion, the slenderness of these dissipative devices in conjunction with the lack of studies about using the shear buckling load as one of the variables of the objective function, have set the staring points for this study.

1.3 Scope and objective

Given the fact that out-of-plane instabilities compromise the cyclic performance of a steel shear fuse, this research aims to develop and use a new objective function in conjunction with a topology optimization algorithm to obtain new cutout patterns for a square domain of

constant thickness that help a structural fuse to resist buckling. The major aspects covered in this study are detailed as follows:

1. The development of an objective function that uses the shear buckling load of the structural fuse as one of its variables. In addition, since the ideal scenario is to have a fuse yielding under shear deformations, the shear yield load of the fuse is considered as the second variable of the objective function.

2. The implementation of the objective function in a form that could be used with topology optimization algorithms. This phase could be expanded in four steps:

   (a) Use MATLAB to represent a given topology with a binary input vector considering the two possible scenarios: material or void.

   (b) Check whether the vector represents a physical admissible geometry.

   (c) Use a finite element software to perform a linear buckling analysis and a nonlinear static analysis.

   (d) Use MATLAB to process all the output information to determine the value of the variables involved in the calculation of the objective function

3. Perform a sensitivity analysis to select the best genetic algorithm parameters to use in the optimization routine.

4. Run the topology optimization algorithm for a square domain with constant thickness.

5. Due to the free forms that naturally occur after using the above procedure, an interpretation or smoothing analysis of the different shapes has to be done in order to maintain simplicity of the geometry and in consequence to reduce its fabrication cost.

6. Finite element models of the new structural fuses including geometric and material nonlinearities are analyzed as subjected to monotonic and cyclic loading, to evaluate their yielding mechanism and hysteretic behavior.

1.4 Organization of thesis

This thesis document is organized in the following chapters:

- Chapter 1: Introduces motivation for this research and defines the scope of this work.
- Chapter 2: Reviews fundamental literature on past experimental and computational studies of steel shear fuses.
- Chapter 3: Defines and validates the proposed objective function to be implemented in a topology optimization algorithm.
- Chapter 4: Presents the implementation of the proposed objective function in a topology optimization algorithm.
- Chapter 5: Introduces the genetic algorithm as an optimization technique.
- Chapter 6: A sensitivity analysis of the different genetic operators involved in the optimization algorithm.
- Chapter 7: Topology optimization algorithm for a square domain with constant thickness.
- Chapter 8: Monotonic pushover analysis of the optimized structural fuses.
- Chapter 9: Cyclic analysis of the optimized topologies.
- Chapter 10: Conclusions reached throughout this research and recommends future work.

Chapter 2

Literature Review

This section summarizes three important philosophies implemented by different authors regarding the improvement of the hysteretic performance of a structural fuse. The first approach considers the implementation of additional steel stiffeners necessary to mitigate or completely avoid the detrimental effects caused by shear buckling. The second approach involves the use of cutout patterns to dispose of the unnecessary material that could trigger out-of-plane deformations, and thus resulting in a better distribution of inelastic strains within the fuse. Lastly, the third methodology uses topology optimization techniques to maximize or minimize the value of an objective function and therefore improving the fuses response to cyclic loading. A more detailed explanation of the previously mentioned philosophies is presented in the following paragraphs.

2.1 Steel shear fuses with additional stiffeners

Several efforts have been made in order to prevent out-of-plane buckling of steel shear fuses. A relatively new kind of buckling restrained shear panel damper (BRSPD) was proposed by Deng et al. (2015). Figure 2.1 illustrates the damper, which consists of two main

parts: an inner core which acts as the energy dissipation system and two exterior restraining plates which should be stiff enough to prevent any instability in the system. Although none of the stiffeners are welded to the energy dissipation plate, they clamp the energy dissipation core with bolts on both sides to prevent out-of-plane buckling.

Quasi-static tests of five specimens were carried out to investigate the performance of the BRSPDs. The tests were intended to illustrate the influence of variables such as: width-to-height ratio, strength of the restraining plates and the gaps between them and the energy dissipation plate. The tests showed that restraining plates with adequate stiffness and strength can effectively restrain the out-of-plane buckling of the energy dissipation plate (Deng et al., 2015). One of the main challenges associated with this novel damper are the gaps between the external restraining plates and the energy dissipation plate, since a too large gap will lead to worse hysteretic performances of the BRSPD.

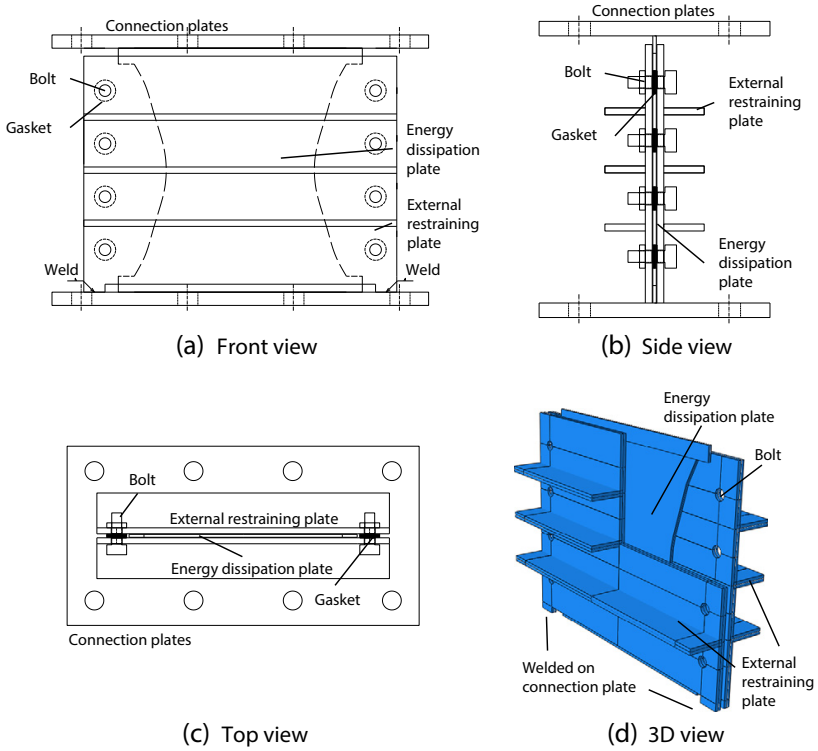

Figure 2.1: Buckling restrained shear panel damper [From (Deng et al., 2015)]

Another similar system to the previously described was proposed by De Matteis et al. (2014), who named this new energy dissipation system as the "Buckling Inhibited Shear Panel" (BIP). From Figure 2.2 we can notice that the BIP system bases its ductile mechanism in the yielding of a thin steel core plate, while additional exterior stiffeners prevent out-of-plane displacements but without any type of interactions in terms of membrane strains. Moreover, two technologies for the inhibition of buckling phenomena are presented. The former restrains the out-of-plane displacements for the plate portions that are most likely to be involved in the development of the first buckling modes i.e. the diagonals of the plate. The latter inhibits the out-of-plane deformations of the whole system (De Matteis et al., 2014). Finally, the authors carried out experimental tests were the two different buckling restraining technologies were tested. Through a comparison of the results from the buckling inhibited plates with those results from the plates without buckling restraining devices, it is possible to observe the increase in energy dissipation capacity that is possible with the proposed technologies.

On the other hand, the authors also noted some critical issues that can arise when the system is assembled with little accuracy. The most critical problem involves the gap between the core and the exterior stiffeners. This variable plays a significant role when thin plates are used as a core. In fact, the response of the system for low-medium shear strain demands could be negatively affected by such a gap in terms of dissipative capacity. In addition, when thicker plates and smaller gaps are applied, the performance of the system could be negatively influenced by the out-of-plane deformability of the restraining elements.

(a) Partially Buckling Inhibited Panel (p-BIP) (b) Totally Buckling Inhibited Panel (t-BIP)

Figure 2.2: Buckling Inhibited Panels [From (De Matteis et al., 2014)]

2.2 Steel shear fuses with cutout patterns

One of the philosophies to prevent or delay buckling in a fuse under shear deformations is to use cut-out patterns. Hence, Egorova et al. (2014) proposed a ring shaped steel plate shear wall (RS-SPSW) which mainly consists in a regular pattern of ring-shaped portions of steel connected by diagonal links (Figure 2.3). When subjected to in-plane lateral displacements, the rings compression diagonal shortens a similar amount as the tension diagonal elongates, thus eliminating the slack problem in the perpendicular direction to the tension field action. The behavior of a ring deforming into an ellipse is the main mechanism by which the RS-SPSW resists out-of-plane instabilities. Because of the unique features of the ring's mode of distortion, the load deformation response of the resulting RS-SPSW system can exhibit full hysteretic behavior and possess greatly improved stiffness relative to thin unstiffened SPSW (Egorova et al., 2014).

Regarding experimental testing, the authors reported that the RS-SPSW specimens were capable of developing plastic hinging of the rings and nearly full hysteretic behavior. Nevertheless, shear buckling of the RS-SPSW panels was also present after large inelastic shear distortion angles. After analyzing all the specimens' final configuration and hysteric response, it was concluded that global shear buckling was related to plate slenderness and

the lateral torsional buckling of the rings was associated to the ring slenderness.

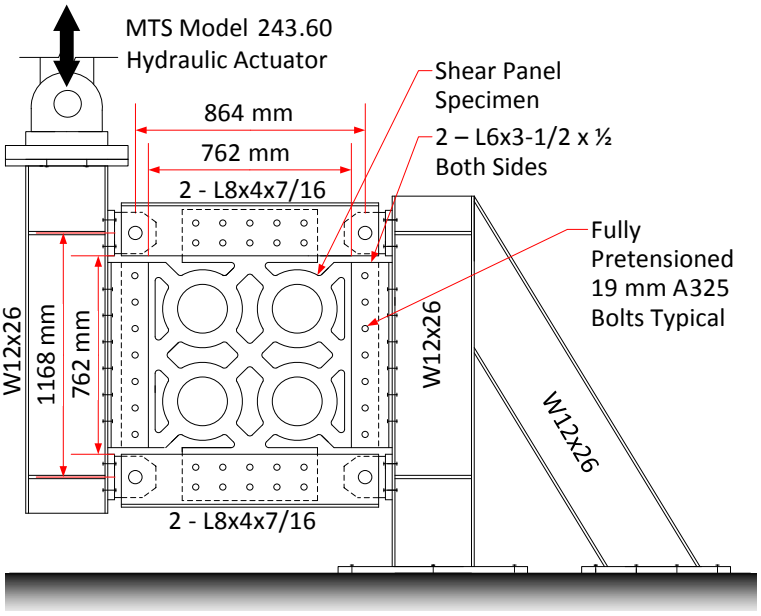

Figure 2.3: Side view of the experimental setup for a RS-SPSW [From (Egorova et al., 2014)]

Another study involving cutout patterns is reported by Ma et al. (2010). This research investigated two types of shear fuses: one with rectangular links named the slit fuse, and the butterfly-shape fuse with diamond-shape openings. Although there was not an specific criterion to determine the geometric dimensions of the slit damper, the logic behind the butterfly-shaped fuse was to initiate yielding at quarter points and then spread the inelastic deformations over the full length. The experimental setup for a slit fuse and a butterfly-shape fuse are illustrated in Figure 2.4.

In terms of experimental results, all the tested fuses demonstrated fairly ductile behavior. More specifically, they presented a full load-deformation hysteretic response at least up to 5% shear deformations, followed by pinched behavior, and eventually fracture due to low-cycle fatigue at a shear deformation of 20%, or 30% for the more ductile butterfly fuses (Ma et al., 2010).

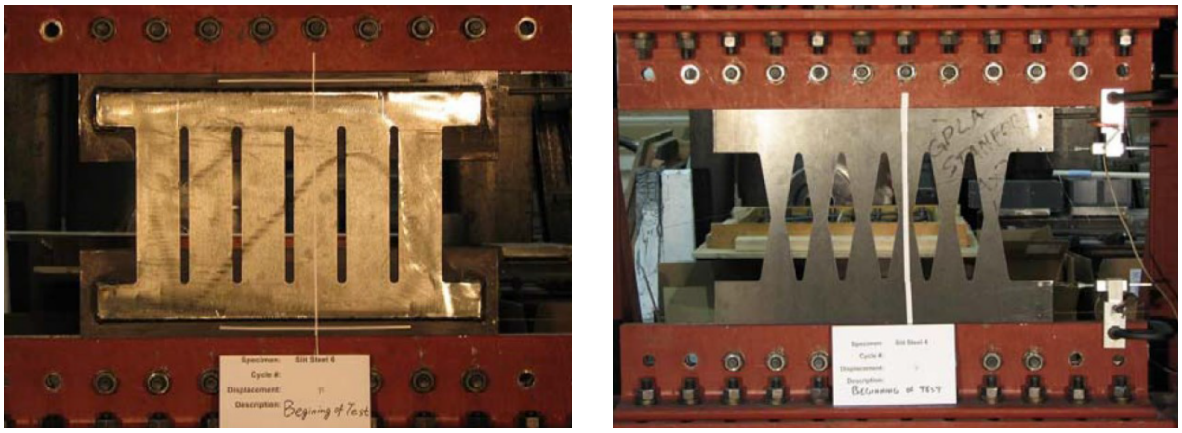

(a) Slit fuse

(b) Butterfly fuse

Figure 2.4: Structural fuses with cutout patterns [From (Ma et al., 2010)]

2.3 Topology optimization of structural fuses

Although the development of shapes for seismic shear fuses based on the engineering experience of designers has been successful, the improvement of the hysteretic performance of these steel dampers through topology optimization techniques has also been investigated. Shapes have been obtained depending on the optimization algorithm and additional constraints, thus the concept of mathematically maximize or minimize an objective function within a design domain has become very useful for designing a structural fuse. Minimizing the worst cumulative equivalent plastic strain (Liu and Shimoda, 2013), maximizing the dissipated total plastic energy (Ghabraie et al., 2010), increasing the in-plane stiffness (He et al., 2016), improving the low cycle fatigue performance (Deng et al., 2014) and producing an even stress state (Xu et al., 2011; He et al., 2016), are some of the most used optimization criteria. Two representative studies of the previously mentioned optimization procedures are analyzed in the following paragraphs.

2.3.1 Steel shear fuses with a maximized total plastic strain energy dissipation

It has been concluded by Ghabraie et al. (2010) that one of the most desirable characteristics for a seismic fuse is to have a reasonable resistance against low-cycle fatigue, performance that can be achieved by reaching an even stress distribution on the fuse. Regarding low-cycle fatigue, the current design standard in the United States requires devices to undergo five fully reversed cycles at maximum earthquake device displacement (ASCE, 2010). Therefore, these researchers used the concept of maximizing the total plastic strain energy dissipation through a Bi-directional Evolutionary Structural Optimization (BESO) topology optimization technique to optimize the low-cycle fatigue performance of previously tested slit dampers.

Moreover, it has been demonstrated that the stress concentration noticeable in the initial straight slit design has been eliminated in the optimum design (Figure 2.5). According to further computational and numerical analyses, they concluded that this even stress distribution can significantly improve the behavior of the damper under fatigue. Since the finite element model used in the optimization process was not capable of predicting failure and fatigue of the design, the new optimized dampers were fabricated and put under cyclic tests. Under identical test setup and load history, the optimized fuses dissipated 37% more energy per unit volume compared to the previously tested dampers, and significantly delayed low-cycle fatigue (Ghabraie et al., 2010).

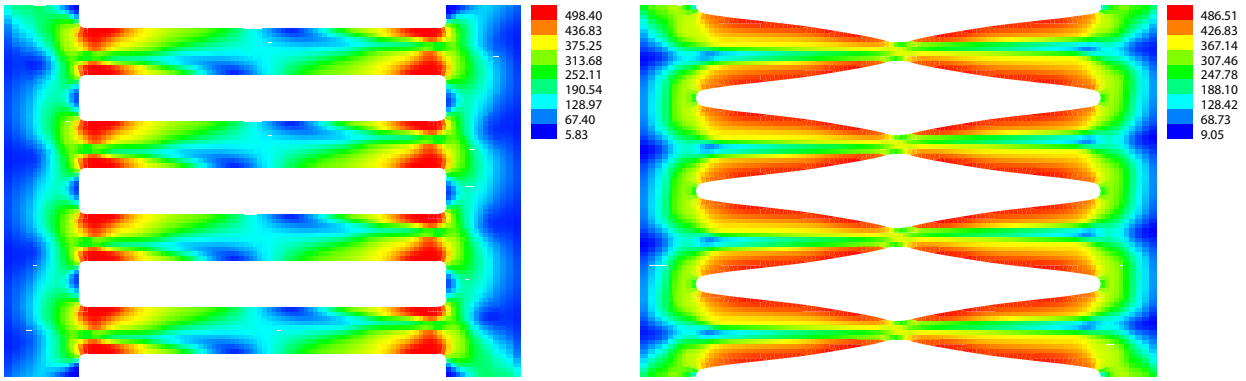

(a) Initial design. (b) Optimal design.

Figure 2.5: Even stress distribution in an optimized slit damper [From (Ghabraie et al., 2010)]

2.3.2 Steel shear fuses with maximum stiffness and full stress state

Noticing the disadvantages of a higher yield stress and inadequate adjustability, He et al. (2016) conducted a research study on the topology optimization of a combined steel plate damper based on the combination of low yield point steel plates and common steel plates. Three types of combined plate dampers with new perforated shapes are proposed, and the specific forms include an interior, boundary, and ellipse perforations (Figure 2.6). The objective of the optimization process was to maximize the in-plane stiffness of the damper and at the same time to produce an even stress distribution on the plate. Various combined steel plate dampers were analyzed by finite element simulation and the results indicated that those dampers with interior and boundary perforations have a larger initial stiffness, a better hysteretic behavior and no stress concentration (He et al., 2016). Additionally, it was reported that the energy-dissipation capacity of all the three dampers is close at the initial stage and it keeps growing gradually with the increment of deformations.

Although the buckling problem was not explicitly studied, it was stated that the ellipse optimized model was proposed to overcome the deficiency of out-of-plane instabilities. Moreover, and as a standing feature, it is reported that at later stages of loading the equiv-

alent damping ratio of the ellipse optimized model grows faster than the interior optimized model, which is directly related to a rapid increase in energy dissipation capacity. Nevertheless, the main flaw reported about this particular shape is that this optimized damper may lead to device failure due to stress concentration, and in consequence it is not recommended for normal structures.

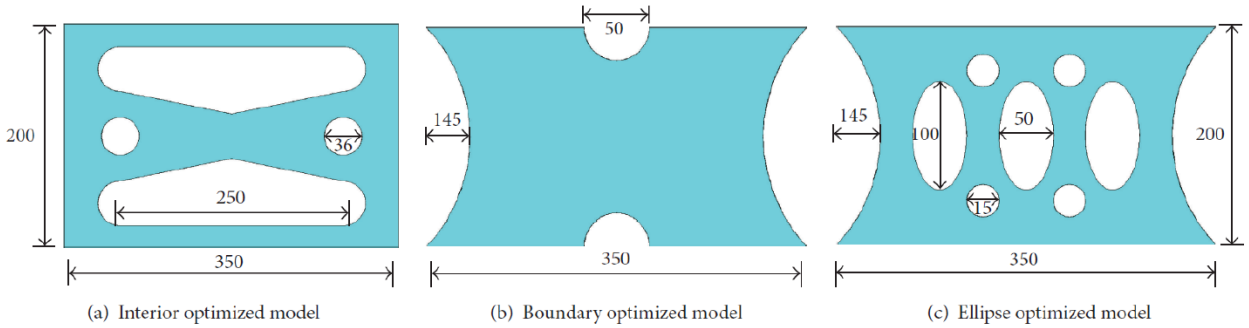

Figure 2.6: Final optimized shape of low yield point steel plate damper [From (He et al., 2016)]

Chapter 3

Resisting Buckling Through Topology Optimization

3.1 Development of an objective function

The purpose of topology optimization is to find the optimum distribution of material within a design space under a given set of loads, boundary conditions and performance targets. Besides the well-known influence of the optimization algorithm in the final result, it is also reasonable to say that the success of this mathematical procedure depends on the efficiency of the implemented objective function and applied constraints.

Along the same lines, the proposed objective function should make use of computationally inexpensive tools. Despite the fact that running a full 3D model with material and geometric non linearity through cyclic loading to directly characterize the buckling behavior of the fuse or the fullness of its cyclic hysteretic loops is the most accurate procedure, it is not be appropriate for topology optimization. This research will rely on relative simple and computationally inexpensive procedures that are also valid to characterize the potential for buckling in a structural fuse.

Since the main goal of this research is to develop a new shape to prevent buckling in the structural fuse, it would be necessary to have a topology with an elastic shear buckling load V_B, larger than the shear yield load V_Y. Expressed in other words, the basic optimization procedure would be minimize the ratio V_Y/V_B for a given volume of material, thus delaying buckling while the shear fuse is yielding. Nevertheless, this condition is not enough as an objective function because results in V_Y approaching to zero.

To solve the problem of producing optimized topologies without bearing capacity, a second approach to guarantee shear yielding in a structural fuse is proposed. The new objective is to force V_Y/V_B to equal a target value $\overline{V_Y}/\overline{V_B}$ while maximizing strength. Therefore, the new objective function has three terms: a normalizing term V_Y', a penalizing parameter ϕ which enforces a target ratio of V_Y/V_B, and radial term $\sqrt{V_Y^2 + V_B^2}$, which incentives larger strength. Using a mathematical language, the proposed objective function can be expressed as Eq. 3.1.

$$\begin{aligned} \underset{\mathbf{x}}{\text{minimize}}: \quad & f(\mathbf{x}) = \frac{V_Y'}{\phi\sqrt{V_Y^2 + V_B^2}} \\ \text{subject to}: \quad & \overline{Vol}(\mathbf{x}) = \Delta Vol \end{aligned} \tag{3.1}$$

Where:

$\mathbf{x}$	: Binary input vector representing the topology,
V_B	: Elastic shear buckling load,
V_Y	: Shear yield load,
$\overline{Vol}(\mathbf{x})$	: Volume of the input vector,
V_Y'	: Normalizing shear load,
ϕ	: Penalty function,
Δ	: Volume fraction,
Vol	: Volume of the full domain.

Regarding Eq. 3.1, the term V_Y' is employed to make the equation unitless and

corresponds to the yield strength of a plate subjected to a pure shear state of stress. Hence, considering the geometric variables illustrated in Figure 3.1, V'_Y is calculated using Eq. 3.2.

$$V'_Y = \frac{F_Y}{\sqrt{3}} \Delta w t \tag{3.2}$$

Where:

F_y : Yield strength of the material,

Δ : Volume fraction,

w : Full width of the domain,

t : Thickness of the plate.

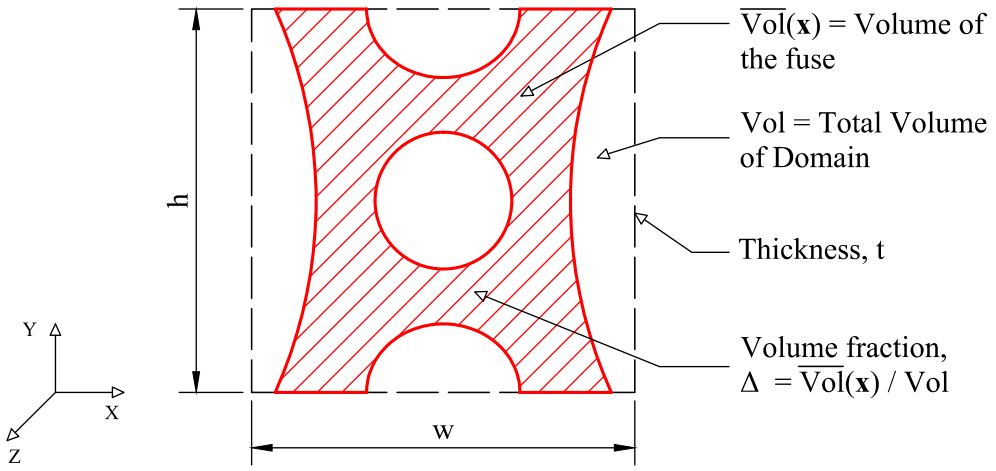

Figure 3.1: Geometric dimensions of a structural fuse

Eq. 3.3 describes the penalty function parameter ϕ that penalizes those topologies that do not lie along the user-defined $\overline{V_Y}/\overline{V_B}$ ratio.

$$\phi = a \exp\left(\frac{-(V_Y/V_B - \overline{V_Y}/\overline{V_B})^2}{2b^2}\right) \tag{3.3}$$

Where:

V_B : Elastic shear buckling load,

V_Y : Shear yield load,

a : Maximum value of penalty function,

b : Intensity of penalty function,

$\overline{V_Y}/\overline{V_B}$: Target value for V_Y/V_B.

The severity of the penalty function can be controlled by modifying the constants $a \in (0, 1.0]$ and $b \in (0, 0.5]$. While a assigns the maximum penalization value, b controls the intensity of the penalty function. Figure 3.2 shows the influence of b in the penalty function for the specific case when $a = 1.0$. Also, typical values of $\overline{V_Y}/\overline{V_B}$ will be less than one, although values of 0.1 to 0.3 are used later in this study.

Figure 3.3 shows a contour plot of the proposed objective function for $a = 1.0$, $b = 0.3$, and $\overline{V_Y}/\overline{V_B} = 1.0$. In this case, the best topologies are those that are away from the origin (maximize strength) but at the same time have a buckling load to shear yield load ratio equal to the target value.

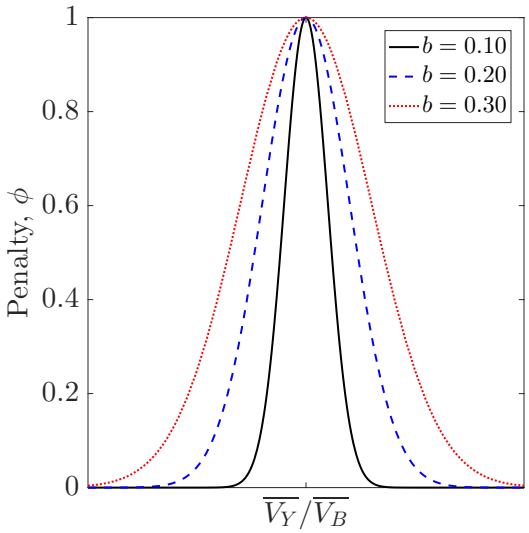

Figure 3.2: Influence of b in the penalty function ϕ

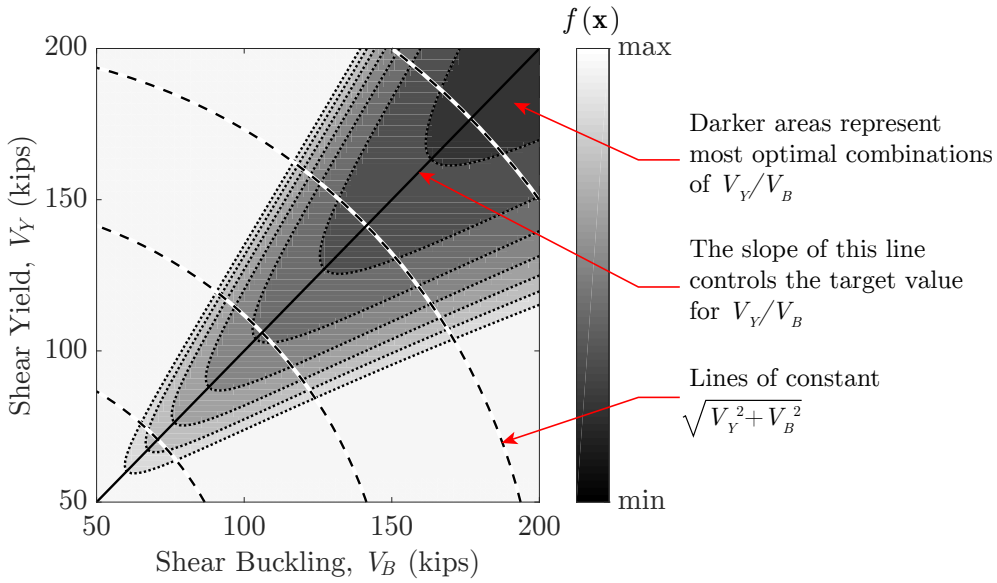

Figure 3.3: Objective function $f(\mathbf{x})$ contour plot for $a = 1.0$, $b = 0.3$ and $\overline{V_Y}/\overline{V_B} = 1.0$

What makes this objective function efficient is the simplicity of how its variables are computed. For instance, a computationally inexpensive procedure to estimate the elastic buckling load of a shear fuse is to perform an eigen-buckling analysis of the plate. Even though inelastic behavior and initial geometric imperfections are present in real fuses, the elastic buckling shear load obtained with this eigen-value procedure gives a useful quantification of how susceptible the geometry is to out-of-plane instabilities. For the calculation of the shear yield load, it is possible to use a 2D analysis of the geometry since all the out-of-plane displacements are neglected. This approach considers a nonlinear material constitutive relationship, but no geometric nonlinearity, turning the problem into a computationally inexpensive analysis as compared to a full 3D analysis. In summary, the objective function involves the implementation of two procedures: a 2D analysis which is geometrically linear but material nonlinear and a 3D linear buckling analysis.

It is worth mentioning that V_Y and V_B may not be the real shear yielding and shear buckling load, respectively. This observation stems from the fact that V_Y may not be an accurate yield load in presence of buckling. Along the same lines, V_B may not be an accurate

buckling load in presence of yielding. Hence, the ratio V_Y/V_B should be interpreted as the propensity of a structural fuse to yield before buckling.

3.2 Fundamentals of linear buckling analysis

In a linear finite element analysis, the corresponding equilibrium equation can be written as Eq. 3.4, where $[K_T]$ is the tangent stiffness matrix, $\{F\}$ is a reference external force vector, and $\{U\}$ is the displacement vector. Given a displacement vector, the internal stresses can be calculated and the geometric stiffness matrix $[K_G]$ can be assembled. Since the geometric stiffness matrix is proportional to the applied reference load vector, a scaled geometric stiffness matrix and a scaled load vector may be defined as Eq. 3.5 and Eq. 3.6, respectively.

$$[K_T]\{U\} = \{F\} \tag{3.4}$$

$$\{F\} = \lambda\{F\}_{ref} \tag{3.5}$$

$$[K_G] = \lambda[K_G]_{ref} \tag{3.6}$$

On the other hand, the material stiffness matrix $[K_M]$ does not change with the applied force because the material is assumed to behave linearly elastic. If we define the critical buckling load as $\{F\}_{crit} = \lambda_{crit}\{F\}_{ref}$, a relation between the stiffness matrices, the displacement vector and the critical buckling load can be written as in Eq. 3.7.

$$([K_M] + \lambda_{crit}[K_G]_{ref})\{U\} = \lambda_{crit}\{F\}_{ref} \tag{3.7}$$

This equation can be used to predict when the structure will elastically buckle based on the following statement: Since buckling is a state when a negligible increment in the applied load leads to drastically increasing displacements, Eq. 3.8 is valid, where $\{\delta U\}$ is

a displacement increment associated with the buckling phenomenon. This point where an increment in the displacement vector is possible without a significant change in applied force, as illustrated in Figure 3.4, is called the bifurcation point.

$$([K_M] + \lambda_{crit}[K_G]_{ref})(\{U\} + \{\delta U\}) = \lambda_{crit}\{F\}_{ref} \tag{3.8}$$

Plugging Eq. 3.7 into Eq. 3.8 gives an eigen-value problem presented in Eq. 3.9, where the smallest eigen-value represents the buckling multiplier λ_{crit}. In consequence, the critical buckling load defines the smallest applied load vector where there is a bifurcation point, Eq. 3.10.

$$([K_M] + \lambda_{crit}[K_G]_{ref})\{\delta U\} = \{0\} \tag{3.9}$$

$$\{F\}_{crit} = \lambda_{crit}\{F\}_{ref} \tag{3.10}$$

Since the trivial solution $\{\delta U\} = \{0\}$ is not of interest, the solution of Eq. 3.9 can be written as Eq. 3.11.

$$det([K_M] + \lambda_{crit}[K_G]_{ref}) = 0 \tag{3.11}$$

The eigen-value λ_{crit} is associated with its corresponding eigen-vector $\{\delta U\}$, which in this problem corresponds to the buckling shape of the system. Although the magnitude of this eigen-vector is completely arbitrary, this buckling mode represents the deformed configuration of the structure after buckling has occurred.

Nevertheless, we should mention that this theoretical solution is based on a geometry without initial imperfections in addition to a linearly elastic material behavior, therefore the actual buckling load will be lower than the value provided by this idealized solution. In other words, using a linear buckling analysis will generally overestimate the actual buckling capacity of the structure.

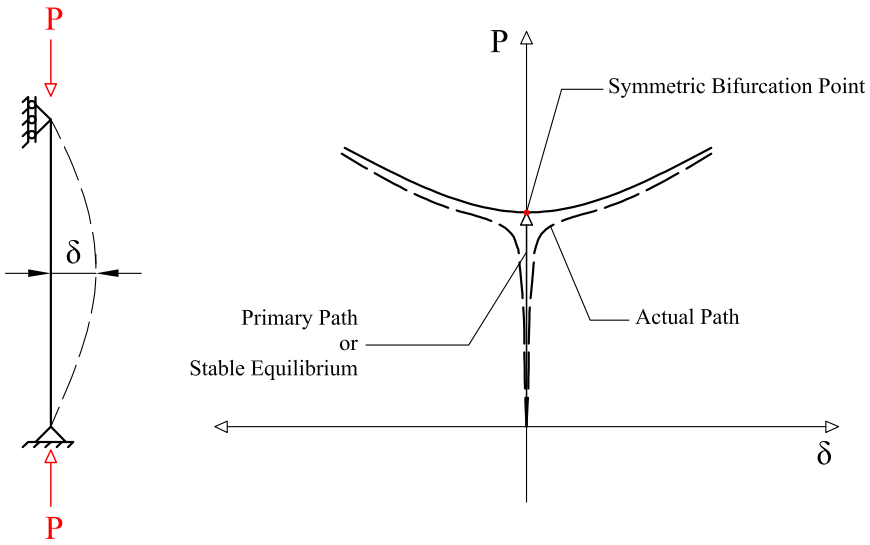

Figure 3.4: Illustration of a bifurcation point

3.3 Shear yield of a steel plate

A well-designed steel shear fuse transforms global shear deformations into local yielding mechanisms. In other words, at some value of lateral displacement the fuse should start to develop an inelastic response and therefore dissipate energy. Therefore, ensuring the stable development of such inelastic mechanisms within the domain of the fuse is directly related to an increment in the energy dissipation capacity of the device.

Nevertheless, the success of developing stable in-plane yielding mechanisms relies in a proper distribution of the material inside the domain of the fuse in addition to a reasonable out-of-plane stiffness. The intention of the two previous statements is to avoid the development of a not ideal energy dissipation mechanism such as tension field, since this behavior implies a reduction in the total amount of dissipated energy per unit volume that the fuse can handle.

Chapter 4

Implementation of the Objective Function

The implementation of the objective function is done using MATLAB. A single script controls all the pre-processing and post-processing procedures involved in the calculation of the objective function. Those different analyses are numbered as follows:

1. Receive the binary input vector. More specifically, MATLAB reads the input vector from a text file and transforms the one dimensional array into a grid representation of the structural topology.

2. Evaluate and fix connectivity. A second script analyzes whether the input vector has a connectivity issue associated with it. If so, a repairing algorithm is executed to ensure the admissibility of the input vector.

3. Calculate the shear buckling load. MATLAB writes the input file and initiates the linear eigen-buckling analysis using finite element software.

4. Calculate the shear yield load. MATLAB writes the input file and initiates the non-linear static analysis using finite element software.

5. Evaluate the objective function. Based on the output data provided by the two finite element analyses, MATLAB calculates the corresponding shear buckling load and shear yield load and then evaluates the objective function.

4.1 Input vector

With the intention of using the finite element method to evaluate the variables involved in the calculation of the objective function, the two-dimensional domain of a shear fuse is discretized into small square elements. Then, each individual square element represents either material or a void region. Based on the previous premise, the combination of the individual elements' states defines the distribution of material and void within the domain and therefore establish the topology of the fuse. Hence, using a binary approach philosophy, where the presence of material is associated with the number one (1) and the existence of a null region with the number zero (0); a discretized topology can be fully described by a binary vector.

The inverse process of converting a binary vector into a topology is also straightforward. Since each binary vector has the same number of elements as the total number of squares used to discretize the domain, by associating the position of each element of the input vector with a previously numbered domain, the binary vector is mapped to a grid representation of the topology, where elements with the corresponding value of one (1) become material while elements with a corresponding value of zero (0) become a void. Figure 4.1 illustrates how a binary vector is mapped to a two-dimensional topology.

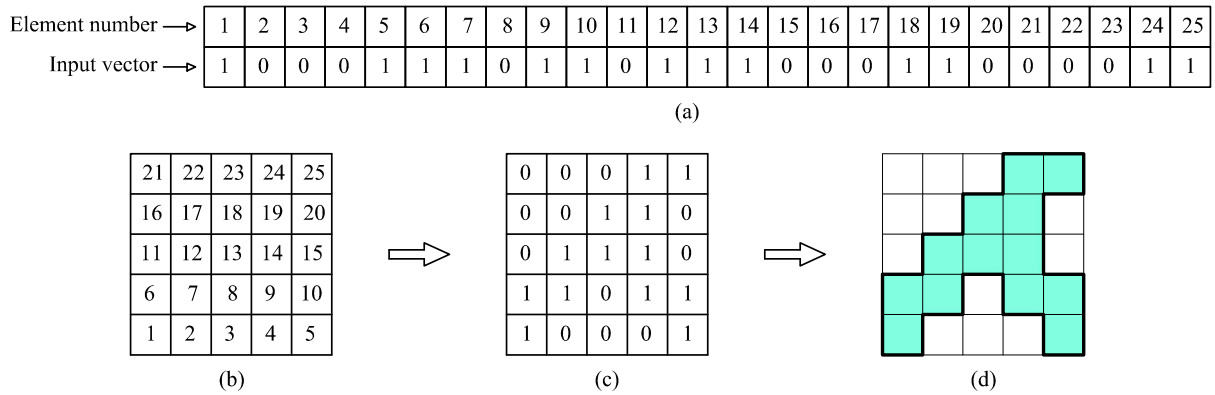

Figure 4.1: (a) Input vector, (b) Element numbering, (c) Grid representation, and (c) Structural topology

4.2 Connectivity analysis

Since the use of a topology optimization algorithm involves an initial step of defining the original full domain and its further discretization into a mesh of n square finite elements, the connectivity analysis plays an important role in the calculation of the objective function. This premise becomes more evident when it is pointed out that, if there is not any previous filtering procedure to eliminate many useless topologies; the objective function could be wasting computational time evaluating input vectors related to topologies with two or more unconnected regions of material within the domain, a condition which is physically unacceptable. In fact, unconnected members are meaningless for structures because there is no method of transferring loads between those members. Therefore, a successful topology optimization algorithm must ensure that each part of a design domain is in some way connected to the whole.

Before discussing procedures for filtering or repairing those vectors which represent useless topologies, it is important to keep in mind some considerations about what is meant by a admissible binary input vector:

1. All elements must be part of one connected topology. The requirement for two elements to be considered connected is to share a common edge. Elements sharing only one corner are not considered connected.

2. The input vector must always ensure the presence of material in at least one element associated with fixed degrees of freedom as well as at least one element related to points of load application. This basic requirement ensures the ability to establish a load path.

As a graphic reference, Figure 4.2 illustrates three of the previously mentioned connectivity issues. More specifically, Figure 4.2 (a) demonstrates how unconnected elements trigger inadmissibility even in the presence of a well-established load path. On the other hand, Figure 4.2 (b) illustrates how two sub domains are interconnected by sharing a single corner, in other words, two sub domains sharing an infinitesimally small connection surface leading to an infinite deflection under applied loads. Finally, Figure 4.2 (c) clarifies how a binary input vector can represent the total absence of a load path.

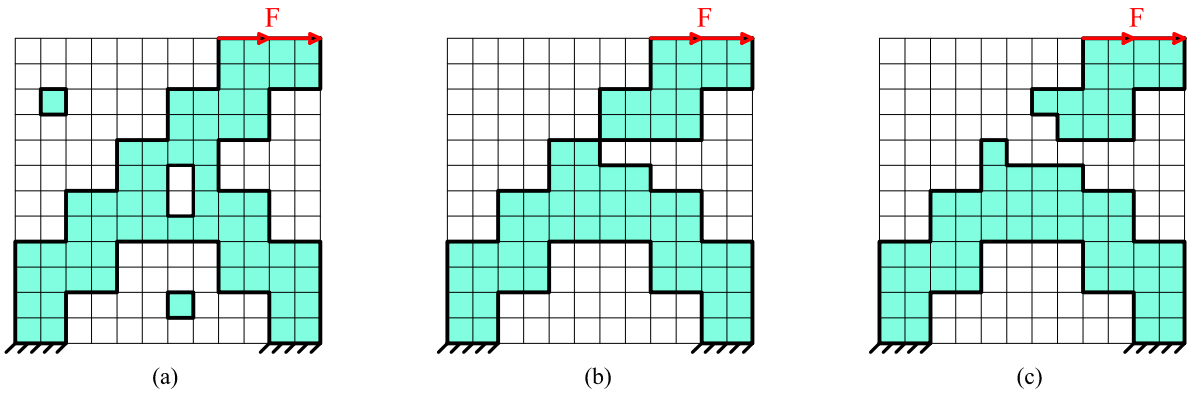

Figure 4.2: Example of three non physically admissible input vectors

The admissibility of a topology therefore depends in part on meeting the condition of mutually connected elements. Madeira et al. (2006) proposed a methodology to repair an unconnected topology, where the main procedure is explained by Algorithm 1 as follows:

Variables are defined as:

$\{Top\}$: Input topology,

$\{Top^*\}$: Repaired topology,

n : Total number of elements,

α : Fraction of the total active material that triggers the repair procedure,

$iter$: Maximum number of iterations,

$Distance$: Distance between two sub domains,

$d(x, y)$: Euclidean distance between two points,

V : Degree of attractiveness of a void element,

NV : Number of neighboring elements with active material,

NSD : Total number of active elements in each neighboring sub domain.

Algorithm 1 Repair of topologies

1: **procedure** REPAIR($\{Top\}, \alpha, iter$)

2: Identify all the sub domains SD_i.

3: $SD^* \leftarrow \mathbf{max}(SD_i)$.

4: **if** $\mathbf{sum}(SD^*) \geq \alpha \mathbf{sum}(Top)$ **then**

5: $cont \leftarrow 1$

6: **while** $(i > 1) \wedge (cont \leq iter)$ **do**

7: Use Eq. 4.1 to calculate:.

$$Distance_i(SD^*, SD_i) = \min\{d(x, y) : x \in SD^*, y \in SD_i\} \tag{4.1}$$

8: For each void element j, determine attractiveness V_j, according to Eq. 4.2.

$$V_j = NV_j + NSD_j \tag{4.2}$$

9: Displace the elements of the most distant component towards the empty elements with the greatest degree of attractiveness.

10: If the number of available empty elements is greater than the number of moving elements or vice versa, the selected elements are randomly chosen to have an even exchange.

11: $cont \leftarrow cont + 1$

12: **return** $\{Top^*\}$

Let us use the topology illustrated in Figure 4.3 (a) as an example to further explain the previous algorithm.

1. Identify all the sub domains, i.e. groups of active elements sharing the same edges. As we can see from Figure 4.3 (b), the different sub domains are:

   $SD_1 = [1]$

   $SD_2 = [4, 9, 10, 11, 15, 17]$

$SD_3 = [6]$

$SD_4 = [19, 25]$

$SD_5 = [24]$

$SD_6 = [27]$

$SD_7 = [29, 35]$

2. Then, $SD^* \leftarrow SD_2$ is the dominant sub domain with 6 out of 14 active elements.

3. The distance between the dominant sub domain and each of the remaining sub domain is summarized in Table 4.1.

Table 4.1: Distance between the dominant sub domain and the remaining ones

Subdomains	*Distance*
SD^*, SD_1	$\sqrt{5}$
SD^*, SD_3	$\sqrt{2}$
SD^*, SD_4	$\sqrt{5}$
SD^*, SD_5	$\sqrt{2}$
SD^*, SD_6	2
SD^*, SD_7	2

4. For each void element j, their corresponding degree of attractiveness is depicted in Figure 4.3 (c) at the upper right corner of each element.

5. The elements of the most distant sub domain are displaced to an empty zone with the highest V_j value as illustrated in Figure 4.3 (d). Since the number of active elements to be displaced is greater than the number of void elements with greatest V_j, a random choice is made to have an even exchange of material (see Figure 4.3 (e)).

6. The process is repeated until a topology with a single sub domain is obtained (see Figure 4.3 (f)).

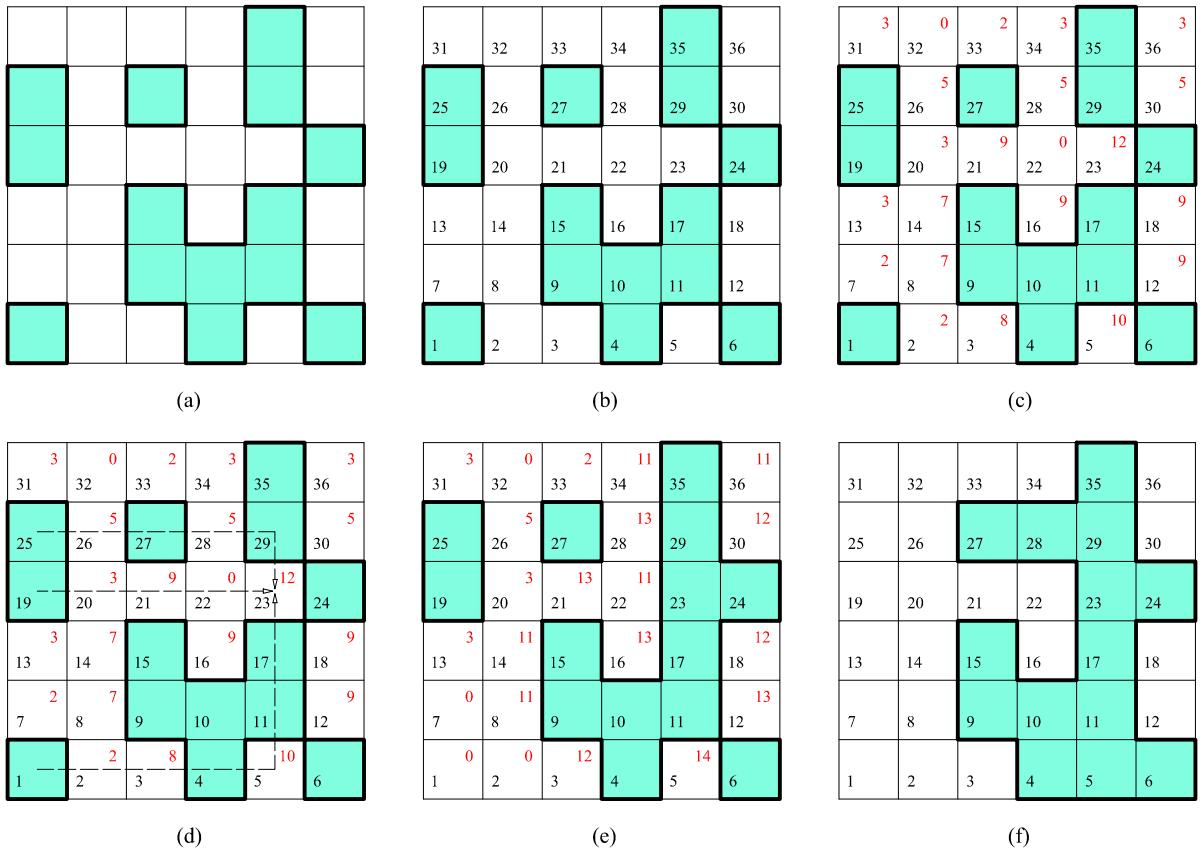

Figure 4.3: Repair process of a topology

Although the above described repair algorithm presents a solution for topologies with isolated elements and checkerboard patterns, there are also scenarios where a topology with a single connected component lacks a load path or where the number of iterations were not enough to totally repair the topology. While the last issue could be potentially solved by increasing the number of iterations, the absence of a structurally connected topology is handled by a image-processing-based analysis. This analysis consists of including additional seed elements along the boundaries with prescribed displacements and forces, then labeling the connected components with a unique integer number and finally checking whether the topology presents a load path by comparing the additionally seed elements' labels number. Figure 4.4 shows the different stages of the image-processing-based analysis, where a topology

without a load path has been found since the subdomains from each side are identified with a different number, as shown in Figure 4.4 (d).

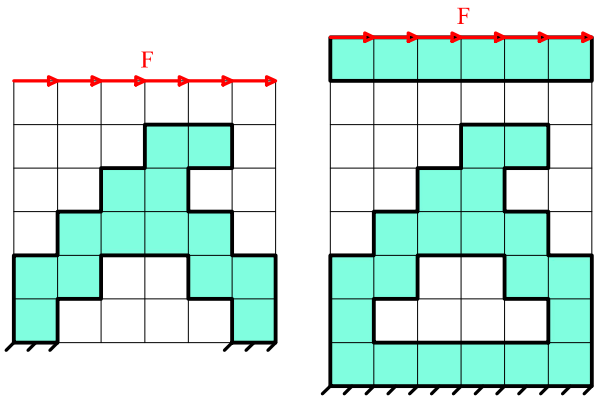

1	1	1	1	1	1
0	0	0	0	0	0
0	0	0	1	1	0
0	0	1	1	0	0
0	1	1	1	1	0
1	1	0	0	1	1
1	0	0	0	0	1
1	1	1	1	1	1

(c)

1	1	1	1	1	1
0	0	0	0	0	0
0	0	0	2	2	0
0	0	2	2	0	0
0	2	2	2	2	0
2	2	0	0	2	2
2	0	0	0	0	2
2	2	2	2	2	2

(d)

Figure 4.4: Image-processing-based analysis: (a) Original topology, (b) Additional seed elements, (c) Binary representation and (d) Connected component labeling

4.3 Eigen buckling analysis using FEAP

Since performing topology optimization using genetic algorithms requires a considerable amount of computational time, it is important to implement each of the individual finite element models using computationally efficient software. Therefore, a finite element software called FEAP (Finite Element Analysis Program) (Taylor, 2013) was used to model the geometries, boundary conditions and applied loads involved in the calculation of the shear buckling load of a steel fuse.

This decision was taken after analyzing the capabilities and downsides of two different programs: FEAP and OpenSees (McKenna et al., 2000). Both software use a similar coding syntax, but the main difference arises at the time of computing the linear buckling load. FEAP has a direct command to explicitly compute the geometric stiffness matrix, also it has the capability of solving the generalized linear eigen-value problem using the susbspace

iteration method. In contrast, OpenSees only allows the extraction of the tangent stiffness matrix and it does not have a built in function to solve the eigen-value problem. Please refer to Appendix A for a more detailed description of the drawbacks associated with OpenSees.

As a general example to corroborate the capability of FEAP to compute the shear buckling load of the fuse, Figure 4.5 illustrates the shape of a steel shear damper that will be analyzed as the case of study. Assuming that the corresponding input vector meets the admissibility criteria, three different steps will take place at the moment of computing the shear buckling load: defining the geometry of the plate and its material properties, applying the boundary conditions and reference load and finally solving the eigen-value problem.

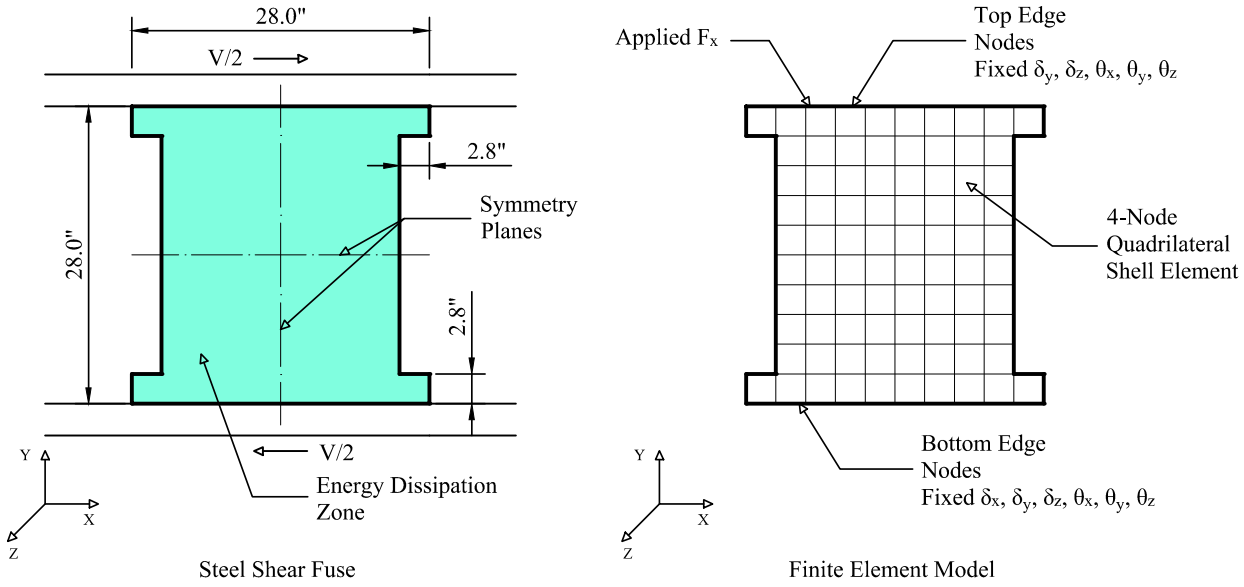

Figure 4.5: Steel shear fuse geometry and its FE representation for shear buckling analysis

A further explanation of the previously mentioned steps is presented in the following paragraphs.

1. Defining the geometry of the fuse involves a preprocessing of the binary input vector using MATLAB, in order to generate the nodal coordinates and element connectivity arrays that are required by FEAP to fully represent the domain of the fuse. Then,

since the buckling problem implies allowing the structure to deform in a perpendicular direction to the main plane of the model, a 4-node general purpose quadrilateral shell element with full integration was used in all the elements of the mesh associated with the actual presence of material. For this specific example, the thickness of the shear plate is equal to $t = 0.50\ in$, the shear factor $\kappa = 5/6$, the number of quadrature points through the thickness $q = 5$, elastic linear isotropic material, Youngs modulus of $E = 29000\ ksi$, and a Poissons ratio of $\nu = 0.3$.

2. Besides the obvious boundary condition of restraining all the degrees of freedom at the bottom edge of the fuse, it should be noted that the buckling analysis is conducted with the reference shear load applied parallel to the global X axis while its magnitude is evenly distributed among all the nodes corresponding to the top edge of the fuse. This distribution of the load keeps the horizontal displacement along the top edge relatively constant. Without enforcing this condition, the displacements along the edge are non-uniform and the buckling modes are dominated by localized deformations. Finally, the remaining five degrees of freedom of the top edge of the fuse are also restrained.

3. After the geometry and the boundary conditions are implemented, FEAP uses the applied reference load to compute the state of stress of the fuse. Then, using the command `GEOMetric`, FEAP uses the information of the current state of stress to develop the geometric stiffness of the system. The following operation is the implementation of the `SUBSpace` command during the solution algorithm in order to solve the generalized eigen-problem. Finally, the buckling load is calculated as the absolute value of the lowest eigen-value multiplied by the magnitude of the applied reference load. It is worth mentioning that the residual corresponding to the chosen eigen-value should be less than 10^{-10} to guarantee the convergence of the solution.

For the example problem, the first eigen values corresponding to the first buckling loads are checked to determine if they are accurate. To do so, a finite element model of the shear fuse with the same boundary conditions is modeled using Abaqus (Simulia, 2014).

Moreover, since both models should have the same characteristics, a 4-node doubly curved general-purpose shell element with full integration is used to model the domain. As conclusion, a comparison of the shear buckling loads obtained from Abaqus and FEAP are presented in Table 4.2. We can notice that the relative error between the values calculated using FEAP and those obtained from Abaqus is 0.48% as maximum. Finally, and as a further validation of the agreement between the results, the first four buckled shapes are presented in Figure 4.6.

Table 4.2: Comparison of the linear buckling loads

Mode	*FEAP* (kips)	*Abaqus* (kips)	*Discrepancy* (%)
1	582.52	585.34	0.48
2	−582.52	−585.34	0.48
3	749.52	752.12	0.35
4	−749.52	−752.12	0.35

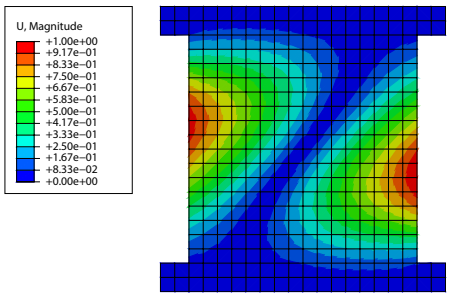

(a) Abaqus - Mode 1

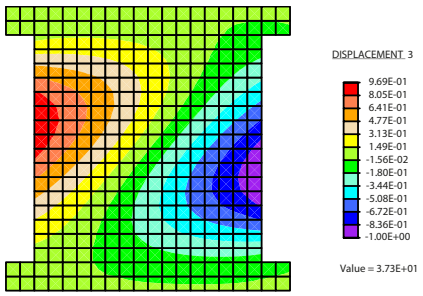

(b) FEAP - Mode 1

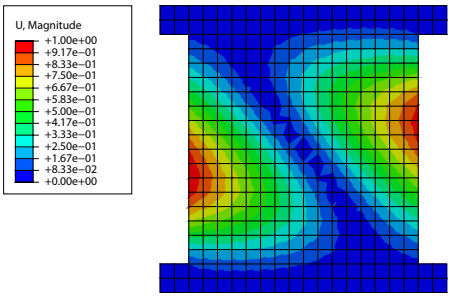

(c) Abaqus - Mode 2

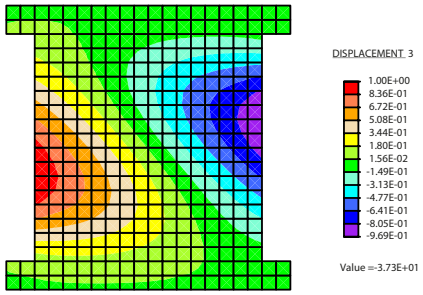

(d) FEAP - Mode 2

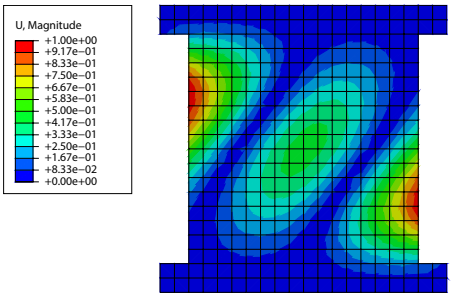

(e) Abaqus - Mode 3

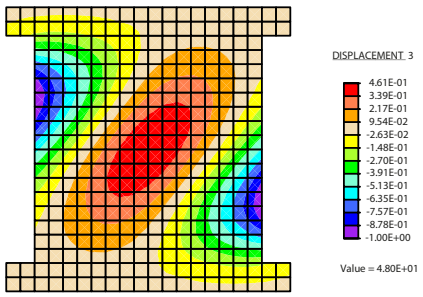

(f) FEAP - Mode 3

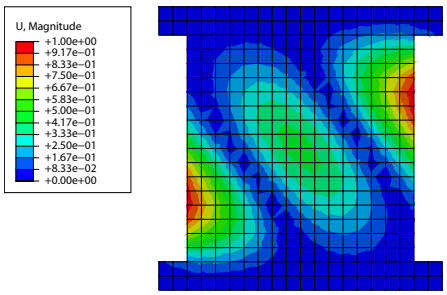

(g) Abaqus - Mode 4

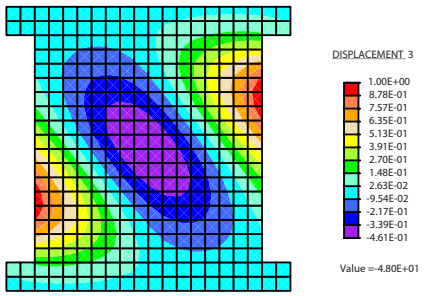

(h) FEAP - Mode 4

Figure 4.6: Abaqus buckling shapes and FEAP buckling shapes

4.4 Shear yield analysis using FEAP

As an example of calculating the shear yield load, Figure 4.7 illustrates the shape of a structural fuse in conjunction with its finite element representation. Since this problem is symmetric in terms of geometry and boundary conditions, only one quarter of the domain is analyzed in order to save computational time. Similar to the process of computing the buckling load, the procedure for computing the shear yield capacity of the fuse using finite element software involves three steps: define the geometry of the plate and the material properties, apply the boundary conditions and calculate the value of shear yield load based on the force vs displacement response of the system.

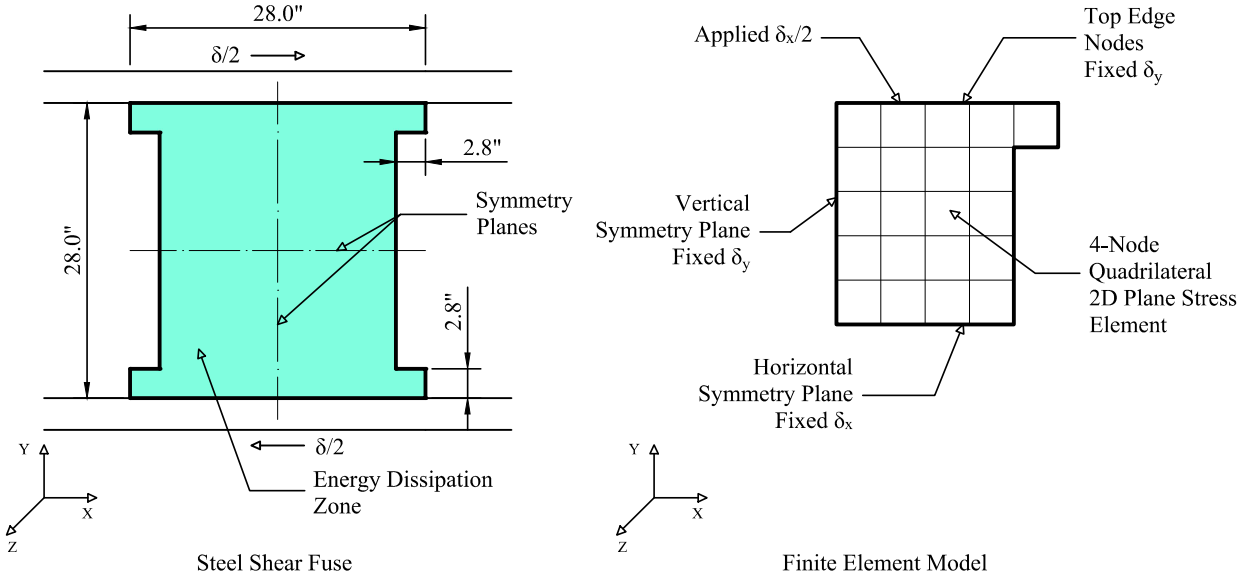

Figure 4.7: Steel shear fuse geometry and its FE representation for shear yield analysis

A more detailed explanation of the steps involved in the shear yield load calculation of a steel fuse using the finite element method is presented in the following paragraphs.

1. The process of converting the binary input vector to the element coordinates and connectivity arrays is exactly the same as the described for the shear buckling analysis. Since the out-of-plane deformations are restrained in this analysis and furthermore,

given the fact that most of the steel shear fuses have a small thickness ($t = 0.50\ in$ in our specific case) compared to its other geometric dimensions such as height and width; the problem can be modeled under a condition of plane stress. Therefore, a 4-node general purpose quadrilateral 2-D element with full integration was used in all the elements of the mesh associated with the actual presence of material. On the other hand, since the only source of non linearity present during the analysis comes from the material constitutive law, a bilinear elasto-plastic model was used. The elastic behavior is represented with a elastic isotropic model with a Youngs modulus equal to $E = 29000\ ksi$ and a Poissons ratio of $\nu = 0.3$. The plastic region is represented by a kinematic hardening model with a yield point of $F_Y = 50\ ksi$ and a hardening slope equal to 1% of the Youngs modulus, $H = 290\ ksi$. The values for F_y and hardening slope H, are chosen to be consistent with ASTM A572 Gr 50 steel plate material.

2. The boundary conditions for the shear yield analysis should consider the double symmetry of the problem. Hence, besides restraining the vertical displacement along the top boundary, the horizontal and vertical displacements are also restrained along the horizontal and vertical symmetry planes, respectively.

3. Regarding the loading protocol, a displacement controlled algorithm is used during the analysis and an applied displacement equal to 1% of the original fuses height is imposed to the quarter domain, which is equivalent to have a total drift of 2% in the original fuse. Finally, a tie constraint should be applied to all the nodes along the top edge in order to ensure a proper distribution of the stresses and at the same time to have an equal level of displacement along all the top edge of the domain.

4. During the analysis, the reaction forces in the X global direction as well as the applied displacement are recorded. The first two points of the load vs deformation response are used to compute the initial elastic stiffness of the system and then, the shear yield force corresponds to the point where the tangent stiffness is less than 25% of the elastic initial stiffness. If there is not such a case, the shear yield force is set equal to zero,

since this scenario corresponds to a not well defined yielding response.

For the example problem, the results are validated against the data provided by Abaqus. A finite element model of the full shear fuse geometry with the corresponding boundary conditions is modeled, using a 4-node 2D plane stress element with full integration to perform the analysis. The final information about the comparative analysis regarding shear yield loads and yielding drifts is presented in Table 4.3. It is stated that the relative error regarding the shear yield load is 0.20% while the relative error in the yielding drift value is 0.01%. Hence, there is an acceptable agreement between the results reported by both analyses. On the other hand, this difference between both approaches becomes more evident as the drift increases, having a relative error of 1.17% in terms of applied force at the end of loading protocol (Figure 4.8). Finally, the displacement fields U1 and U2 obtained from both analyses are presented in Figure 4.9 with the intention of reinforcing the idea that there is sufficient agreement between the two models.

Table 4.3: Comparison of the shear yield analysis

Parameter	*Shear yielding force* (kips)	*Yielding drift* (%)
FEAP	228.31	0.34
Abaqus	228.77	0.34
Discrepancy (%)	0.20	0.01

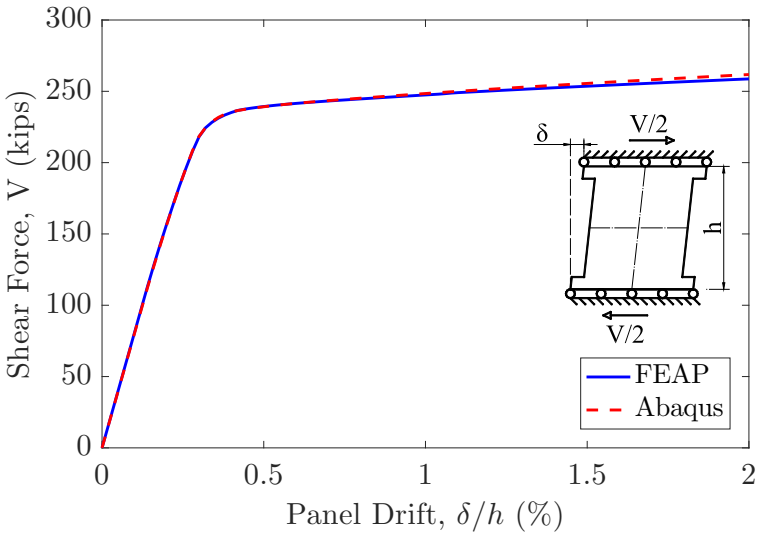

Figure 4.8: Shear Force vs Panel Drift curve

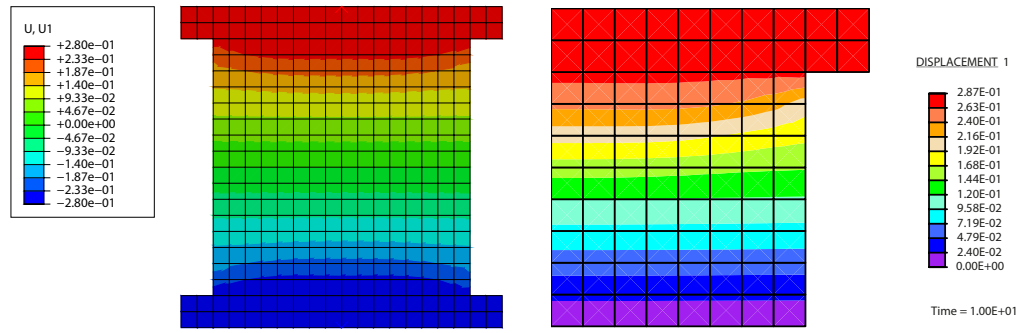

(a) Abaqus - Horizontal displacement

(b) FEAP - Horizontal displacement

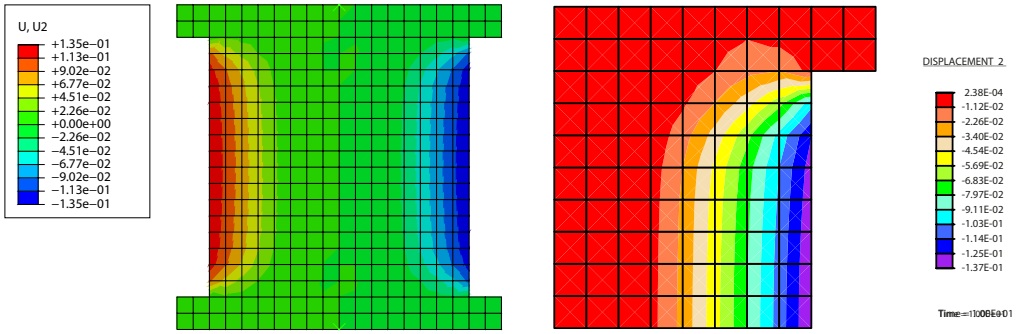

(c) Abaqus - Vertical displacement

(d) FEAP - Vertical displacement

Figure 4.9: Abaqus and FEAP displacements components at the end of the analysis

Chapter 5

Genetic Algorithm Concepts for Topology Optimization

In the context of structural topology optimization, genetic algorithms are probabilistic search procedures inspired by the process of natural evolution or survival-of-the fittest principle (Pezeshk and Camp, 2002). The initial population generally consists of a set of randomly generated topologies which are then selected for breeding based on a merit function. At each generation, the best candidates crossover their genetic information, i.e. they exchange their structural components, to create a new set of topologies. Sporadic mutation events are also introduced to help the algorithm maintain the diversity of the population. Hence, it is very likely that after a considerable number of generations the algorithm will produce an optimized shape.

The key advantages of using genetic algorithms for topology optimization can be listed as follows: the algorithm performs a global search without the need of the gradient information, the ability to use discrete variables in the search process, and its ease of implementation in parallel computing (Jakiela et al., 2000). However, there is also an increment in the number of finite element evaluations and therefore increased computational time required to obtain an optimized solution as compared to gradient-based optimization

(Sigmund, 2011).

5.1 Selection operation

The intent of the selection operator is to improve the quality of the population by assigning a higher probability of reproduction to those individuals with a better objective function. In other words, the higher quality topologies are more likely to pass their structural components to the next generation. At the same time, it is implicit that during this procedure those bad individuals will be lost and with them their genetic information.

5.1.1 Tournament selection

Tournament selection is one of the most common selection procedures due to its implementation efficiency, as no sorting of the population is required. Basically, a tournament is held among t competitors selected at random from the population, with t being the tournament size. Then, the individual with the best objective function is inserted into the mating pool. This process is repeated until the mating pool is filled. The pseudo code of tournament selection is given by Algorithm 2.

Algorithm 2 Tournament selection

1: **procedure** TOURNAMENT($t, \{I_1, ..., I_N\}$)
2: **for** $i \leftarrow 1, N$ **do**
3: $I_i^* \leftarrow$ best individual out of t randomly selected individuals from $\{I_1, ..., I_N\}$
4: **return** $\{I_1^*, ..., I_N^*\}$

By increasing the tournament size t, a higher average of the population's objective function is expected and the population's diversity is considerably reduced (Blickle and Thiele, 1995).

5.1.2 Exponential ranking selection

During the last generations of a fitness proportional selection method, when the individuals have very close objective function values, they will have almost the same probability to be selected. This scenario leads to a drop in the selection intensity towards better individuals, forcing the genetic algorithm to make poor decisions in terms of potential parents. To overcome this issue, a non fitness proportional method called exponential ranking selection can be used. Briefly explained, the N original individuals are sorted according to their objective function values, assigning the rank 1 to the worst individual and the rank N to the best individual. Then, an exponentially weighted probability is assigned to each individual according to Eq. 5.1.

$$p_i = \frac{c-1}{c^N - 1} c^{N-i} \tag{5.1}$$

Algorithm 3 is used to perform the exponential ranking selection.

Algorithm 3 Exponential ranking selection

1: **procedure** EXPONENTIAL RANKING($c, \{I_1, ..., I_N\}$)
2: $\{\overline{I_1}, ..., \overline{I_N}\} \leftarrow$ **sort**$\{I_1, ..., I_N\}$
3: $P_0 \leftarrow 0$
4: **for** $i \leftarrow 1, N$ **do**
5: $P_i \leftarrow P_{i-1} + p_i$
6: **return** $\{P_1, ..., P_N\}$

Regarding the variable $0 < c < 1$, it is observed that the closer c is to 1, the lower the 'exponentiality' of the probability distribution, becoming linear when c tends to 1. Consequently, a higher selection pressure but a lower population's diversity is anticipated by using a c value smaller than 1 (Blickle and Thiele, 1995).

After sorting the individuals and assigning their selection probabilities, a sampling algorithm has to be performed. Based on its relatively small bias towards better individuals

and its reduced computational cost, the Stochastic Universal Sampling (Baker, 1987) is used to sample the potential parents. Its mechanism consists in using a cumulative probability distribution $\{P_1, ..., P_N\}$ to select M individuals by choosing them at evenly spaced intervals D. Algorithm 4 presents the pseudo code for the Stochastic Universal Sampling.

Algorithm 4 Stochastic Universal Sampling

1: **procedure** SUS($M, \{\overline{I_1}, ..., \overline{I_N}\}, \{P_1, ..., P_N\}$)
2: $D \leftarrow \frac{P_N}{M}$
3: $S \leftarrow$ **random** $\in [0, P_N]$
4: **for** $i \leftarrow 1, M$ **do**
5: $L_i \leftarrow S + (i-1)D$
6: **for** $i \leftarrow 1, M$ **do**
7: $j \leftarrow 1$
8: **while** $\overline{I_j} \leq L_i$ **do**
9: $j \leftarrow j + 1$
10: $I_i^* \leftarrow \overline{I_j}$
11: **return** $\{I_1^*, ..., I_M^*\}$

5.2 Crossover operation with equal volume constraint

In a topology oriented optimization, the crossover operator generates new individuals by the stochastic process of recombining the structural components of an existing population. Although several methods allow the genetic algorithm to perform its search, it is reported that Single Point crossover works better for structural oriented or pattern development problems (Chapman et al., 1994). However, if a volume constraint is prescribed, all the different topologies generated by the genetic algorithm must have the same volume of material. Thus, a Single Point crossover operation that preserves the volume of material along the evolutionary process has to be implemented.

The crossover algorithm proposed by Madeira et al. (2005) is slightly modified and implemented to produce the next generation of topologies. This modification, in terms of element numbering, allows the crossover algorithm to work with horizontal and vertical structural components (Figure 5.1).

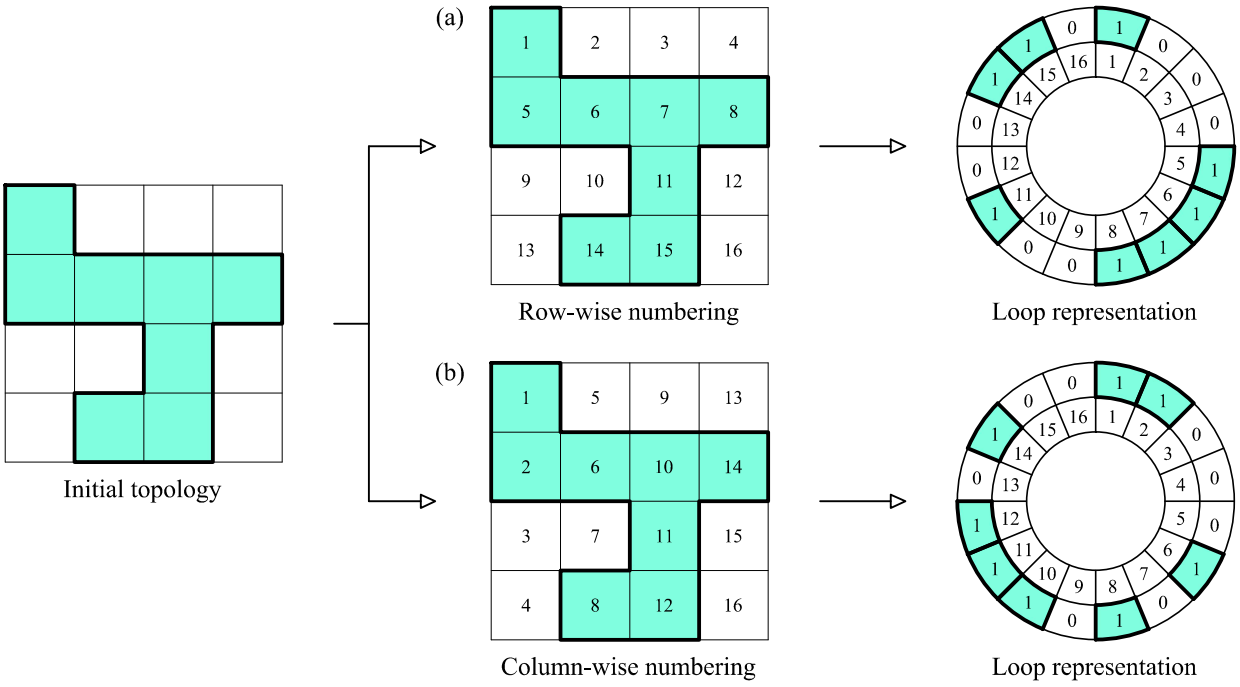

Figure 5.1: Topology reshape process for crossover operation

The pseudo code describing this crossover process is presented in Algorithm 5.

Variables are defined as:

n : Number of elements in the topology,

α : Number of elements to exchange during the crossover operation,

β_1 : Element number where the cut begins in the first topology,

β_2 : Element number where the cut begins in the second topology,

γ_1 : Number of active elements of the first topology within the interval $[\beta_1, \beta_1 + (\alpha - 1)]$,

γ_2 : Number of active elements of the second topology within the interval $[\beta_2, \beta_2 + (\alpha - 1)]$.

Algorithm 5 Single point crossover with equal volume constraint

1: **procedure** SPC($\alpha, \{Top_1, Top_2\}$)
2: $Top_1^* = Top_1$
3: $Top_2^* = Top_2$
4: Reshape the input topologies according to either Figure 5.1 (a) or Figure 5.1 (b).
5: Select the initial β_1, where $\beta_1 \in [1, n]$.
6: Select the initial β_2, where $\beta_2 \in [1, n]$.
7: $\gamma_1 \leftarrow \mathbf{sum}(Top_1(\beta_1 : \beta_1 + (\alpha - 1)))$.
8: $\gamma_2 \leftarrow \mathbf{sum}(Top_2(\beta_2 : \beta_2 + (\alpha - 1)))$.
9: **if** $(\gamma_1 \neq \gamma_2) \wedge (\beta_2 < n)$ **then**
10: $\beta_2 \leftarrow \beta_2 + 1$
11: **Go to** Step 7
12: **else if** $(\gamma_1 \neq \gamma_2) \wedge (\beta_2 = n)$ **then**
13: $\beta_1 \leftarrow \beta_1 + 1$
14: **Go to** Step 6
15: **else if** $\gamma_1 = \gamma_2$ **then**
16: $Top_1^*(\beta_1 : \beta_1 + (\alpha - 1)) \leftarrow Top_2(\beta_2 : \beta_2 + (\alpha - 1))$
17: $Top_2^*(\beta_2 : \beta_2 + (\alpha - 1)) \leftarrow Top_1(\beta_1 : \beta_1 + (\alpha - 1))$
18: **else**
19: **return** $\{Top_1^*, Top_2^*\}$

Selecting a value for β_1 and β_2 in Step 6 and Step 7 respectively, leads to three different crossover scenarios.

1. Use $\beta_1 = \beta_2 =$ fixed value throughout all the algorithm.
2. Use $\beta_1 = \beta_2 =$ random value. This value has to be determined whenever the operator is used.
3. β_1 and β_2 are independent random choices.

In the first case, two individuals will generate the same offspring no matter when they are selected for mating. In the second case, the probability of two individuals to generate the same offspring is smaller. Finally, the third case will generate an offspring with the highest diversity among the three possible scenarios and is by this reason the one used in this study.

Let us use Figure 5.2 to illustrate how Algorithm 5 works. First, the two topologies selected for mating are reshaped using a row-wise order. Then, considering a random scenario where $\alpha = 8$, $\beta_1 = 1$ and $\beta_2 = 5$, the number of active elements in the first progenitor is $\gamma_1 = 4$ and $\gamma_2 = 3$ for the second progenitor. Given that $(\gamma_1 \neq \gamma_2) \wedge (\beta_2 < N)$, we have to increment γ_2 by 1 and go to Step 7. After some iterations, when $\beta_2 = 7$ we have an equally exchange of volume since $\gamma_1 = 4$ and $\gamma_2 = 4$. Hence, we make the corresponding exchange of genetic material, tanking into account the element number where the cut begins in each topology, as suggested in Figure 5.2. As a final observation, we can notice from the generated topologies that the crossover operation does not necessarily guarantee the admissibility of the offspring.

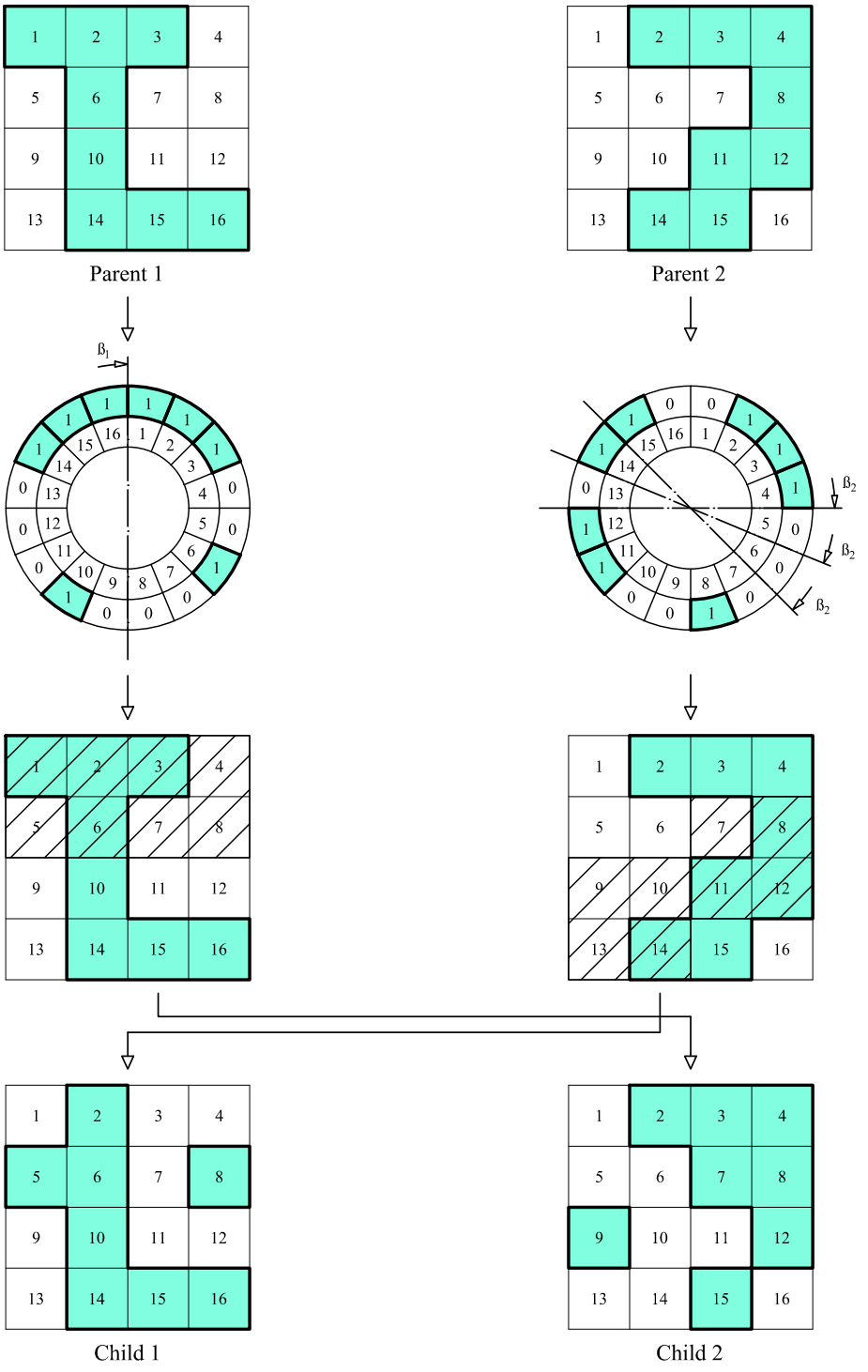

Figure 5.2: Example of the crossover operation with equal volume constraint

5.3 Mutation operation

When properly set, the mutation operator should help the genetic algorithm to avoid local minima by introducing diversity in the population. In other words, by preventing the topologies from becoming similar to each other, the evolutionary process is more likely to find a better solution at each generation. For a topology that satisfies the mutation probability, the mutation algorithm will randomly pick a number of active elements equivalent to the volume to be mutated. Then, those elements will be moved to random void locations. In this way, the volume of material remains constant after the mutation operation.

As a summary, Algorithm 6 presents the pseudo code for the mutation procedure.

Variables are defined as:

p : Probability of mutation $\in [0, 1]$

n : Number of elements in the topology,

α : Fraction of the total active material.

Algorithm 6 Mutation operation with equal volume constraint

1: **procedure** MUTATION($p, \alpha, \{Top\}$)
2: $\{Top^*\} = \{Top\}$
3: **if** $p < random[0, 1]$ **then**
4: **else**
5: $Subset_1 \leftarrow$ Random sample of $round(\alpha n)$ active elements
6: $Subset_2 \leftarrow$ Random sample of $round(\alpha n)$ void elements
7: $Top^*(Subset_1) \leftarrow 0 \wedge Top^*(Subset_2) \leftarrow 1$
8: **return** $\{Top^*\}$

Figure 5.3 (a) is used as a graphic example of the mutation operation, where $Subset_1 = \{2, 3, 4, 7, 10, 11, 13, 14\}$ and $Subset_2 = \{1, 5, 6, 8, 9, 12, 15, 16\}$ correspond to the group of

active and void elements, respectively. Then, a fraction of active elements equal to $\alpha = 0.25$, which is equivalent to 2 active elements, will be mutated. Since we are dealing with a volume constraint, the exchange of the genetic information between 2 randomly selected active elements and 2 randomly selected void elements is performed, as illustrated in Figure 5.3 (b). Finally, Figure 5.3 (c) shows the mutated topology. However, it is important to note that the mutation procedure does not necessarily guarantee the admissibility of the mutated topology.

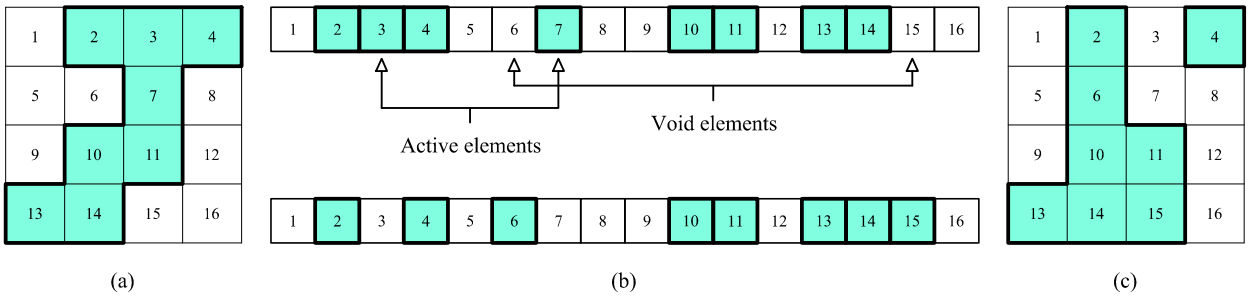

Figure 5.3: Example of the mutation operation with equal volume constraint

Chapter 6

Optimization Implementation and Sensitivity Analysis

Given the multiple possible combinations of genetic algorithm operators, a sensitivity analysis is performed prior the actual topology optimization routine. The intention is to analyze how the selection, repair and mutation procedures influence the performance of our algorithm. Moreover, considering the stochastic nature of the genetic algorithm, five different initial populations representing a square domain with constant thickness are generated. Each set of topologies is used to initialize the evolutionary process and 40 generations are performed. Then, a conclusion is derived primarily based on the rate of reduction in the averaged objective function values. Finally, the most effective combination of genetic operators will be incorporated in the full optimization routine.

6.1 Variation of the genetic operators

Sixteen genetic algorithms are created as a result of varying some genetic operators while keeping others constant. A description of each variation is presented in the next

paragraph.

- Selection operator: Varying the selection operator is intended to analyze which one produces the best convergence rate as well as the best objective function value. A Tournament selection operator considering $t = (2, 3)$ and an Exponential Ranking selection considering $c = (0.80, 0.95)$ are examined.

- Crossover operator: During the sensitivity analysis, the Crossover operator is kept constant. More specifically, a Single Point crossover operation which interchanges half of the parent's genetic information is always invoked during each generation.

- Mutation operator: Given a probability of mutation of $p = 0.05$ and a fraction of the total active material equal $\alpha = 0.10$, the variation of the operator consists in including or not the mutation procedure during the optimization routine.

- Repair algorithm: Madeira et al. (2006) reported that repairing unconnected topologies when the dominant connected component has at least 90% of total material volume is an effective mechanism for convergence acceleration. For this reason, the influence of the fraction of the total active material that triggers the repair procedure is investigated by considering $\alpha = (0.80, 0.90)$.

6.2 Domain description

The domain corresponds to a square plate with constant thickness described as follows:

- Geometry: A square plate of 28 by 28 inches and thickness equal to $t = 0.50$ inches represents the domain. These geometric dimensions are selected to approximately replicate the Specimen 1-13-1 tested by Egorova et al. (2014). Although the volume fraction

is treated as a variable in the next chapter, the sensitivity analysis only considers a volume fraction equal to $\overline{Vol}(\mathbf{x}) = 0.40Vol$.

- Material: To be consistent with ASTM A572 Gr 50 steel plate material, a Youngs modulus equal to $E = 29000\ ksi$ and a Poissons ratio of $\nu = 0.3$ are considered. The plastic region is represented by a kinematic hardening model with a yield point of $F_Y = 50\ ksi$ and a hardening slope equal to 1% of the Youngs modulus, $H = 290\ ksi$.

- Finite element mesh: A mesh of 32 by 32 square finite elements is used to discretize the domain for optimization. An extra row of square elements are always added to the top and bottom edge of the domain to ensure the correct allocation of the boundary conditions, however these seed elements are not part of the optimization procedure.

- Symmetry: Given the current boundary conditions and the cyclic displacements to which a steel structural fuse is subjected, it is reasonable to assume that an optimized shape would be symmetrical about the vertical and horizontal axes. Thus, double symmetry condition is enforced by genetically operating with input vectors that represent only one quarter of the actual topologies. Then, the shear buckling load and the shear yield load are calculated using the process described in Section 4.3 and Section 4.4 respectively.

6.3 Objective function variables

6.3.1 Penalty function, ϕ

By setting $a = 1$ and $b = 0.1$, Eq. 3.3 becomes Eq. 6.1. This penalty function is used for the current sensitivity analysis and in future algorithms as well.

$$\phi = \exp\left(-50(V_Y/V_B - \overline{V_Y}/\overline{V_B})^2\right) \tag{6.1}$$

6.3.2 Penalty function bias, $\overline{V_Y}/\overline{V_B}$

Based on the idealization of our models, having a ratio $\overline{V_Y}/\overline{V_B} < 1$ would indicate yielding of the structural fuse before presenting significant out-of-plane deformations. Nevertheless, the elastic buckling load overestimates the actual buckling strength of the fuse. Depending on the initial imperfections and the nonlinear behavior of the material, the inelastic buckling load could be less than the load predicted by the elastic analysis. This suggests that the smallest values of V_Y/V_B are desirable to limit buckling, even though the structural fuse may buckle after some inelastic cycles. However, using a value for $\overline{V_Y}/\overline{V_B}$ that is too small can lead to a topology with an insignificant in-plane stiffness. Hence, the ratio $\overline{V_Y}/\overline{V_B} = 0.2$ is used for the sensitivity analysis but the range $0.1 \leq \overline{V_Y}/\overline{V_B} \leq 0.3$ is considered in subsequent chapters.

6.3.3 Objective function

To get the final expression for the objective function, we use the material properties and the above described geometric dimensions to calculate the pure shear load described by Eq. 3.2, where $V_Y' = 280\sqrt{3}/3$ kips. Finally, Eq. 3.1 becomes:

$$f(\mathbf{x}) = \frac{280}{\sqrt{3}\exp\left[-50(V_Y/V_B - 0.2)^2\right]\sqrt{V_Y^2 + V_B^2}} \tag{6.2}$$

Where:

$\mathbf{x}$: Binary input vector representing the topology,

V_B : Elastic buckling load,

V_Y : Shear yield load.

6.4 Assumptions for the optimization algorithm

6.4.1 Non admissible topologies

If a topology lacks a load path or if it has disconnected structural components, the topology is cataloged as non admissible. Although these shapes are separated from the admissible ones, they are not discarded from the optimization routine. More specifically, after all the admissible topologies have been evaluated and their objective function were calculated, all the non admissible topologies are assigned an objective function value equal to 1.01 times the worst objective function value extracted from the admissible group.

6.4.2 Repeated topologies

It is possible that the repair, crossover or mutation operator will generate a topology that is already part of the current population or a topology that was analyzed during previous generations. To avoid unnecessary finite element analyses, we could either exclude the duplicated topology or search among previous results the information associated with the repeated shape. However, excluding duplicated topologies implies working with a varying number of individuals during each generation, affecting the Selection operation. Also, the time required to check whether a topology was already analyzed increases with the population size as well with the mesh refinement. In conclusion, since both solutions compromise other aspects of the optimization routine, the genetic algorithm used in this study does not have any special consideration for repeated topologies.

6.4.3 Elitism

This concept involves copying a small fraction of the best candidates, unchanged, into the next generation of individuals. By ensuring that the genetic algorithm does not waste

time rediscovering previously discarded topologies, a positive impact in the performance of the evolutionary process is likely to happen. In this study 4% of the total number of individuals are considered as elite.

6.4.4 Initial population

Taking into account the volume constraint, the initial population consists of 100 initial topologies. These 100 topologies are divided into 95 randomly generated shapes, 1 topology representing the ring-shaped structural fuse (Egorova et al., 2014), 3 variations of the butterfly fuse (Ma et al., 2010), and 1 topology associated with the compliance minimization of the structural fuse (Sigmund, 2001). These 5 specific topologies and their quarter of domain representation are illustrated in Figure 6.1.

Please refer to Appendix B.1 for the subset of initial topologies corresponding to different volume fractions.

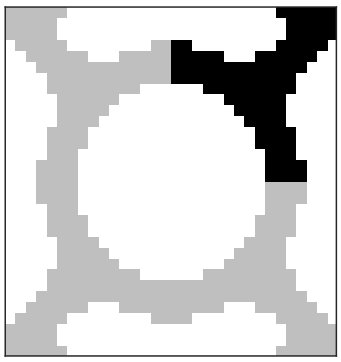

(a) Ring-shaped fuse (Egorova et al., 2014)

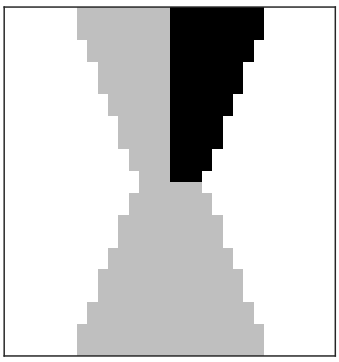

(b) Butterfly fuses (Ma et al., 2010)

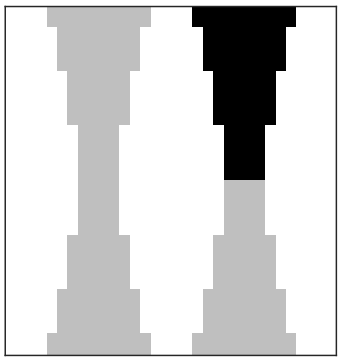

(c) Butterfly fuses (Ma et al., 2010)

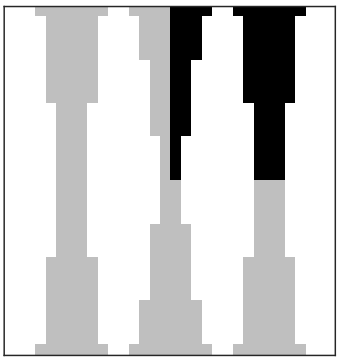

(d) Butterfly fuses (Ma et al., 2010)

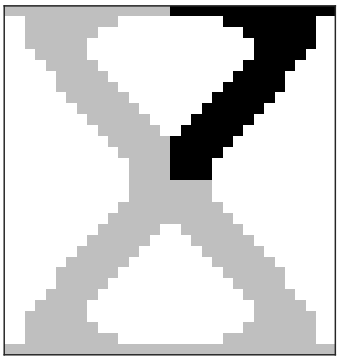

(e) Compliance minimization problem (Sigmund, 2001)

Figure 6.1: Subset of initial topologies for $\overline{Vol}(\mathbf{x}) = 0.40Vol$

6.5 Sensitivity analysis results

6.5.1 Averaged objective function value

Due to the stochastic nature of the genetic algorithms, the performance comparison between variations of a genetic operator is based on the averaged results of independent runs of the genetic algorithm (Wang et al., 2006). Hence, this sensitivity analysis considers the averaged results of the genetic algorithm with five independent initial populations. Figure 6.2 shows the evolution of the average objective function for the four selection scenarios.

We can observe that at the end of the 40th generation, the two best results for a Tournament selection operator are obtained with $t = 3$ and $\alpha = 0.90$, having an averaged objective function value equal to $\overline{f}(\mathbf{x}) = 0.86$. Also, the two worst results for an Exponential Ranking selection corresponding to $c = 0.95$ and $\alpha = 0.90$ have an averaged objective function value equal to $\overline{f}(\mathbf{x}) = 0.88$. Since six out of eight genetic algorithms with an Exponential Ranking selection outperform all the results obtained with a Tournament selection operator, we conclude that under the assumptions and conditions used in this sensitivity analysis, an Exponential Ranking selection produces better results than a Tournament selection operator.

After discarding the Tournament selection method, we will refer and compare the results of the two cases using an Exponential Ranking selection. We can observe that when $c = 0.80$, the algorithm converges to approximately the same averaged objective function value $\overline{f}(\mathbf{x}) = 0.81$ independently of the mutation or repair operator. In contrast, when $c = 0.90$ the results do depend on selected mutation and repair operators, however the best results $\overline{f}(\mathbf{x}) = 0.84$ are linked to a repair variable $\alpha = 0.80$.

6.5.2 Convergence rate

The best converge rate during the first 10 generations corresponds to the genetic algorithm using an Exponential Ranking selection method with $c = 0.80$. Once again this

convergence rate is independent of the mutation and repair operator. Also, this rapid improvement in the average value of the objective function during the first generations increases the probabilities of converging to a better solution at the end of the 40th generation.

6.5.3 Fraction of admissible topologies

Having a higher fraction of admissible topologies during the early stages of the evolutionary process could potentially lead to preserve or even increasing the diversity of the next generation of individuals. According to Figure 6.3, the best option to have a good percentage of admissible topologies within the early generations is the Exponential Ranking selection with $c = 0.80$. An average of 69% of the total number of topologies are admissible at the end of the 10th generation. Once again, using an specific mutation and repair operator does not influence in great magnitude this fraction of admissible topologies.

In contrast, at the end of the 10th generation, only 7% of the topologies are admissible when a Tournament selection operator with $t = 2$ is implemented.

6.5.4 Sensitivity analysis conclusion

Based on the conclusions obtained in previous sections, an Exponential Ranking selection method with $c = 0.80$ is selected for use in this study. At the same time is reasonable to say that invoking or not the mutation operation does not greatly influence the results of the evolutionary process. Along the same lines, our sensitivity analysis indicated there is not a big improvement when the variable α in the repair algorithm decreases from $\alpha = 0.90$ to $\alpha = 0.80$. Hence, the decision of choosing the appropriate mutation and repair operators is made based on additional facts and previous studies, as follows:

1. Since the mutation operation is cataloged as one way to preserve the population's diversity, the author considers appropriate to include it in optimization routines of

future chapters.

2. A previous study of topology optimization of structures using genetic algorithms conducted by Madeira et al. (2006) concluded that invoking the repair algorithm when a non-admissible topology has a dominant subdomain with at least 90% of the total material volume is an effective mechanism for converge acceleration. Hence, a repair variable of $\alpha = 0.90$ is used in future optimization algorithms.

To summarize, genetic algorithms in coming chapters will use an Exponential Ranking selection with $c = 0.80$, a Mutation procedure with $p = 0.05$ and $\alpha = 0.10$, and a Repair algorithm with $\alpha = 0.90$.

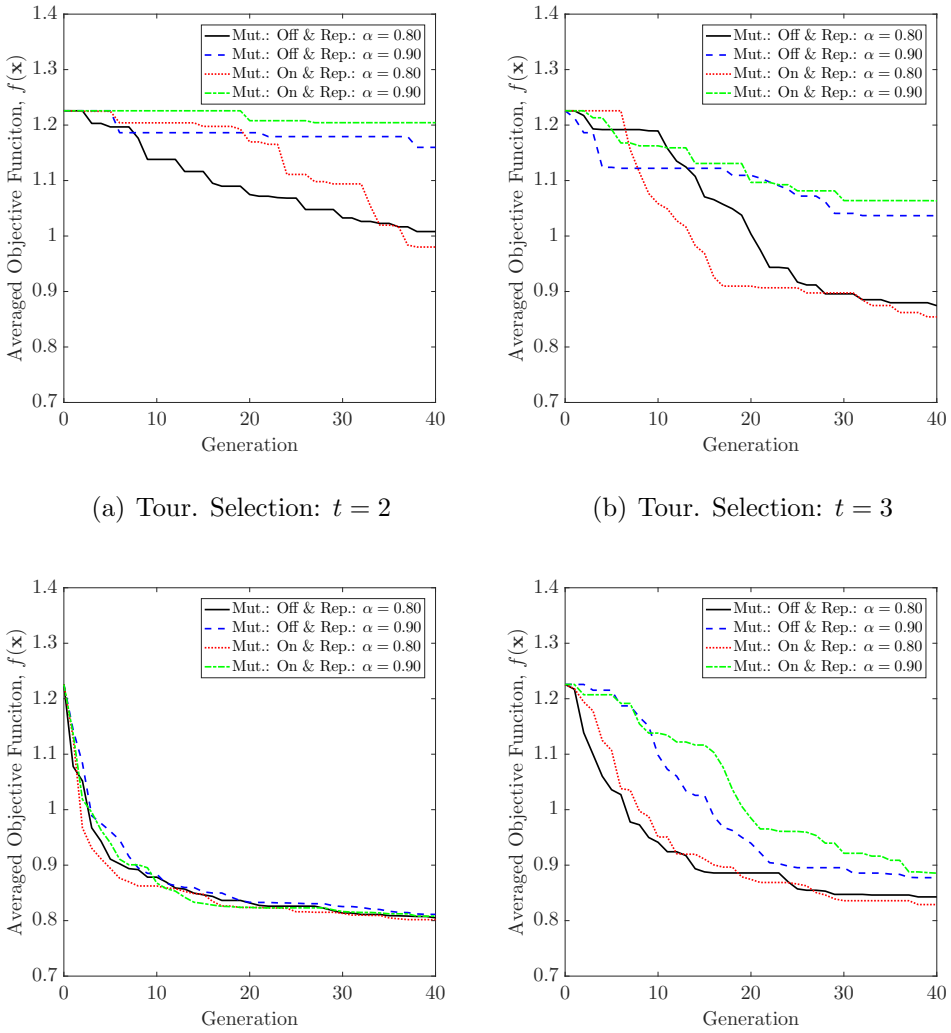

(a) Tour. Selection: $t = 2$

(b) Tour. Selection: $t = 3$

(c) Exp. Rank. Selection: $c = 0.80$

(d) Exp. Rank. Selection: $c = 0.95$

Figure 6.2: Sensitivity analysis results - Averaged objective function for $\overline{V_Y}/\overline{V_B} = 0.20$ and $\overline{Vol} = 0.40Vol$

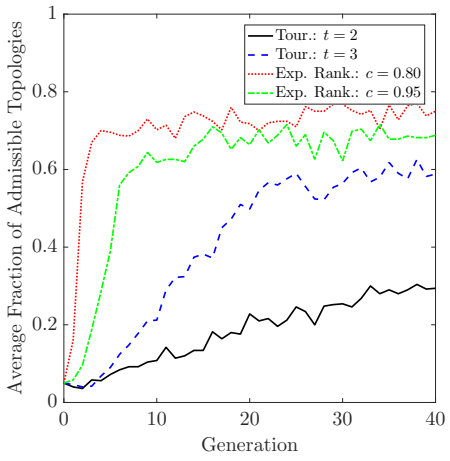

(a) Mutation: Off & Repair: $\alpha = 0.80$

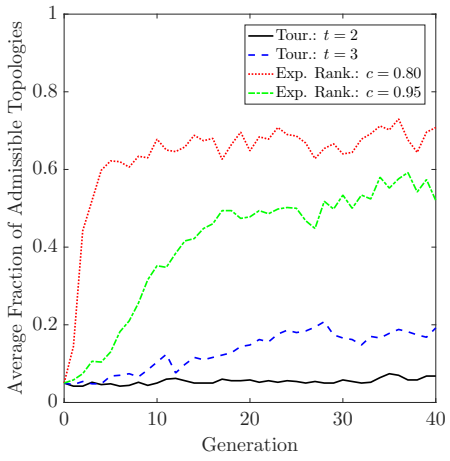

(b) Mutation: Off & Repair: $\alpha = 0.90$

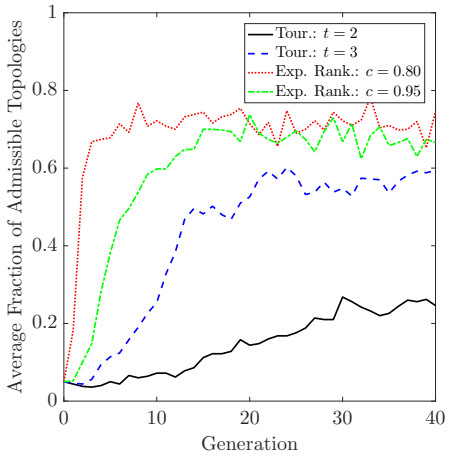

(c) Mutation: On & Repair: $\alpha = 0.80$

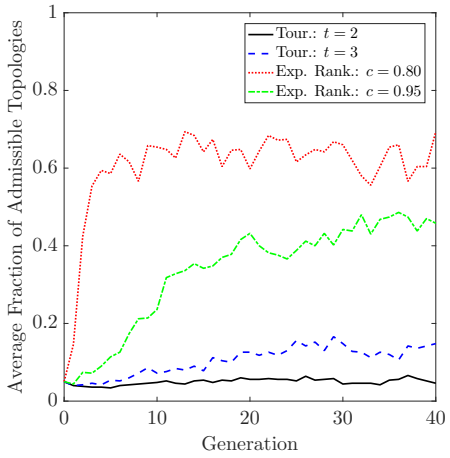

(d) Mutation: On & Repair: $\alpha = 0.90$

Figure 6.3: Sensitivity analysis results - Average fraction of admissible topologies for $\overline{V_Y}/\overline{V_B} = 0.20$ and $\overline{Vol}(\mathbf{x}) = 0.40Vol$

Chapter 7

Results of Topology Optimization

In this chapter, the conclusions derived from the sensitivity analysis are implemented into a genetic algorithm to optimize a structural fuse using 400 generations. Additionally, the domain description and general assumptions used during the sensitivity analysis remain unchanged.

To account for the stochastic nature of genetic algorithms, two unique sets of topologies are used as initial populations in two independent runs. After presenting the results for a baseline case, the influence of the bias $\overline{V_Y}/\overline{V_B}$ and volume fraction $\overline{Vol}(\mathbf{x}) = \Delta Vol$ are investigated. Then, the effect of scaling the width, height and thickness of the fuse is analyzed in a parametric study.

7.1 Baseline case

The baseline case is associated with the topology optimization of a square plate of 28 by 28 inches and constant thickness $t = 0.50\ in$ (Figure 7.1). The material properties are those from ASTM A572 Gr 50 steel where $E = 29000\ ksi$, $\nu = 0.3$, $F_Y = 50\ ksi$ and $H = 290\ ksi$. A finite element mesh of 32 by 32 square elements is used to discretize domain.

Once again, the calculation of the shear buckling load and shear yield load follows Section 4.3 and Section 4.4, respectively.

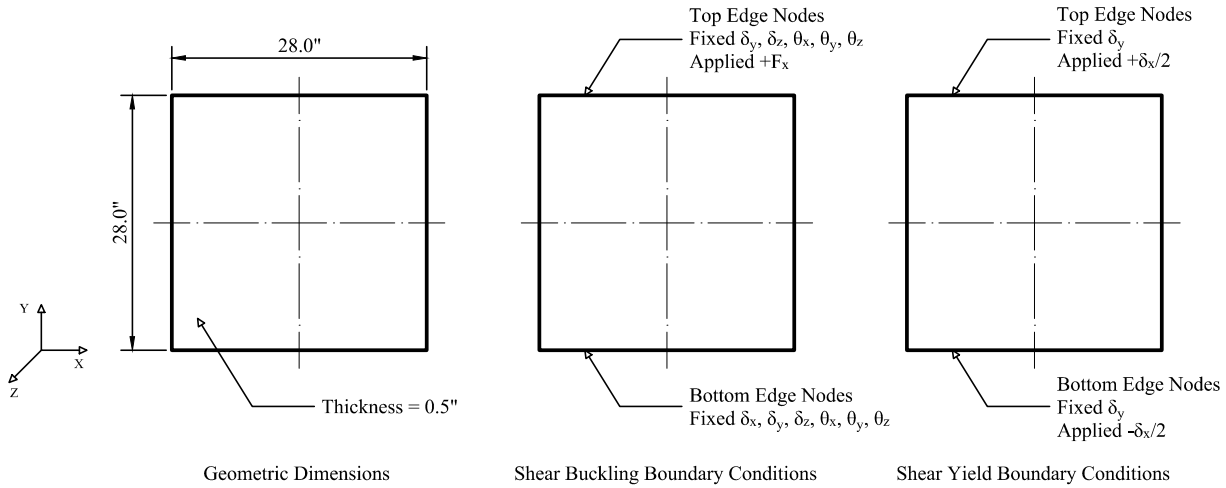

Figure 7.1: Illustration of the domain for the reference case

Additionally, a bias of $\overline{V_Y}/\overline{V_B} = 0.20$ and a volume fraction of $\overline{Vol}(\mathbf{x}) = 0.40Vol$ are considered. Hence, the objective function becomes Eq. 7.1.

$$f(\mathbf{x}) = \frac{280}{\sqrt{3}\exp\left[-50(V_Y/V_B - 0.2)^2\right]\sqrt{V_Y^2 + V_B^2}} \tag{7.1}$$

Finally, the evolution of the objective function associated with the best candidate at each generation is presented in Figure 7.2 (a). As we can notice, both initial populations performed relatively similar in terms of rate of convergence as well as in the value of the objective function at the end of each run. Also, from Figure 7.2 (b) we can state that from the 100 topologies used during each iteration, the number of admissible topologies oscillates around 70 for the first run and around 68 for the second run.

Additionally, the results of the optimization algorithm at the end of each routine are presented in Table 7.1. The values of the shear buckling load $V_B(\mathbf{x})$, shear yield load $V_Y(\mathbf{x})$, and objective function $f(\mathbf{x})$, are quite similar at the end of the optimization process regardless

of the initial population. However, we can observe from Figure 7.3 and Figure 7.4 that the evolution of the topologies is different for Population 1 and Population 2, respectively. It is expected that optimized topology from Figure 7.3 will dissipate energy through the yielding of the two horizontal interior links. On the other side, the yielding mechanism of the optimized topology illustrated in Figure 7.4 is expected to be yielding of its four interior vertical links. Additionally, the fact of having two different optimized shapes with different buckling and yield strength means that the algorithm was not able to find a global optimum topology.

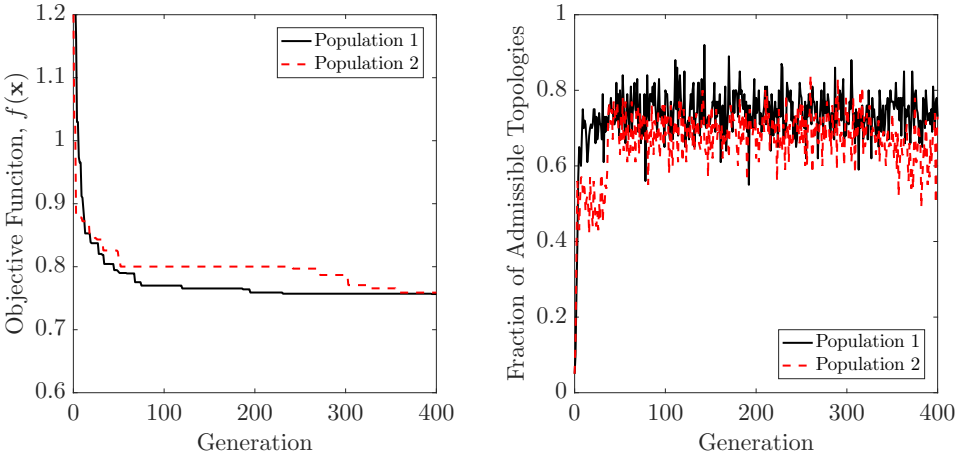

(a) (b)

Figure 7.2: Objective function and fraction of admissible topologies for $\overline{V_Y}/\overline{V_B} = 0.20$ and $\overline{Vol}(\mathbf{x}) = 0.40Vol$

Table 7.1: Reference case - Final results for $\overline{V_Y}/\overline{V_B} = 0.20$ and $\overline{Vol}(\mathbf{x}) = 0.40Vol$

$\overline{V_Y}/\overline{V_B}$	Population	V_B (kips)	V_Y (kips)	$f(\mathbf{x})$
0.20	1	209.70	41.42	0.757
	2	209.00	41.28	0.759

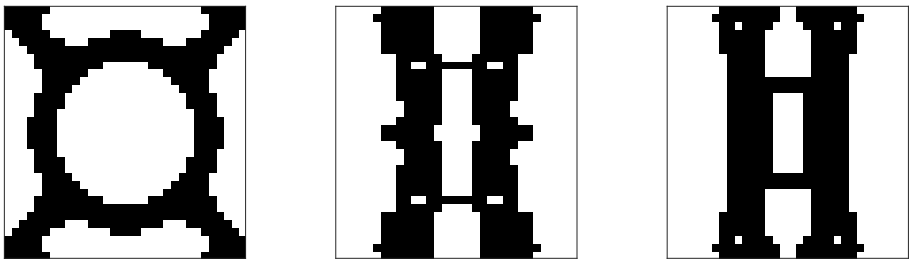

(a) Generation: 1 (b) Generation: 10 (c) Generation: 20

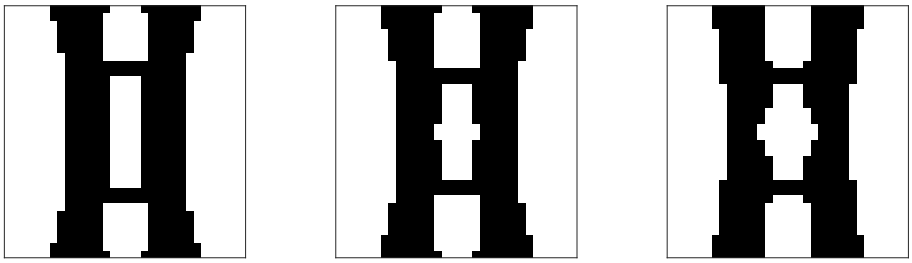

(d) Generation: 30 (e) Generation: 40 (f) Generation: 50

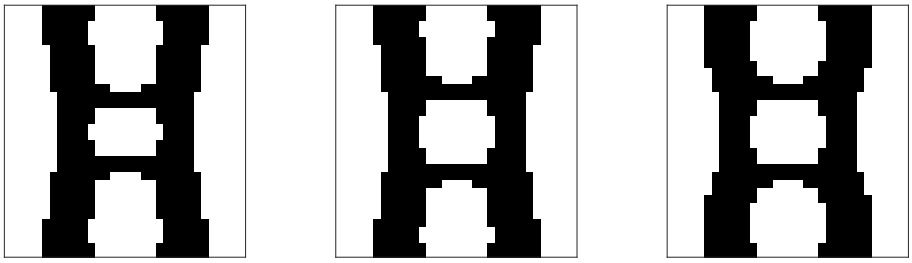

(g) Generation: 75 (h) Generation: 100 (i) Generation: 150

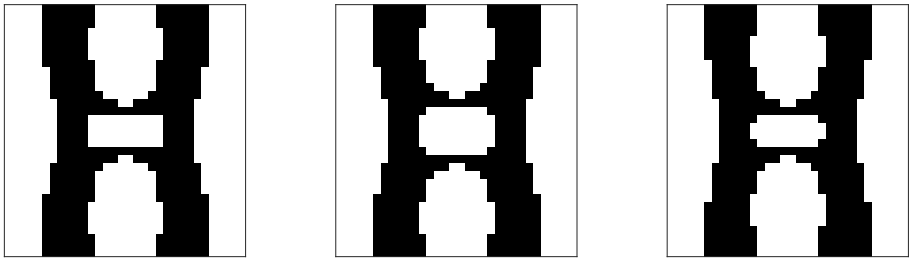

(j) Generation: 200 (k) Generation: 300 (l) Generation: 400

Figure 7.3: Evolution of topologies for $\overline{V_Y}/\overline{V_B} = 0.20$ and $\overline{Vol}(\mathbf{x}) = 0.40Vol$ - Population 1

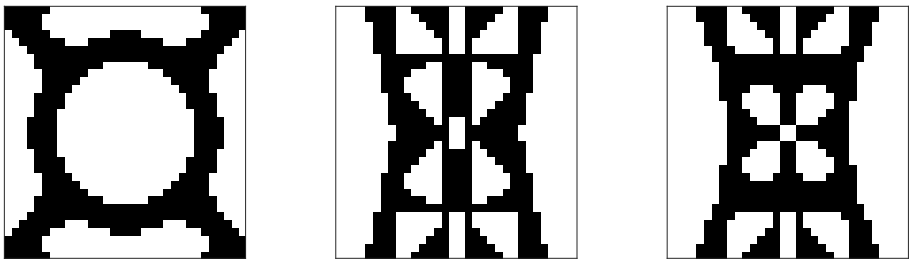

(a) Generation: 1 (b) Generation: 10 (c) Generation: 20

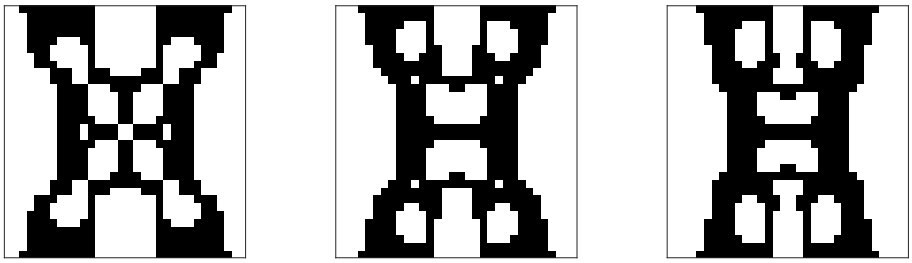

(d) Generation: 30 (e) Generation: 40 (f) Generation: 50

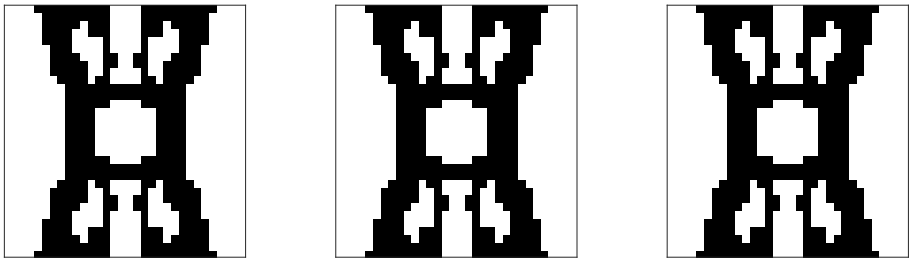

(g) Generation: 75 (h) Generation: 100 (i) Generation: 150

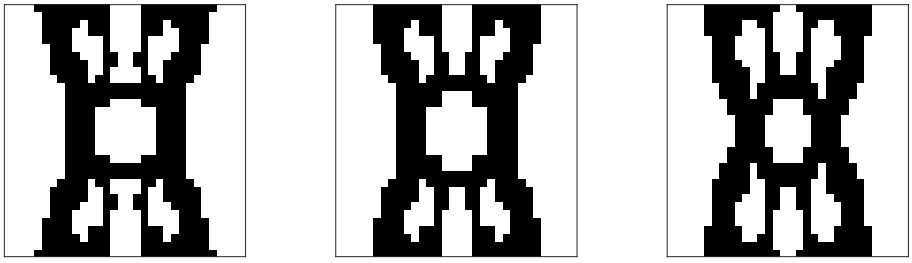

(j) Generation: 200 (k) Generation: 300 (l) Generation: 400

Figure 7.4: Evolution of topologies for $\overline{V_Y}/\overline{V_B} = 0.20$ and $\overline{Vol}(\mathbf{x}) = 0.40Vol$ - Population 2

7.2 Influence of the objective function bias, $\overline{V_Y}/\overline{V_B}$

Using the same domain and boundary conditions as those illustrated in Figure 7.1, we analyze the influence of the objective function bias $\overline{V_Y}/\overline{V_B}$ on the topology optimization algorithm. Hence, we keep the volume fraction constant but the value of the objective function bias varies. For the case when $\overline{Vol}(\mathbf{x}) = 0.40Vol$ and $\overline{V_Y}/\overline{V_B} = (0.10, 0.30)$, the objective function becomes Eq. 7.2 and Eq. 7.2, respectively.

$$f(\mathbf{x}) = \frac{280}{\sqrt{3}\exp\left[-50(V_Y/V_B - 0.1)^2\right]\sqrt{V_Y^2 + V_B^2}} \tag{7.2}$$

$$f(\mathbf{x}) = \frac{280}{\sqrt{3}\exp\left[-50(V_Y/V_B - 0.3)^2\right]\sqrt{V_Y^2 + V_B^2}} \tag{7.3}$$

From Figure 7.5 (a) and (b), we notice that decreasing the objective function bias to $\overline{V_Y}/\overline{V_B} = 0.10$ does not have an impact on the convergence of the algorithm nor in fraction of admissible topologies. Additionally, Figure 7.6 (a) and (b) show that the two independent initial populations evolved to the same final topology, where the yielding mechanism is located along the two interior horizontal links, which is very similar to the mechanism presented in Figure 7.4. Another observation comes from Table 7.2, where we can notice that the average values of the shear buckling load $\overline{V_B}(\mathbf{x})$ and shear yield load $\overline{V_Y}(\mathbf{x})$ decreased 7% and 46% respectively, compared to those average values from Table 7.1. This decrement of the shear yield strength in addition to a relatively constant shear buckling load is directly related to the fact that objective function bias changed from $\overline{V_Y}/\overline{V_B} = 0.20$ to $\overline{V_Y}/\overline{V_B} = 0.10$.

Similarly, Figure 7.5 (c) and (d) show that changing the objective function bias to $\overline{V_Y}/\overline{V_B} = 0.30$ does not influence the convergence nor the fraction of admissible topologies. Regarding the final topologies, Figure 7.6 (c) and (d) show the two final shapes generated by the evolution of two different initial populations. Both optimized topologies are similar in terms of the yielding mechanism, since both shapes will most likely dissipate energy through inelastic deformations localized in the two vertical interior links. Also, from Table 7.2 we

observe that the average value of the shear buckling load decreased 5% but the average shear yield load increased 45% compared to the average values from Table 7.1. Since the shear buckling load stays relatively constant, the increment in the value of objective function bias is reflected in the shear yield load.

The similarity between optimized topologies regardless of the objective function bias is also present for different volume fractions, as observed in Appendix B.3. Although the yielding mechanism may change a little, two solid legs linked together by weaker elements appears to be the optimized geometrical configuration for resisting buckling. Another key concept is that shear buckling load V_B, reaches an upper limit no matter the objective function bias used in the optimization algorithm. This concept is corroborated by the values of V_B shown in Table B.4, where we can observe that for a given volume fraction, there is not much variation in the shear buckling load when the objective function bias changes from $\overline{V_Y}/\overline{V_B} = 0.10$ to $\overline{V_Y}/\overline{V_B} = 0.30$.

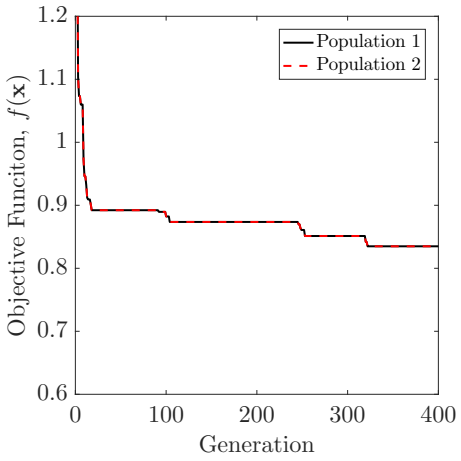

(a) $\overline{V_Y}/\overline{V_B} = 0.10$

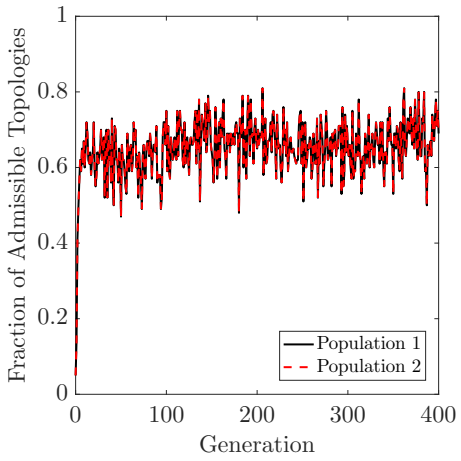

(b) $\overline{V_Y}/\overline{V_B} = 0.10$

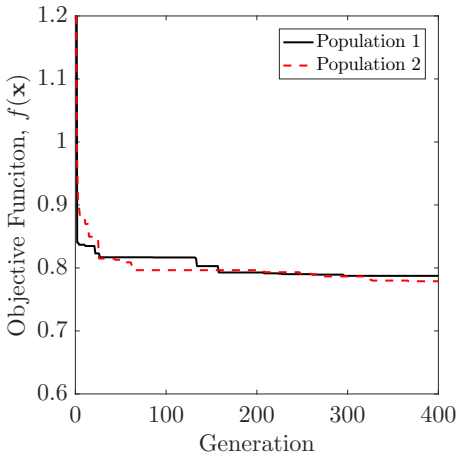

(c) $\overline{V_Y}/\overline{V_B} = 0.30$

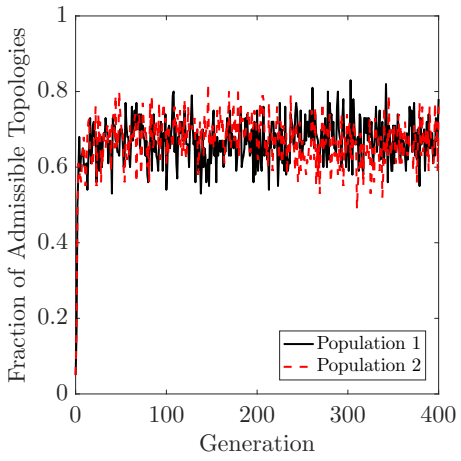

(d) $\overline{V_Y}/\overline{V_B} = 0.30$

Figure 7.5: Bias influence - Objective function and fraction of admissible topologies for $\overline{Vol}(\mathbf{x}) = 0.40Vol$

Table 7.2: Bias influence - Final results for $\overline{Vol}(\mathbf{x}) = 0.40Vol$

$\overline{V_Y}/\overline{V_B}$	Population	V_B (kips)	V_Y (kips)	$f(\mathbf{x})$
0.10	1	194.60	22.46	0.835
	2	194.60	22.46	0.835
0.30	1	199.60	60.08	0.787
	2	198.90	59.43	0.779

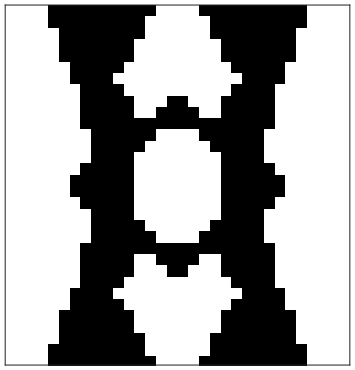

(a) $\overline{V_Y}/\overline{V_B} = 0.10$ - Population 1

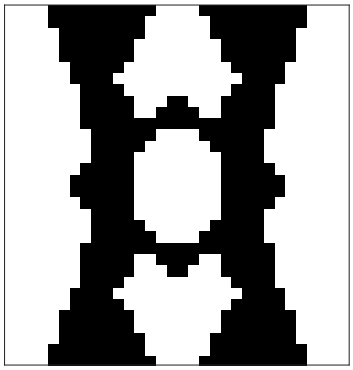

(b) $\overline{V_Y}/\overline{V_B} = 0.10$ - Population 2

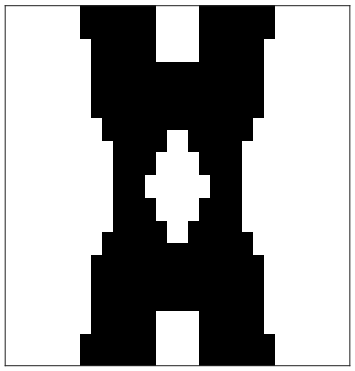

(c) $\overline{V_Y}/\overline{V_B} = 0.30$ - Population 1

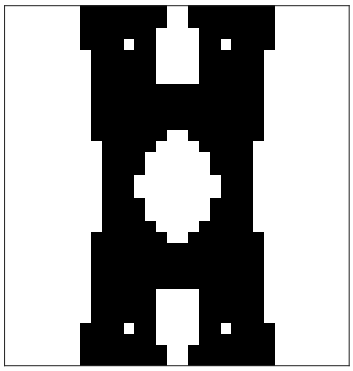

(d) $\overline{V_Y}/\overline{V_B} = 0.30$ - Population 2

Figure 7.6: Bias influence - Final optimized topologies for $\overline{Vol}(\mathbf{x}) = 0.40Vol$

7.3 Influence of the volume fraction, $\overline{Vol}(\mathbf{x}) = \Delta Vol$

By using the domain and boundary conditions illustrated in Figure 7.1, in addition to an objective function bias $\overline{V_Y}/\overline{V_B} = 0.20$, we vary the prescribed volume fraction in order to analyze its influence on the overall performance of the topology optimization algorithm. It is important to note that this variation of the prescribed volume fraction influences the initial population, hence a new set of initial topologies are generated according to the same ideas described in Section 6.4.4. Then, for the case when $\overline{Vol}(\mathbf{x}) = (0.30Vol, 0.50Vol)$, the objective function becomes Eq. 7.4 and Eq. 7.5 respectively.

$$f(\mathbf{x}) = \frac{210}{\sqrt{3}\exp\left[-50(V_Y/V_B - 0.2)^2\right]\sqrt{V_Y^2 + V_B^2}} \tag{7.4}$$

$$f(\mathbf{x}) = \frac{350}{\sqrt{3}\exp\left[-50(V_Y/V_B - 0.2)^2\right]\sqrt{V_Y^2 + V_B^2}} \tag{7.5}$$

When the volume fraction is $\overline{Vol}(\mathbf{x}) = 0.30Vol$, there is not further improvement of the objective function after generation 90 approximately, as we can observe in Figure 7.7 (a). Also, from Figure 7.7 (b) we notice that the fraction of admissible topologies during the optimization routine decreased to an average of 55, in contrast to 69 admissible topologies when the volume fraction was equal to $\overline{Vol}(\mathbf{x}) = 0.40Vol$. Hence, reducing the volume fraction is potentially associated with an early convergence of the genetic algorithm and with a decrement in the number of admissible shapes. In terms of the final topologies, Figure 7.8 (a) and (b) show that both populations evolved into a similar yielding mechanism, where the two horizontal interior links will undergo plastic deformations and thus dissipate energy. Finally, Table 7.3 shows that the average shear buckling and shear yield loads decreased 33% and 46% respectively, compared to their corresponding averages when $\overline{Vol}(\mathbf{x}) = 0.40Vol$.

On the other hand, if the volume fraction is $\overline{Vol}(\mathbf{x}) = 0.50Vol$, Figure 7.7 (d) shows that the number of admissible individuals increases to an average of 80 topologies, and Figure 7.7 (c) indicates that the algorithm does not reaches a state of convergence within the very

early generations. In this specific case each initial population evolved into a different final topology. While the topology illustrated by Figure 7.8 (c) will dissipate energy through the inelastic deformations in the interior horizontal links, Figure 7.8 (d) shows a different final shape where yielding of the vertical links is the potential energy dissipation mechanism. Once again we can notice from Table 7.3 that the average shear buckling and shear yield load increased 35% compared to their corresponding values from Table 7.1.

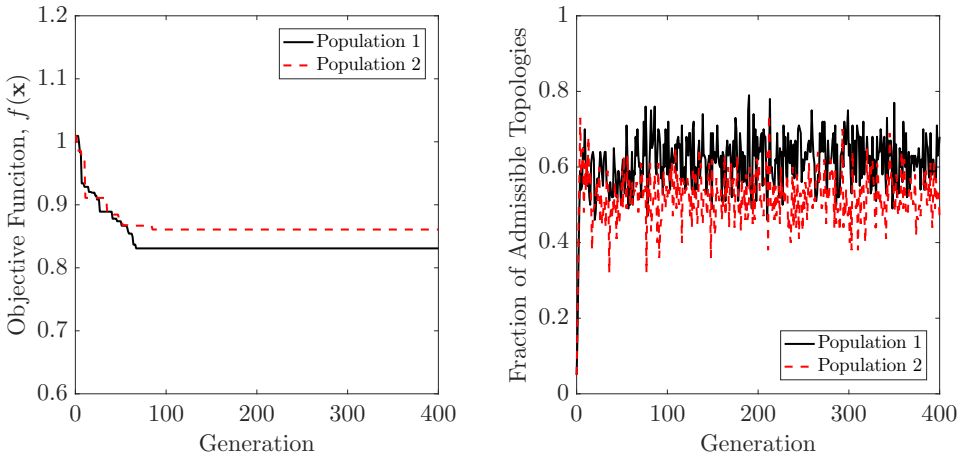

(a) $\overline{Vol}(\mathbf{x}) = 0.30Vol$ (b) $\overline{Vol}(\mathbf{x}) = 0.30Vol$

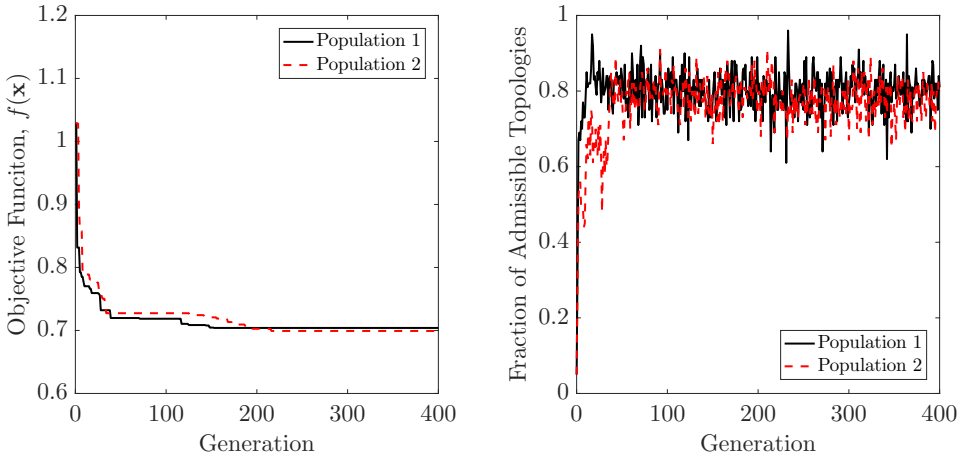

(c) $\overline{Vol}(\mathbf{x}) = 0.50Vol$ (d) $\overline{Vol}(\mathbf{x}) = 0.50Vol$

Figure 7.7: Volume fraction influence - Objective function and fraction of admissible topologies for $\overline{V_Y}/\overline{V_B} = 0.20$

Table 7.3: Volume fraction influence - Final results for $\overline{V_Y}/\overline{V_B} = 0.20$

$\overline{Vol}(\mathbf{x})$	Population	V_B (kips)	V_Y (kips)	$f(\mathbf{x})$
0.30Vol	1	143.20	28.22	0.831
	2	139.20	26.32	0.861
0.50Vol	1	282.70	54.34	0.704
	2	283.40	56.95	0.699

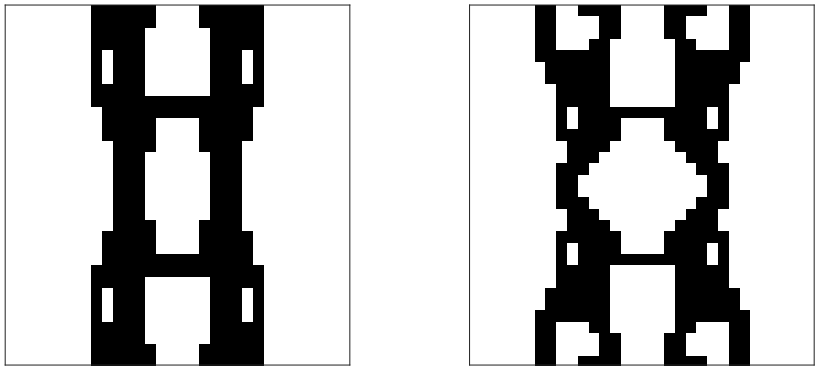

(a) $\overline{Vol}(\mathbf{x}) = 0.30Vol$ - Population 1 (b) $\overline{Vol}(\mathbf{x}) = 0.30Vol$ - Population 2

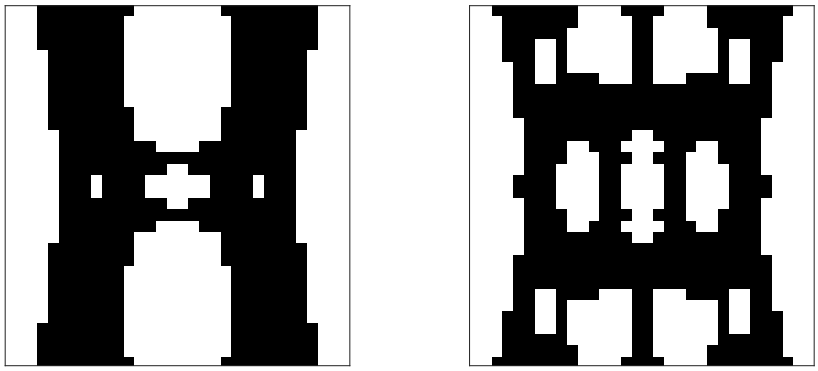

(c) $\overline{Vol}(\mathbf{x}) = 0.50Vol$ - Population 1 (d) $\overline{Vol}(\mathbf{x}) = 0.50Vol$ - Population 2

Figure 7.8: Volume fraction influence - Final optimized topologies for $\overline{V_Y}/\overline{V_B} = 0.20$

7.4 Influence of the scale factor

All the optimized topologies obtained in previous sections are based on a domain with constant geometric dimensions (i.e. width, height and thickness). Hence, it is important to analyze whether these optimized topologies are still useful when these geometric dimensions are scaled. In other words, we will analyze the impact of the geometric scale factor on the ratio V_Y/V_B. Hence, two scale factors are introduced to modify the height, width and thickness of the optimized topology. The parameter α scales the height and width of the shape whereas the parameter β controls its thickness, as illustrated in Figure 7.9. Then, the shear buckling load and shear yield load are calculated using the procedures described in Sections 4.3 and Section 4.4, respectively. It is worth mentioning that the same 32 by 32 finite element mesh as well as the boundary conditions detailed in Figure 7.1 are used in this parametric study.

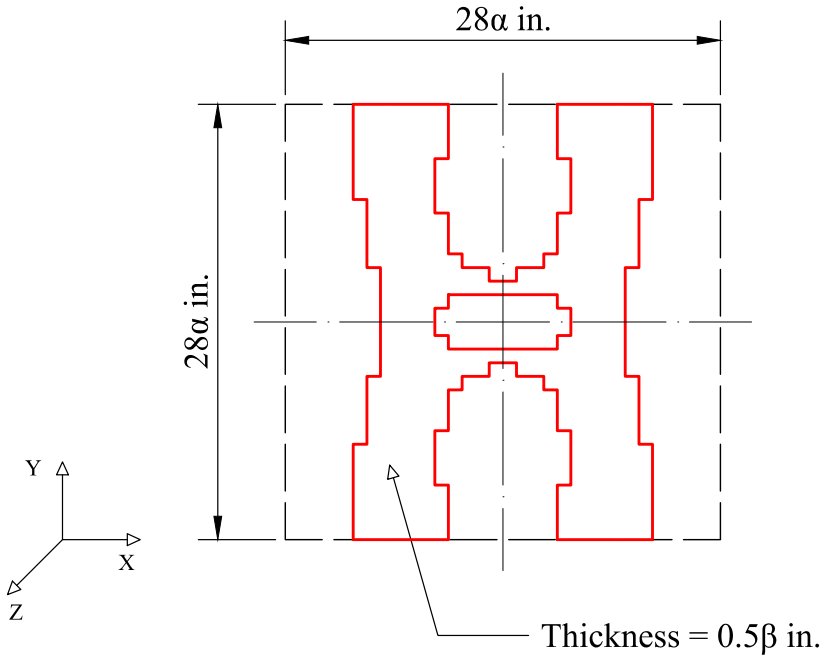

Figure 7.9: Illustration of the parameterized domain

In this parametric analysis we consider a variation of the scale factors α and β from 1

to 4 with increments of 0.1. After obtaining V_Y/V_B for all the combinations of the two scale parameters, we normalize all these values by the $\overline{V_Y}/\overline{V_B}$ ratio associated with the original topology, i.e. when $\alpha = 1$ and $\beta = 1$.

From Figure 7.10 (a) we can observe that the shear buckling load V_B has logarithmic behavior in terms of the height and width scale factor α, whereas the shear yield load V_Y is directly proportional to α. Along the same lines, Figure 7.10 (b) shows that the shear buckling load V_B has an exponential behavior in terms of the thickness scale factor β, and V_Y is directly proportional to the scale factor β.

Finally, Figure 7.10 (c) illustrates the change in the V_Y/V_B ratio as a function of each the scale factor α and β. We can observe that if we scale all the three geometric dimensions by the same factor, the V_Y/V_B ratio remains unaltered, i.e. we would expect the same amount of yielding prior to buckling as in the original shape. Additionally, we can modify the original V_Y/V_B ratio if we set $\alpha \neq \beta$. More specifically, if we set $\alpha > \beta$ or $\alpha < \beta$ we will experience an increment or decrement of the current V_Y/V_B ratio compared to the original one, respectively.

As a side note we should mention that we obtained the same trend plots no matter the topology used in the parametric analysis, hence this information applies for all the optimized topologies obtained throughout this study.

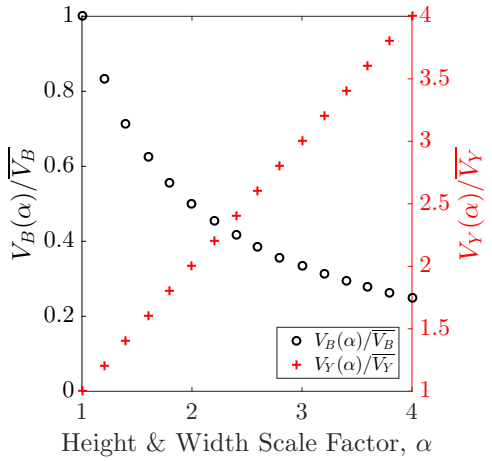

(a) Influence of α in $V_B(\mathbf{x})$ and $V_Y(\mathbf{x})$

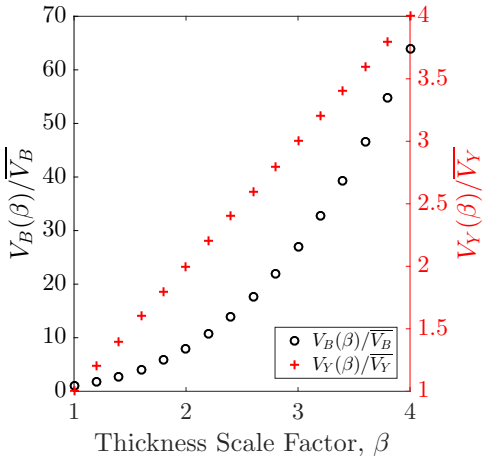

(b) Influence of β in $V_B(\mathbf{x})$ and $V_Y(\mathbf{x})$

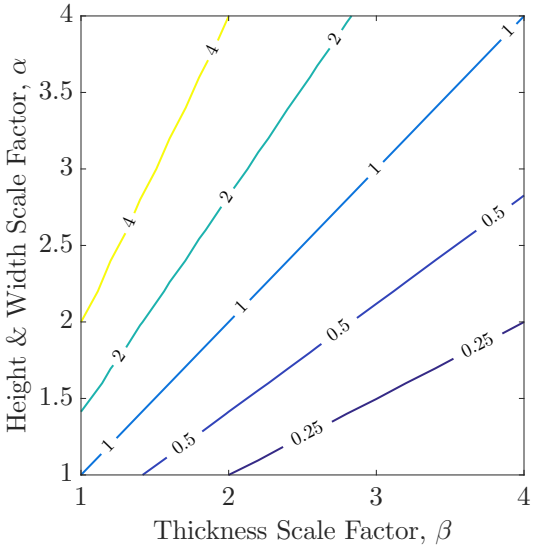

(c) $V_Y(\mathbf{x})/V_B(\mathbf{x})$ as a function of α and β

Figure 7.10: Influence of the scale factors α and β on the $V_Y(\mathbf{x})/V_B(\mathbf{x})$ ratio

Chapter 8

Monotonic FE Analysis of Optimized Topologies

The main goal in this chapter is to analyze whether the optimization routine satisfied the objective of preventing buckling in a structural fuse under the action of monotonically applied displacement. Hence, a set of nine optimized topologies are analyzed using finite element models. These topologies cover all the scenarios in terms of the volume fraction $\overline{Vol}(\mathbf{x}) = \Delta Vol$, and the objective function bias $\overline{V_Y}/\overline{V_B}$.

The analysis procedure involves a pre-processing of the geometry and then the models are subjected to a monotonic displacement protocol. This analysis is used to obtain the response of the optimized fuse over an increasing lateral displacement. While keeping the bottom edge fixed, we apply a horizontal displacement in all the nodes along the top edge of the fuse equal to 2.52 in. By neglecting the deformation of the solid boundary elements, this horizontal displacement corresponds to a drift angle of 0.09 radians, which is in accordance with AISC 341, as the final rotation angle imposed on an eccentrically braced frame link-to-column connection specimen (AISC, 2016). The reaction force as well as the applied displacement are recorded and used to construct the pushover curve. Additionally, the maximum out of plane displacement is also recorded to approximately measure the level of

buckling at each specific drift angle.

8.1 Geometric interpretation of the optimized topologies

Before analyzing the monotonic and cyclic response of the optimized fuses, each geometry is converted into a smoothed version of its coarse predecessor. The main intention is to prevent stress localization due to an abrupt discontinuity along the fuse's boundary. To accomplish this goal, simple geometric entities such as lines, circles, ellipses and three-point arcs are used to interpret the geometries. Additionally, the re-entrant corner connecting the shape with the boundary elements is smoothed using a circle with a radius of 0.5 in. The final result of this pre-processing stage is illustrated in Figure 8.1, where the name of each topology corresponds the volume fraction, objective function bias and initial population from which each optimized shape was obtained. Finally, a 28 in. by 2 in. solid boundary element should be added to both ends of the topology in order to get a better representation of the geometry and boundary conditions of the fuse.

Please refer to Appendix C for the geometric dimensions of the interpreted topologies.

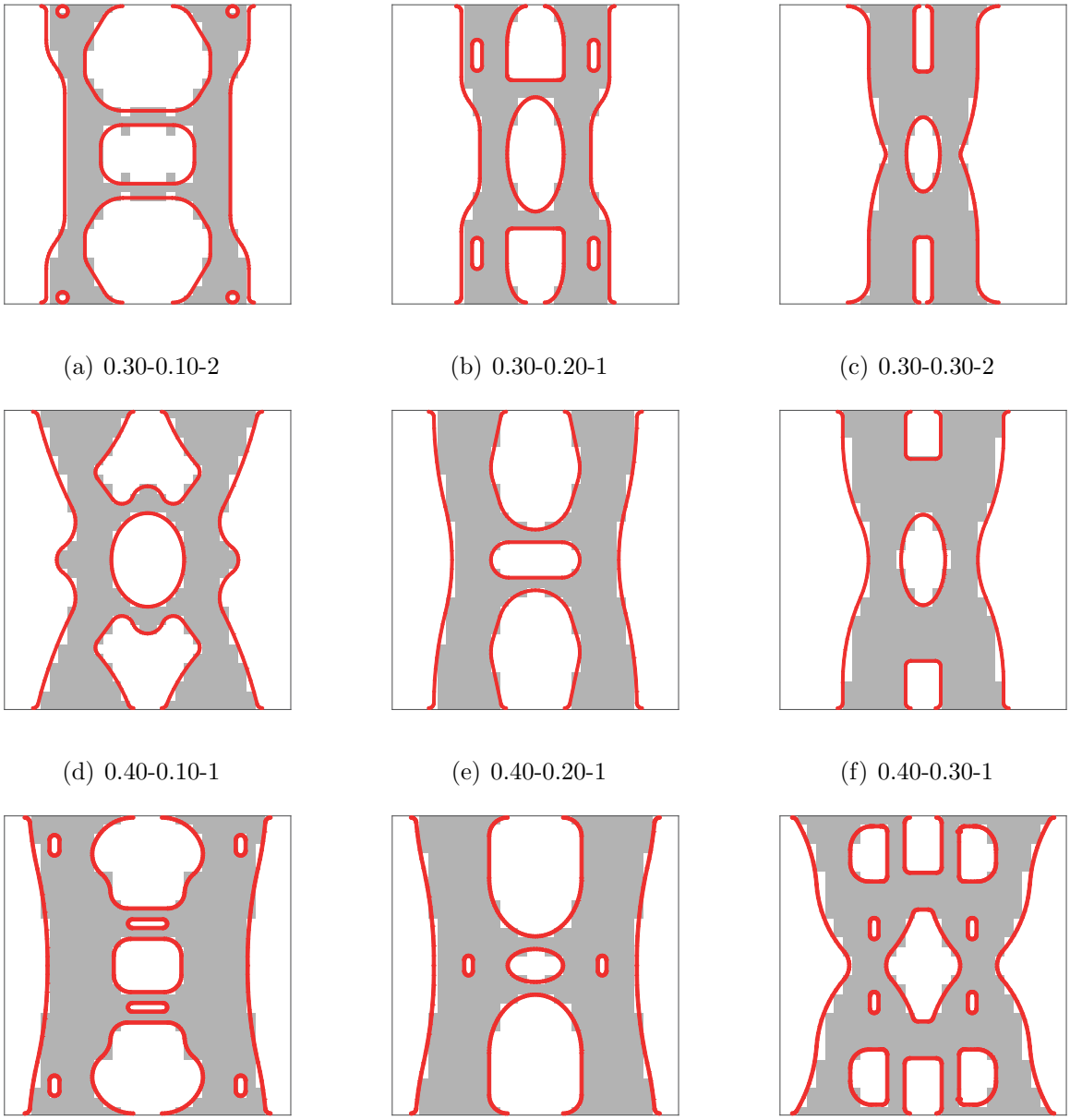

(a) 0.30-0.10-2 (b) 0.30-0.20-1 (c) 0.30-0.30-2

(d) 0.40-0.10-1 (e) 0.40-0.20-1 (f) 0.40-0.30-1

(g) 0.50-0.10-2 (h) 0.50-0.20-1 (i) 0.50-0.30-1

Figure 8.1: Set of interpreted topologies corresponding to $\Delta Vol - \overline{V_Y}/\overline{V_B} - Population$

8.2 Finite element model

After adding a 28 in. by 2 in. solid boundary element to both ends of the topology, the finite element model of each fuse was created using full integration 4-node shell elements. All the elements have a thickness equal to $t = 0.50\ in$ and the number of through-thickness integration points is set to 5. The ASTM A572 Gr 50 steel plate material was modeled using an isotropic elastic model with a Youngs modulus equal to $E = 29000\ ksi$ and a Poissons ratio of $\nu = 0.3$ in addition to a kinematic hardening rule with $F_Y = 50\ ksi$ and a hardening slope equal to 1% of the Youngs modulus, $H = 290\ ksi$.

A reference point used to apply the lateral displacement is created in the middle of the top edge of the fuse and a rigid body tie constraint couples the the movement of this master node with all the nodes along the top edge of the fuse, as shown in Figure 8.2 (a). Finally, all the degrees of freedom at the top and bottom edges of the fuse (excluding the horizontal displacement of the top edge) are restrained.

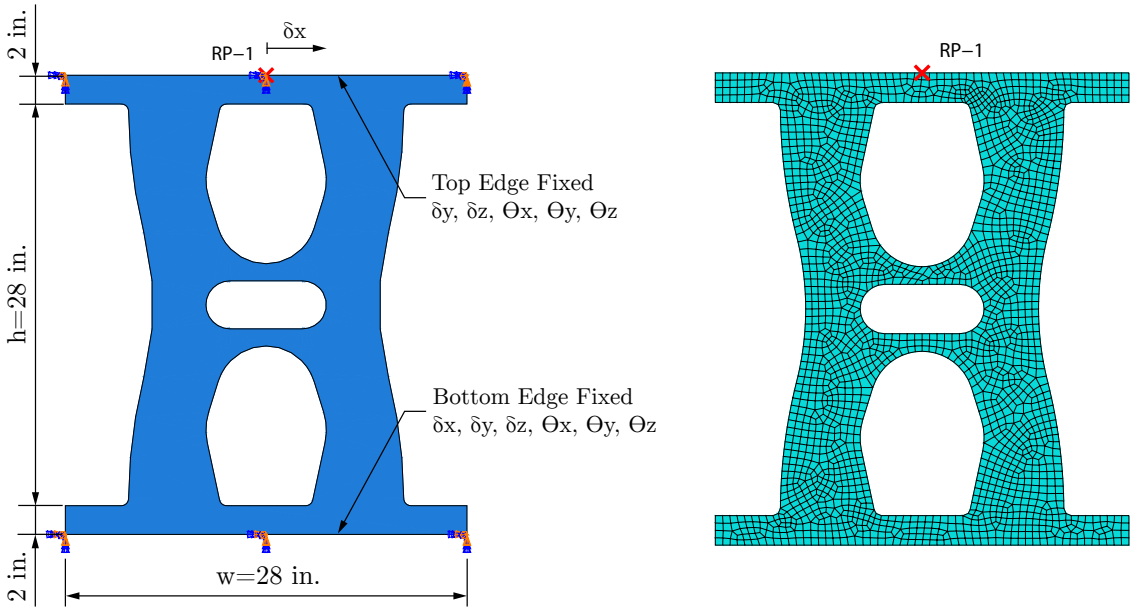

(a) Geometry and boundary conditions

(b) Finite element mesh

Figure 8.2: Abaqus finite element model for Topology 0.40-0.20-1

The domain is discretized using a free structured mesh with an an average size of 0.5 in., as illustrated in Figure 8.2 (b). Finally, the monotonic pushover analysis is performed in two steps:

1. To account for initial imperfections in the geometry, a linear buckling analysis is performed and the first four buckling shapes are obtained. Then, the first buckling mode is scaled by a factor of $h'/250$ and used as the initial imperfection of the model. The total height h' is equal to the fuse's height h plus the height of the two boundary elements. As an example, the first four buckling modes of Topology 0.40-0.20-1 are illustrated in Figure 8.3.

2. After the initial imperfections have been included, a static general solver is used to run the pushover analysis. Due to the potential large deformations related to the buckling phenomenon, the model is assumed to be geometric nonlinear. Finally, at each converged iteration, the output parameters are: displacements, reaction forces, von Mises stresses and equivalent plastic strains.

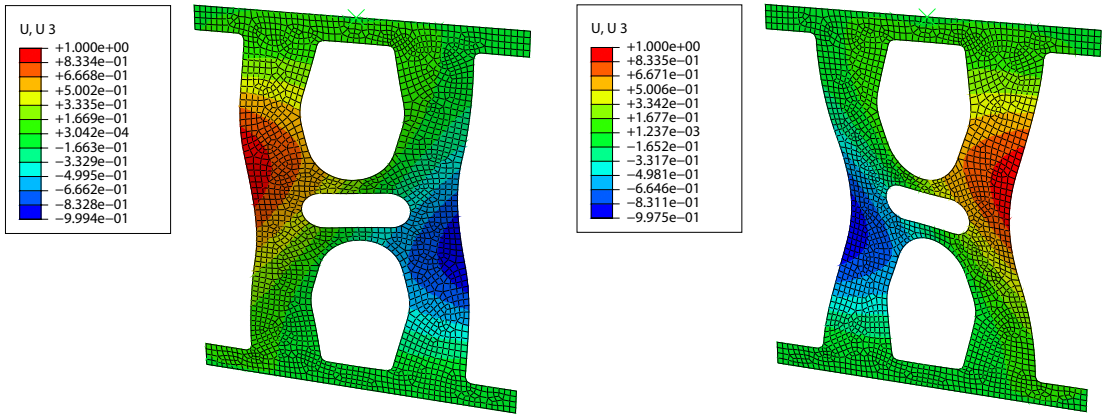

(a) Buckling Shape 1 - $V_B = 188\,kips$ (b) Buckling Shape 2 - $V_B = -188\,kips$

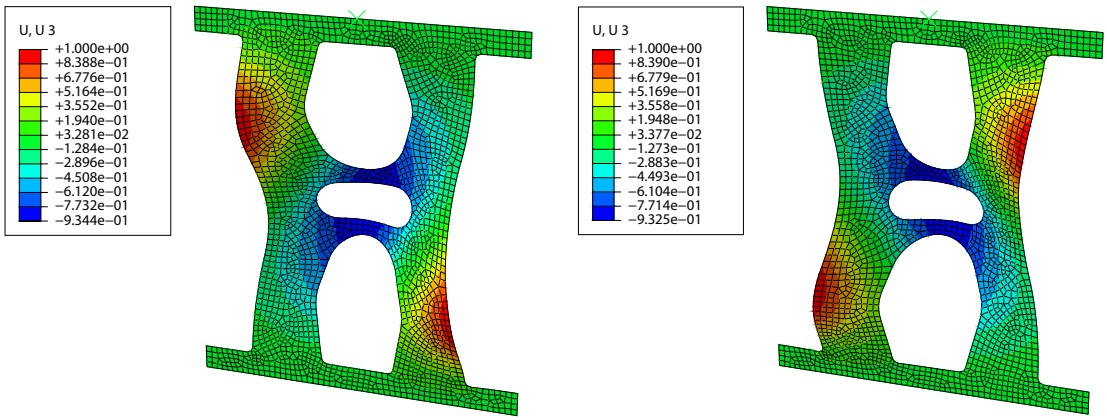

(c) Buckling Shape 3 - $V_B = 208\,kips$ (d) Buckling Shape 4 - $V_B = -208\,kips$

Figure 8.3: Buckling shapes for Topology 0.40-0.20-1

8.3 Output parameters

After performing the pushover analysis, the output information is processed to obtain parameters that will allow us determine if the new optimized topologies are able to delay buckling. This set of parameters is described in the following paragraphs:

- The mechanism through which the fuse transforms global shear deformations into local yielding mechanisms is obtained by analyzing the von Mises stress contour plot. When

the level of applied horizontal displacement reaches the corresponding yield drift, those regions of material with a von Mises stress value greater than $F_Y = 50\ ksi$ lead to the formation of plastic hinges and thus the fuse is able to dissipate energy.

- The initial stiffness, yield force and yield drift are calculated based on the monotonic response of the fuse. First, the monotonic curve is obtained by plotting the horizontal reaction force and the applied horizontal displacement at the reference point. Then, the initial stiffness K_I of the fuse is calculated using the first two consecutive points of the force-displacement plot. Finally, the yield point is the first point where the tangent stiffness is less than 20% of the initial stiffness. The x-coordinate of this point corresponds to the yield drift δ_Y, and the y-coordinate to the yield force V_Y. We should mention that each curve was examined individually to ensure that this method to obtain the yield point produced reasonable results.

- The post-yield stiffening related to an increment in the bearing capacity of the fuse after reaching the yield point is associated with the hardening material model in addition to the geometric stiffening of the fuse i.e. the transition from flexural to axial deformations at large drift levels. This parameter is equal to the maximum force exhibit by the fuse during the pushover analysis V_{max}, divided by the yield force V_Y.

- One simple way to measure the level of buckling as a function of the out-of-plane displacements is to track the evolution of the U_3 displacement component of an specific node. In this case, the selected node corresponds to the node with the maximum out-of-plane displacement at the end of the loading protocol. In order to have a unitless parameter, the U_3 component is divided by the height of the fuse h.

It is worth mentioning that the output data generated by the ring shaped fuse (designated as RS) as well as the butterfly shaped fuse (designated as BF2) are included for comparison purposes. Also, the V_Y/V_B ratio for these previously studied shapes is summarized in Table 8.1.

Table 8.1: V_Y/V_B for the ring shaped and butterfly shaped structural fuses

$\overline{Vol}(\mathbf{x})$	Shape	V_Y/V_B
$0.30Vol$	RS	0.17
	$BF2$	0.20
$0.40Vol$	RS	0.18
	$BF2$	0.26
$0.50Vol$	RS	0.26
	$BF2$	0.34

8.4 Results and discussion

8.4.1 Yielding mechanism

The yielding mechanism by which each fuse dissipates energy is obtained by analyzing its corresponding von Mises stress contour plot. Since all the finite element models consider an ASTM A572 Gr 50 steel plate with $F_Y = 50\ ksi$, the regions within the fuse with a von Mises stress greater than or equal to 50 ksi are considered part of the yielding mechanism.

As a reference case, the von Mises stress distribution corresponding to the yield displacement is illustrated in Figure 8.4 for all of those topologies within the category $\overline{Vol}(\mathbf{x}) = 0.40Vol$. In the ring shaped structural fuse, the von Mises stress distribution indicates that four plastic hinges formed next to one side of the links which connects the ring with the boundary elements. Along the same lines, the contour plot of the von Mises stress for the butterfly shaped structural fuse indicates plastic deformations along the edges of the two vertical fuses with some amount of yielding propagating towards the boundary elements. It is worth mentioning that these two yielding mechanisms were expected to happen

according to the results presented by Egorova et al. (2014) and Ma et al. (2010), respectively.

For the optimized topology corresponding to an objective function bias of $\overline{V_Y}/\overline{V_B} = 0.10$, the von Mises stress distribution illustrated in Figure 8.4 (c) shows two well localized plastic hinges in the two interior horizontal links. We can also notice that if we continue increasing the lateral displacement, an additional set of plastic hinges will form in the reduced section of the two vertical legs of the fuse. For the optimized shape obtained with an objective function bias of $\overline{V_Y}/\overline{V_B} = 0.20$, Figure 8.4 (d) illustrates the von Mises stress distribution within the fuse. Once again the plastic deformations take place in well localized regions near the two ends of the horizontal links. Also, by increasing the applied lateral displacement, additional plastic hinges form in the vertical legs of the fuse, more specifically in those regions close to the boundary elements.

In contrast to earlier findings, by increasing the objective function bias to $\overline{V_Y}/\overline{V_B} = 0.30$, the resulting optimized topology does not present a well defined plastic mechanism. Although the von Mises stress distribution indicates the presence of plastic deformations at the mid-height of the fuse, additional plastic regions are present in the horizontal links as well as in the transition regions near the boundary elements, as illustrated in Figure 8.4 (e).

Similar conclusions can be derived based on the yielding mechanisms corresponding to those topologies with $\overline{Vol}(\mathbf{x}) = 0.30Vol$ and $\overline{Vol}(\mathbf{x}) = 0.50Vol$. Please refer to Appendix D.2 for further details.

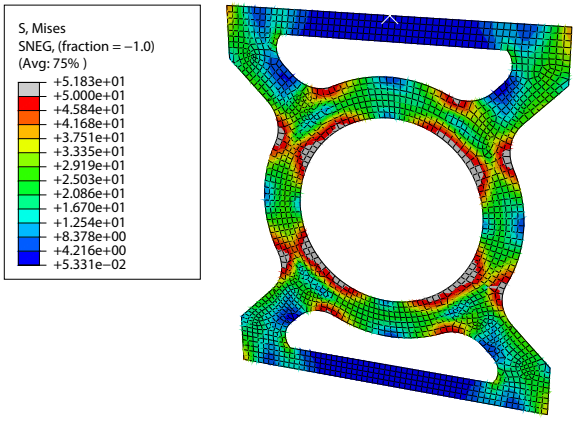

(a) Ring Shaped

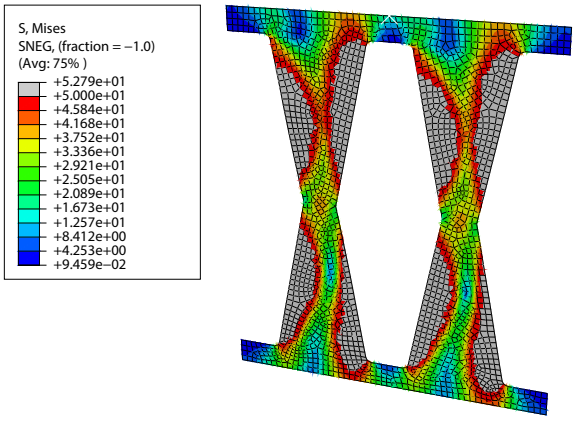

(b) Butterfly Shaped

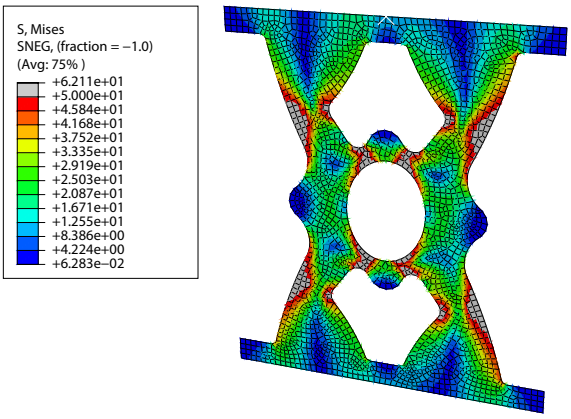

(c) 0.40-0.10-1

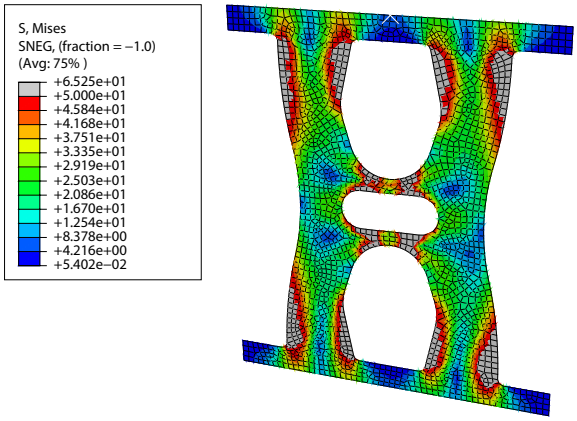

(d) 0.40-0.20-1

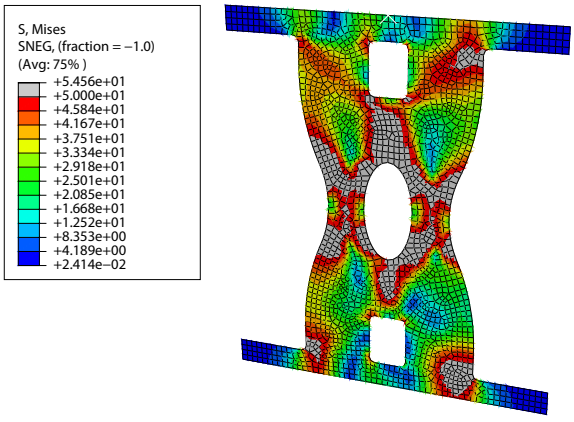

(e) 0.40-0.30-1

Figure 8.4: Von Mises stress distribution at $\delta = \delta_Y$ for $\overline{Vol}(\mathbf{x}) = 0.40Vol$

8.4.2 Initial stiffness

From the pushover curves illustrated in Figure 8.5 (a), we can observe how the initial stiffness varies for the different optimized topologies. Also, the pushover response reveals that the ring shaped fuse is the weaker topology in terms of strength. This observation is also valid for the other volume fractions, as we can observe in the pushover plots presented in Appendix D.3.

Comparing only the optimized topologies, we can state that the bigger the value of the prescribed objective function bias $\overline{V_Y}/\overline{V_B}$, the larger the initial stiffness of the optimized topology. Moreover, this trend holds even when the volume fraction is increased or decreased, as we can note from Figure 8.5 (b). In conclusion, an optimized topology with a higher initial stiffness can be obtained if we use bigger value of the objective function bias during the optimization routine. Also, a direct consequence of increasing or decreasing the prescribed volume fraction is that for a given objective function bias, the higher initial stiffness is associated with the larger volume of material.

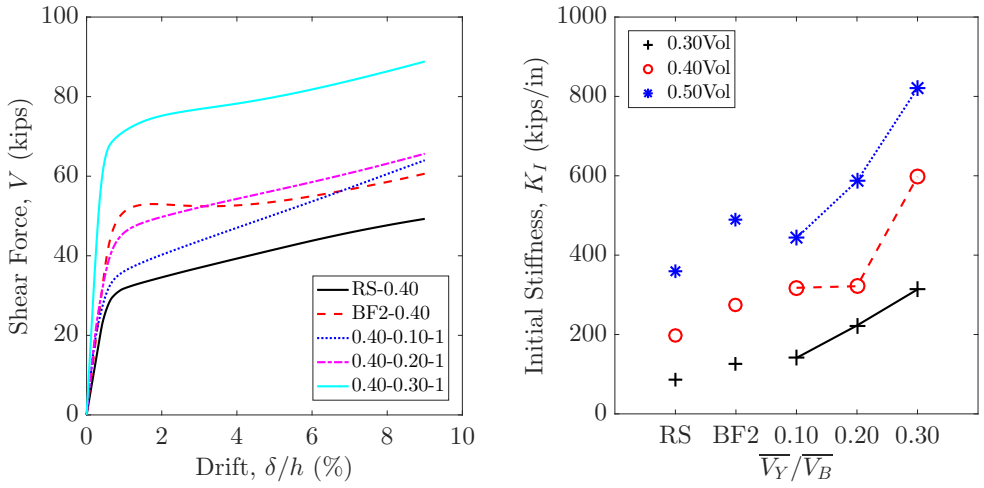

(a) Topology: ΔVol - $\overline{V_Y}/\overline{V_B}$ - Population (b) Trend plot of the initial stiffness

Figure 8.5: Pushover curves - Initial stiffness K_I as a function of the volume fraction $\overline{Vol}(\mathbf{x}) = \Delta Vol$ and the objective function bias $\overline{V_Y}/\overline{V_B}$

A summary of the initial stiffness values K_I, obtained from the monotonic pushover curves can be found in Table 8.2.

Table 8.2: Results from the monotonic pushover analysis

Model	K_I (kips/in)	V_Y (kips)	δ_Y/h (%)	V_{max}/V_Y	U_3/h at δ_Y (%)	U_3/h at δ_F (%)
RS-0.30	87	15	0.82	1.76	0.01	0.22
BF2-0.30	125	29	1.07	1.40	0.06	0.80
0.30-0.10-2	141	17	0.74	2.10	0.04	0.12
0.30-0.20-1	223	32	0.78	1.53	0.16	2.36
0.30-0.30-2	314	41	0.64	1.25	0.26	5.59
RS-0.40	198	30	0.69	1.66	0.07	0.94
BF2-0.40	274	49	0.84	1.23	0.31	4.00
0.40-0.10-1	318	33	0.62	1.97	0.09	0.46
0.40-0.20-1	322	43	0.76	1.52	0.10	1.85
0.40-0.30-1	598	66	0.54	1.34	0.35	6.20
RS-0.50	360	49	0.68	1.21	0.09	4.47
BF2-0.50	490	78	0.73	1.11	0.05	5.27
0.50-0.10-2	443	42	0.51	1.91	0.07	0.97
0.50-0.20-1	587	59	0.62	1.61	0.02	2.56
0.50-0.30-1	821	88	0.51	1.23	0.05	6.79

8.4.3 Yield point

Based on defining the yield point as the point where the current stiffness is less than 20% of the initial stiffness K_I, the trend plots for the corresponding yield force and yield drift are presented in Figure 8.6 (a) and (b) respectively.

From Figure 8.6 (a) we can observe that the ring shaped fuse has the smaller yield strength, except when $\overline{Vol}(\mathbf{x}) = 0.50Vol$. On the other hand, the optimized topologies have the largest yield strength of its corresponding group when the objective function bias is $\overline{V_Y}/\overline{V_B} = 0.30$. If we consider only the optimized topologies, it is clear that a bigger value of the objective function bias will produce a topology with a larger yield strength. Additionally, we can state that for a given objective function bias, a bigger volume fraction implies a larger value of the yield strength.

Along the same lines, by analyzing Figure 8.6 (b), we observe that the different yield drifts corresponding to the different variations of the ring shaped fuse are relatively close to each other with an average value of 0.73%, whereas the butterfly shaped topologies exhibit a wider range in terms of the yield drift, with an average yield drift equal to 0.88%. For the case of the optimized shapes, there is not a single trend for the yield drift in terms of the objective function bias $\overline{V_Y}/\overline{V_B}$. Although we could say that for a specific objective function bias the yield drift decreases with an increment in the volume fraction, from a general perspective we could also represent the yield drift of all the optimized topologies by an average yield drift value equal to 0.64%.

Table 8.2 contains the summary of all the yield forces and yield drifts for all the analyzed topologies.

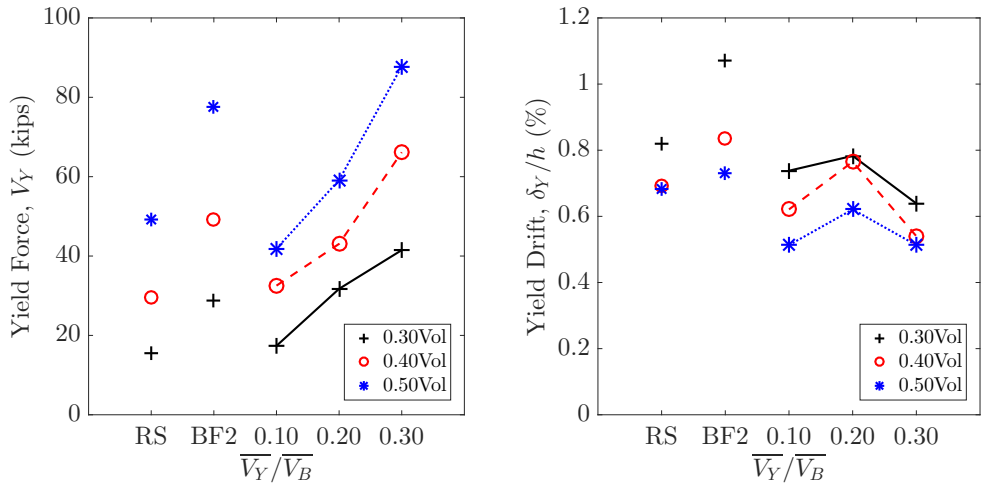

(a) Trend plot of the yield force

(b) Trend plot of the yield drift

Figure 8.6: Yield point as a function of the volume fraction $\overline{Vol}(\mathbf{x}) = \Delta Vol$ and the objective function bias $\overline{V_Y}/\overline{V_B}$

8.4.4 Post-yield stiffening

The post-yield stiffening behavior of each topology can be graphically observed by normalizing the pushover curves by its corresponding yield force V_Y. Figure 8.7 (a) illustrates the normalized monotonic response of those topologies with a volume fraction equal to $\overline{Vol}(\mathbf{x}) = 0.40Vol$. If we focus on the optimized topologies only, we can observe that the larger the objective function bias, the smaller the post-yield stiffening of the optimized topology. Also, the similarity in the initial stiffness means that if we scale the optimized topologies with different objective function bias to have the same strength, then the stiffness will be the same too. These two observations are also present in the remaining normalized pushover curves corresponding to different volume fractions found in Appendix D.3.

Likewise, the trend plot illustrated in Figure 8.7 (b) shows a close proximity between the trend lines of different volume fractions. Hence, we could state that the post-yield stiffening is a function of the objective function bias and it is not heavily influenced by the

volume of material.

The fact that the highest post-yield stiffening corresponds to those optimized fuses with an objective function bias of $\overline{V_Y}/\overline{V_B} = 0.10$ could be attributed to the geometric stiffening of the shape and the hardening that the material is experiencing. For instance, after the yield point the interior horizontal links (Figure 8.4 (c), Figure D.9 (c) and Figure D.10 (a)) no longer act as flexural links but rather as tension members. It triggers a rapid accumulation of plastic deformations that may cause an unrealistic hardening of the material.

Table 8.2 summarizes all the post-yield stiffening values corresponding to the topologies analyzed in this chapter.

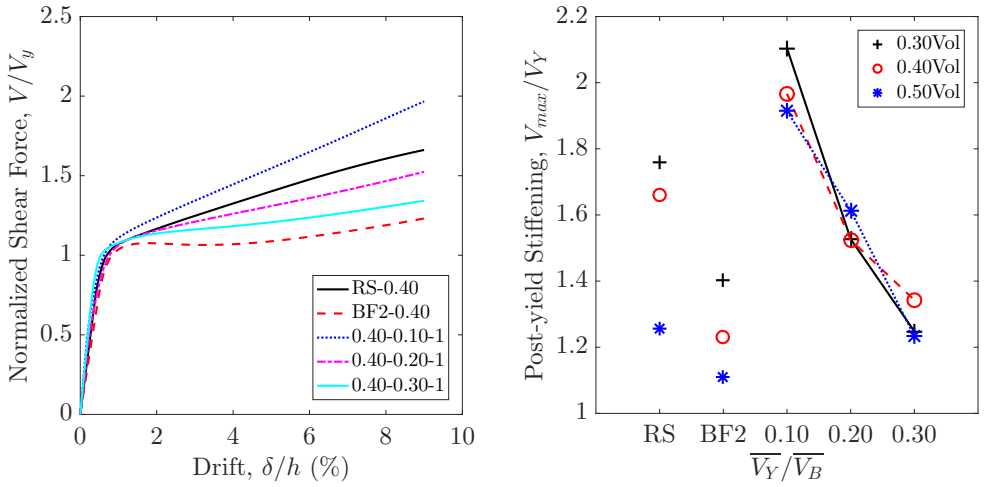

(a) Topology: ΔVol - $\overline{V_Y}/\overline{V_B}$ - Population (b) Trend of the post-yield stiffening

Figure 8.7: Normalized pushover curves and post-yield stiffening effect as a function of the volume fraction $\overline{Vol}(\mathbf{x}) = \Delta Vol$ and the objective function bias $\overline{V_Y}/\overline{V_B}$

8.4.5 Out-of-plane displacement

The out-of-plane displacement in each fuse will be tackled from three different perspectives, namely, the evolution of the out-of-plane displacement during the pushover analysis and the maximum out-of-plane displacement at the yield and final drift.

For the volume fraction equal to $\overline{Vol}(\mathbf{x}) = 0.40Vol$, the evolution of the maximum out-of-plane displacement is presented in Figure 8.8 (a). In this figure we can notice two different evolution behaviors, where the first type corresponds to an initially linear evolution of the U_3 displacement component which remains relatively linear during almost the entire displacement protocol, and a second type of evolution which has a very short linear behavior followed by a sudden increment in the U3 displacement component. In general terms, we expect a relative linear evolution of the maximum out-of-plane displacement if the objective function bias is $\overline{V_Y}/\overline{V_B} \leq 0.20$.

An additional key aspect regarding Figure 8.8 (a) is that the ratio V_Y/V_B is a good predictor for buckling resistance for the ring shaped and butterfly shaped structural fuses. Considering a volume fraction equal to $\overline{Vol}(\mathbf{x}) = 0.40Vol$ and based on the information provided in Table 8.1, the ring shaped topology has a ratio $V_Y/V_B = 0.18$ and the butterfly shaped shape a ratio equal to $V_Y/V_B = 0.26$. Hence, it is reasonable that the out-of-plane displacements in the ring shaped are so low whereas the level of buckling for the butterfly shaped is between the curves associated with an objective function bias of 0.20 and 0.30. The same behavior is observed in the evolution of the U3 displacement component corresponding to the remaining volume fractions illustrated in Appendix D.4.

Regarding the level of out-of-plane displacement at the yield drift, from Figure 8.8 (b) we can observe that all the variations of the ring shaped fuse as well as two out of the three butterfly shaped fuses have an out-of-plane displacement less than 0.1%. On the other hand, there is a trend for the optimized topologies to exhibit larger out-of-plane displacement when the value of objective function bias is increased. Nevertheless, this observation does not apply for those topologies corresponding to a volume fraction of $\overline{Vol}(\mathbf{x}) = 0.50Vol$, where the out-of-plane displacements at the yield drift are less than 0.1%.

If we continue increasing the lateral displacement, the maximum U3 displacement component present in each topology at the maximum drift angle is shown in Figure 8.8 (c). We can observe that the of out-of-plane displacement for the ring shaped and the

butterfly shaped is related to the amount of material present in each fuse, i.e. a larger volume of material makes these topologies more prone to develop larger U3 displacements. On the other hand, we observe that for the optimized topologies the maximum out-of-plane displacement seems to be a function of the objective function bias only. Moreover, when $\overline{V_Y}/\overline{V_B} = 0.10$ the optimized topologies outperforms the ring shaped and butterfly shaped topologies. Therefore, we can state that the topology optimization can generate better shapes in terms of buckling if the objective function bias is small enough.

The values of the out-of-plane displacements at the yield and final drift for all the topologies are summarized in Table 8.2.

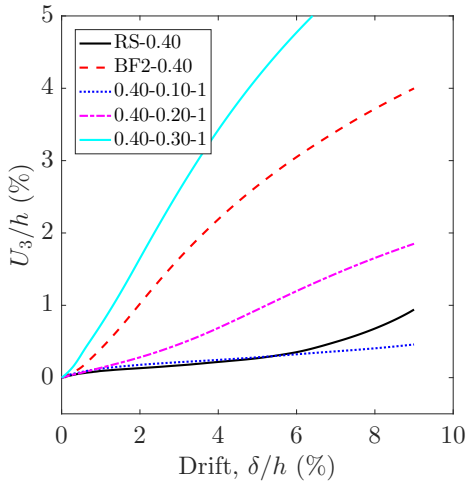

(a) Topology: ΔVol - $\overline{V_Y}/\overline{V_B}$ - Population

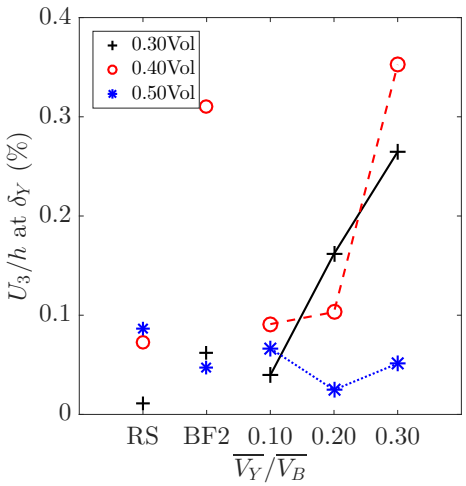

(b) Trend of the out-of-plane displacement at δ_Y

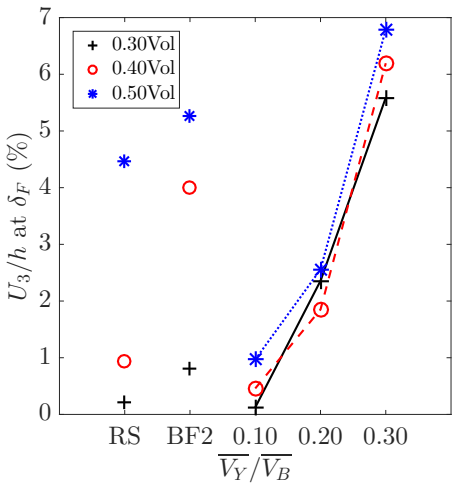

(c) Trend of the out-of-plane displacement at δ_F

Figure 8.8: Out-of-plane displacement as a function of the volume fraction $\overline{Vol}(\mathbf{x}) = \Delta Vol$ and the objective function bias $\overline{V_Y}/\overline{V_B}$

8.5 Conclusions from monotonic FE analyses

In this chapter, it was demonstrated that if the objective function bias $\overline{V_Y}/\overline{V_B}$ is small enough, the topology optimization routine creates shapes that resist buckling better than previously studies shapes.

When we reduce the value of $\overline{V_Y}/\overline{V_B}$, the volume of material that yields in the optimized topology decreases but the post-yield stiffening is greater. Additionally, the peak strength increases when we use larger values of $\overline{V_Y}/\overline{V_B}$ but the yield drift remains approximately the same for all the topologies. This means that the initial stiffness would be the same if the optimized topologies are scaled to have the same peak strength.

Finally, we can state that the objective function bias $\overline{V_Y}/\overline{V_B}$ controls the level of buckling in a topology under monotonic loading. A value of $\overline{V_Y}/\overline{V_B} = 0.10$ keeps the maximum out of plane displacement less than 1% the fuse's height at the end of the analysis. On the other hand, when $\overline{V_Y}/\overline{V_B} = 0.30$ the maximum out-of-plane displacement reaches 6% approximately. This trend of the maximum out-of-plane displacement at the end of the loading protocol as a function of V_Y/V_B is in good agreement with the results obtained from the ring shaped and butterfly shaped structural fuses.

Chapter 9

Cyclic FE Analysis of Optimized Topologies

Although the results from the monotonic analyses presented in Chapter 8 can be used to derived a preliminary conclusion about the performance of the optimized topologies, a better estimate of the actual response of the structural fuse under an earthquake event is obtained by performing cyclic analyses. Hence, the same finite element models used in Section 8.2 are modified to apply a cyclic displacement protocol. Using this analysis, output parameters are evaluated such as: total dissipated energy, strength degradation, equivalent viscous damping, and equivalent plastic strains. Analyzing this output information, a better conclusion about whether or not the optimized topologies resit buckling can be derived.

9.1 Loading protocol

The loading protocol is an adaptation of the qualifying cyclic test of link-to-column moment connections in eccentrically braced frames (AISC, 2016), where the loading sequence controls the total link rotation. In this study, only one cycle per rotation angle was used as

shown in Figure 9.1. By neglecting the deformation of the boundary elements, this sequence of total link rotations can be converted into a sequence of peak displacements. For height equal to $h = 28\ in$, the cyclic loading protocol is detailed in Table 9.1.

Table 9.1: Loading sequence for the cyclic analysis

Step	Peak Rotation (rad)	Peak Deformation, δ (in)	Number of Cycles
1	0.003 75	0.105	1
2	0.005	0.140	1
3	0.0075	0.210	1
4	0.01	0.280	1
5	0.015	0.420	1
6	0.02	0.560	1
7	0.03	0.840	1
8	0.04	1.120	1
9	0.05	1.400	1
10	0.07	1.960	1
11	0.09	2.520	1

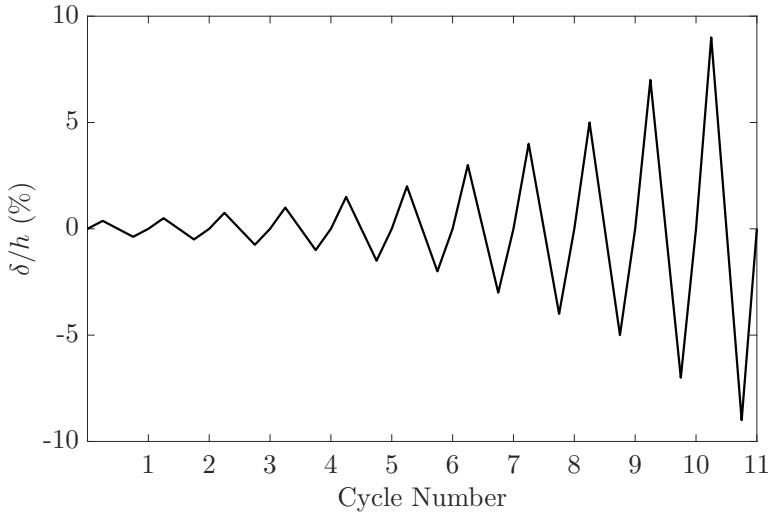

Figure 9.1: Displacement protocol for the cyclic analysis

9.2 Output parameters

The parameters used to characterize the response of the optimized topologies under cyclic loading are described in the following paragraphs.

- The hysteretic response of each topology is obtained by recording and plotting the horizontal component of the reaction force and the applied horizontal displacement at the reference node during each step of the cyclic analysis. This parameter allows us to observe the hysteretic patterns that each topology exhibit during each cycle. Finally, a backbone curve is drawn by connecting the points corresponding to the maximum level of displacement during each cycle. Therefore the backbone curve shows the evolution of the shear strength associated to the peak displacement during the cyclic analysis.

- The energy dissipation in a structural fuse is attributed to its ability of transform global lateral displacements into yielding mechanisms. The efficiency of its energy dissipation capacity is reflected in the total area under each hysteresis loop. Finally, an average

dissipated energy density is calculated by dividing the total dissipated energy by the total volume of the topology.

- The equivalent viscous damping obtained from equating the dissipated energy by the nonlinear system during a hysteresis loop and an equivalent viscous system is given by Eq. 9.1, where E_D is the area within the hysteresis loop and E_{So} is the elastic strain energy corresponding to a displacement δ_o, as illustrated in Figure 9.2.

$$\zeta_{eq} = \frac{1}{4\pi}\frac{E_D}{E_{So}} \tag{9.1}$$

  Although the damping ratio ζ_{eq} determined by the above equation is only valid when the exciting frequency is equal to the system's natural frequency, it would be a satisfactory approximation for the remaining cases (Chopra, 2017).

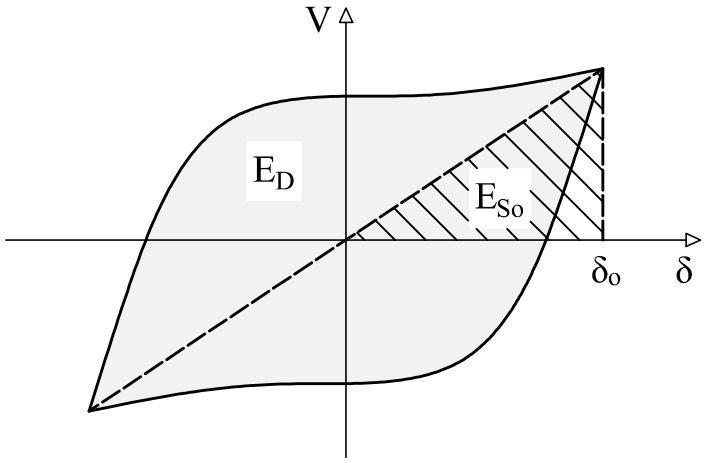

Figure 9.2: Dissipated energy E_D, and elastic strain energy E_{So}, in a hysteresis loop

- The fracture initiation in a topology can be predicted by the distribution of the equivalent plastic strain, which is a scalar value that monotonically increases whenever the material is yielding. By analyzing the values and distribution of this scalar variable at the end of the cyclic analysis, preliminary conclusions can be derived in order to reduce the probability of fracture in the topologies.

9.3 Results and discussion

9.3.1 Hysteretic behavior

The hysteretic response of the optimized topologies corresponding to a volume fraction of $\overline{Vol}(\mathbf{x}) = 0.40Vol$ are illustrated in Figure 9.3, where once again a variation of the ring shaped fuse and the butterfly shaped fuse are also shown for comparison purposes.

In terms of the shape of the hysteretic response, we can observe that the loops vary from a non degraded response to a pinched behavior. More specifically, Figure 9.3 (c) shows that when the objective function bias is equal to $\overline{V_Y}/\overline{V_B} = 0.10$ the response of the topology approaches to an ideal full hysteretic behavior without pinching nor stiffness degradation. On the other hand, the cyclic response is heavily deteriorated when the objective function bias is increased to $\overline{V_Y}/\overline{V_B} = 0.30$, since the hysteretic loops start to exhibit a pinched behavior when they reach a 3% drift, as we can observe from Figure 9.3 (e). Finally, Figure 9.3 (d) illustrates the intermediate case corresponding to the optimized topology based on $\overline{V_Y}/\overline{V_B} = 0.20$, where the hysteretic response behaves stable up to a 5% drift and then gradually deteriorates during the last two cycles.

If we compare the hysteretic behavior of the optimized topologies with the ring shaped and butterfly shaped shapes, we can observe that none of the optimized topologies exhibit a significant stiffness degradation during the analysis, in contrast to the ring shaped fuse where the stiffness at the last cycle decreased 48% if its compared to its initial value. Although the butterfly shaped fuse does not present a considerable stiffness deterioration, its pinched behaviors is evident when the drift is larger than 2%.

We should also notice that the same trends apply for the optimized topologies with a volume fraction of $\overline{Vol}(\mathbf{x}) = 0.30Vol$ and $\overline{Vol}(\mathbf{x}) = 0.50Vol$, i.e. varying the value of the objective function bias alters the cyclic response of the optimized topology, going from full hysteresis loops when $\overline{V_Y}/\overline{V_B} = 0.10$ to a pinched hysteretic behavior when $\overline{V_Y}/\overline{V_B} = 0.30$,

as it is shown in Appendix E.1.

This trend in the hysteretic behavior of the optimized topologies demonstrates that topology optimization was successful in produce structural fuses that resist buckling. Also, it shows that the objective function bias $\overline{V_Y}/\overline{V_B}$ can control not only when buckling starts but also the initial stiffness, strength degradation, and amount of dissipated energy.

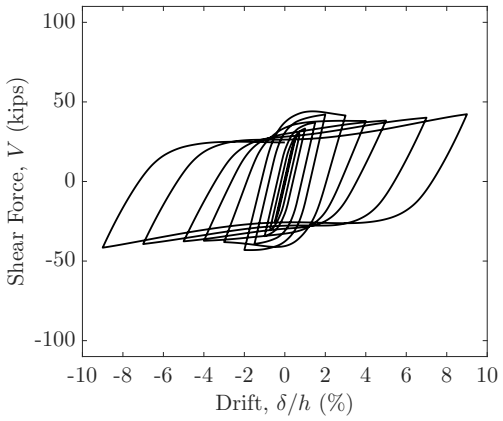

(a) Ring Shaped

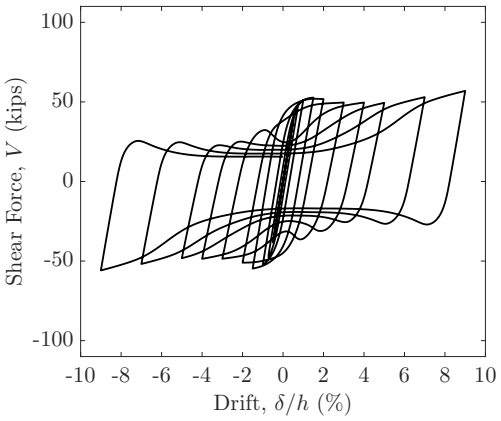

(b) Butterfly Shaped

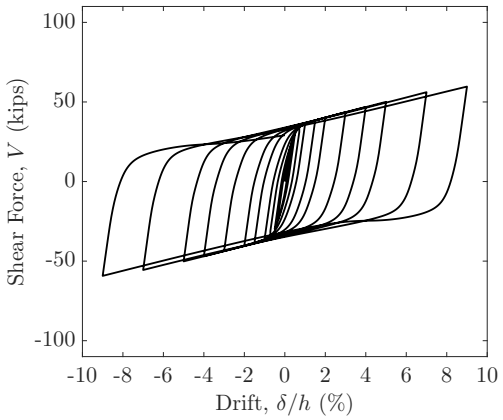

(c) 0.40-0.10-1

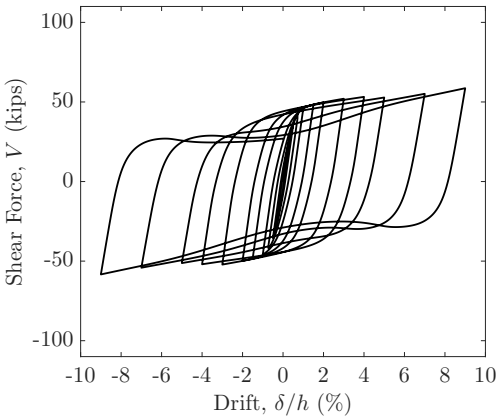

(d) 0.40-0.20-1

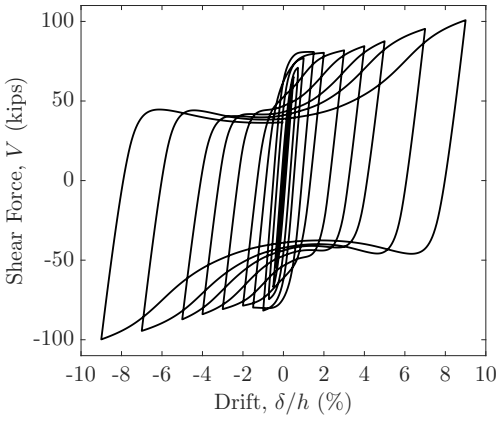

(e) 0.40-0.30-1

Figure 9.3: Hysteretic behavior of the topologies with $\overline{Vol}(\mathbf{x}) = 0.40Vol$

9.3.2 Backbone curve

The set of backbone curves corresponding to those topologies with a volume fraction equal to $\overline{Vol}(\mathbf{x}) = 0.40Vol$ are presented in Figure 9.4. It is worth mentioning that in terms of initial stiffness and strength, we can observe that the ring shaped fuse has the worst behavior among the analyzed topologies because of its relatively flexible initial stiffness and its early strength degradations after a 2% drift.

If we focus only in the backbone curves of the optimized topologies, we can observe that the initial stiffness of the optimized topology has a greater value when the value of the objective function bias $\overline{V_Y}/\overline{V_B}$ increases. However, if the intention is to reduce the strength degradation exhibited by the fuse throughout the cyclic displacement protocol, a small value of the objective function bias gives better results. This last statement is based on the negligible strength degradation presented in the backbone curves corresponding to those shapes with the two smallest objective function bias, whereas the topology $0.40 - 0.10 - 1$ presents some small deterioration in the resisting force after the 1.5% drift.

The relation between a larger initial stiffness and a larger value of the objective function bias is also valid for the remaining volume fractions, as we can observe in Appendix E.2. However, we should recall that the initial stiffness is the same when the typology's dimensions are scaled to have the same strength, as demonstrated in Chapter 8.

The major observation from these additional backbones curves is the great influence of the objective function bias in the strength deterioration during the cyclic displacement protocol. We can clearly appreciate how the strength deteriorates after the 1.5% drift for those topologies with $\overline{V_Y}/\overline{V_B} = 0.30$. On the other hand, the topologies with a smaller value of the objective function bias present a stable increment in the resisting force during the analysis.

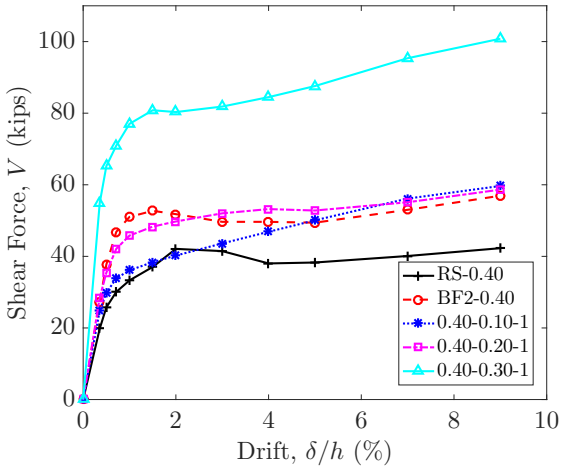

Figure 9.4: Backbone curves - Topology: ΔVol - $\overline{V_Y}/\overline{V_B}$ - Population

9.3.3 Total energy dissipation

For those topologies with a volume fraction equal to $\overline{Vol}(\mathbf{x}) = 0.40Vol$, the dissipated energy per unit volume of material during each cycle is illustrated in Figure 9.5 (a). In terms of the evolution of the dissipated energy density, we can observe that the ring shaped and butterfly shaped fuses dissipate similar amounts of energy.

Within the set of optimized topologies, we can observe that up to a 4% drift the energy dissipated in each hysteresis loop is larger in those topologies with a greater value of the objective function bias $\overline{V_Y}/\overline{V_B}$. However, during the 5% drift the energy dissipated by $0.40 - 0.20 - 1$ starts to drop and eventually becomes equal to the energy dissipated by $0.40 - 0.10 - 1$. This fact could be attributed to the loss of strength and pinched hysteretic behavior that the topology $0.40 - 0.20 - 1$ shows during the last cycles. For the topologies with different volume fraction, the trend that a greater objective function bias will produce a fuse with a greater energy dissipation capacity is still valid, as illustrated in Appendix E.3. However, there is a particular topology $0.30 - 0.30 - 2$ that is the exception to this trend. Although this shape develops the greatest resisting force, its notorious pinched behavior heavily reduces the energy dissipation capacity of the fuse after a 2% drift.

When considering the cumulative dissipated energy density as the comparison variable, we can observe from Figure 9.5 (b) that all the three optimized topologies dissipate a greater amount of energy compared to the ring shaped and butterfly shaped fuses. This observation is also valid for the other optimized topologies obtained from different volume fractions, as observed in Appendix E.3. Additionally, we can notice that there is not a significant increment in the cumulative dissipated energy density when we increase the volume fraction from $\overline{Vol}(\mathbf{x}) = 0.40Vol$ to $\overline{Vol}(\mathbf{x}) = 0.50Vol$, since its values range from $6.97 - 10.42\ kip \cdot in/in^3$ and $7.33 - 9.87\ kip \cdot in/in^3$, respectively. However there is a drop in the dissipation capacity for those topologies corresponding to $\overline{Vol}(\mathbf{x}) = 0.30Vol$ since the dissipated energy at the end of the cyclic protocol ranges from $5.15 - 7.60\ kip \cdot in/in^3$.

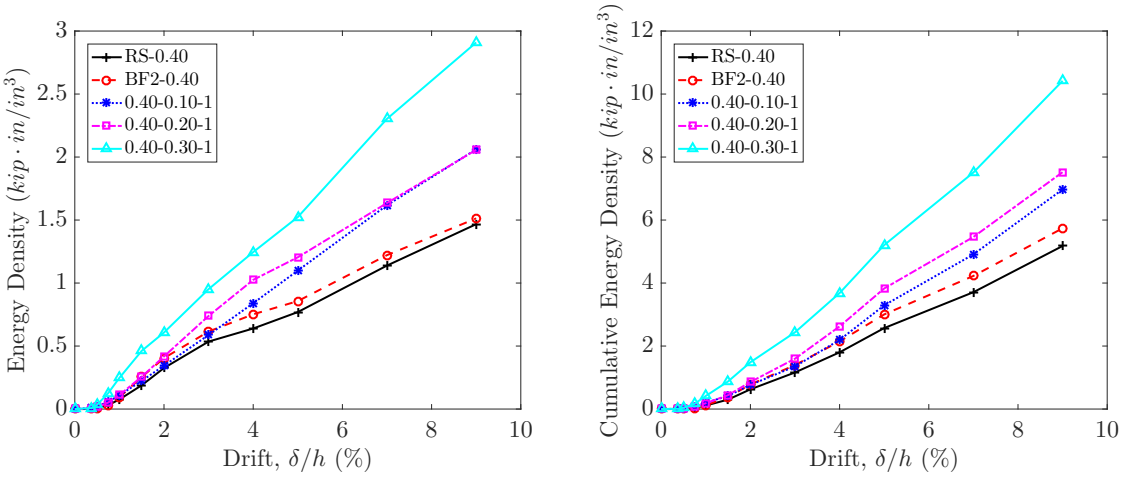

(a) Topology: ΔVol - $\overline{V_Y}/\overline{V_B}$ - Population

(b) Topology: ΔVol - $\overline{V_Y}/\overline{V_B}$ - Population

Figure 9.5: Dissipated energy per unit volume for $\overline{Vol}(\mathbf{x}) = 0.40Vol$

9.3.4 Equivalent viscous damping, ζ_{eq}

Another way to measure the energy dissipation capacity of each fuse is to calculate its equivalent viscous damping at different drift levels. Figure 9.6 shows the variation of the equivalent viscous damping ζ_{eq} at different drift levels for the topologies with a volume

fraction equal to $\overline{Vol}(\mathbf{x}) = 0.40Vol$. For all the topologies the equivalent viscous danging value grows rapidly up to a drift level equal to 2%, where for the majority of the topologies reaches its maximum value. After this point, the equivalent viscous damping for the ring shaped, $0.40 - 0.10 - 1$ and $0.40 - 0.20 - 1$; starts to decrease gradually to finally reach a average value of 0.34. On the other hand, the equivalent viscous damping for the butterfly shaped and $0.40 - 0.30 - 1$ drops drastically to an average value of 0.28 at the final drift.

A similar behavior is observed in the equivalent viscous damping evolution for the topologies associated with other volume fractions, as illustrated in Appendix E.4. When $\overline{Vol}(\mathbf{x}) = 0.30Vol$, the equivalent viscous damping reaches its maximum value at 4% drift and then gradually decreases to an average value of 0.35 for the ring shaped, $0.30-0.10-2$, and $0.30-0.20-1$ fuses but drastically decreases to an average value of 0.27 for the butterfly shaped and the $0.30-0.30-2$ topology. Lastly, the same trend is observed in those topologies with an volume fraction of $\overline{Vol}(\mathbf{x}) = 0.50Vol$, where the damping parameter reaches its maximum value at 3% drift and then gradually diminishes to an average value of 0.34 for the ring shaped, $0.50 - 0.10 - 2$ and $0.50 - 0.20 - 1$ topologies but drops drastically up to 0.30 for the butterfly shaped and the $0.50 - 0.30 - 1$ topology.

To summarize all the above described trends, practically speaking we can state that the ring shaped fuse and those optimized topologies with a objective function bias equal to $\overline{V_Y}/\overline{V_B} = (0.10, 0.20)$ behave better and virtually identical in terms of the equivalent viscous damping no matter the prescribed volume fraction. Also, the drastic decay in the damping parameter for the butterfly shaped and the optimized topologies with an objective function bias of $\overline{V_Y}/\overline{V_B} = 0.30$ could be attributed to the pinched shape of their hysteresis loops.

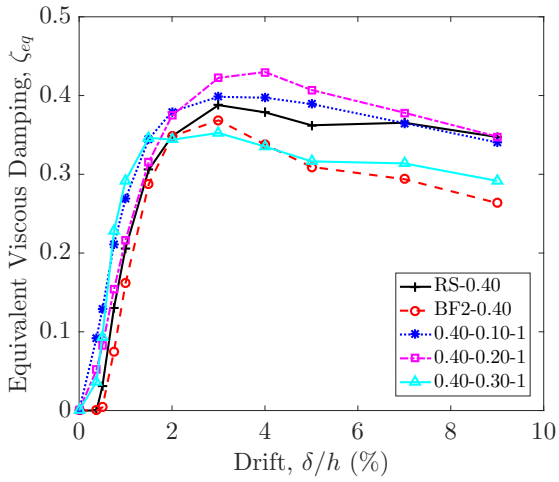

Figure 9.6: Equivalent viscous damping - Topology: ΔVol - $\overline{V_Y}/\overline{V_B}$ - Population

9.3.5 Equivalent plastic strains, PEEQ

Although the values and distribution of the equivalent plastic strains might not be necessarily accurate due to the relatively coarse mesh used in the finite element analysis, it is good indicative of the fracture prone regions. For instance, Figure 9.7 shows the contour plot of the distribution of equivalent plastic strains for those topologies with $\overline{Vol}(\mathbf{x}) = 0.40Vol$. It is clear that a smaller value of the objective function bias $\overline{V_Y}/\overline{V_B}$ leads to a larger maximum PEEQ value concentrated in a smaller region. This trend is reinforced by observing the values and distribution of the PEEQ variable in the topologies with different volume fractions illustrated in Appendix E.5.

While the concentration of equivalent plastic strains in the re-entrant corners of the fuses can be alleviated by increasing the fillet radius, those greater PEEQ values in the regions associated with the yielding mechanism need a deeper study. Although the most intuitive solution could be to increase the width of the links where the plastic hinges are located, and excessive increment could potentially trigger a change in the yielding mechanism of the topology. Hence, a more clever way to solve this problem might be parametrize some relevant geometric features of the optimized topology i.e. width of the horizontal links,

width of the vertical legs, diameters of the inner holes, fillet radius, etc. and then perform a parametric analysis using a refined mesh. The main idea would be decrease the PEEQ values while keeping the same yielding mechanism.

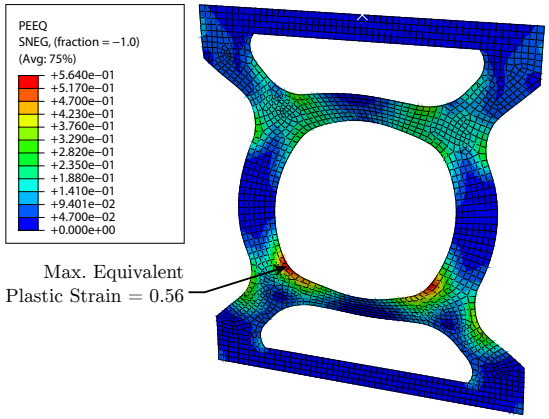

(a) Ring Shaped

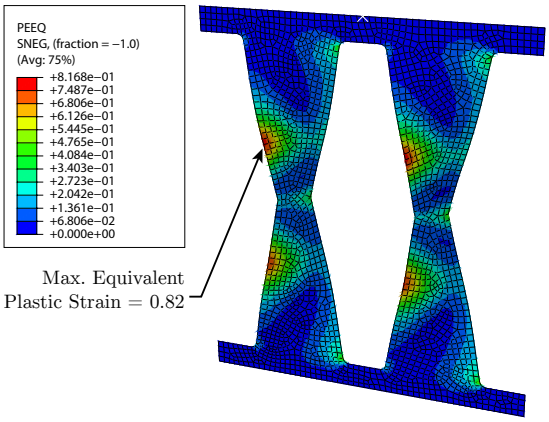

(b) Butterfly Shaped

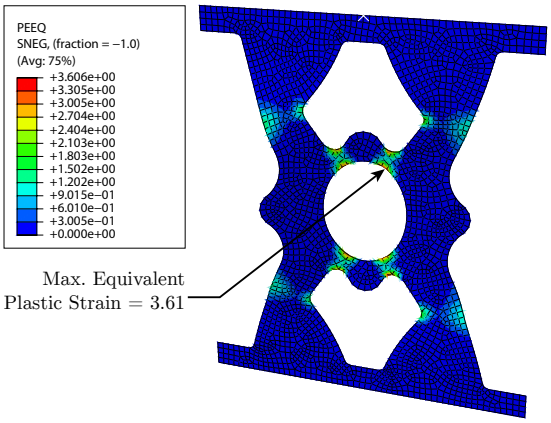

(c) 0.40-0.10-1

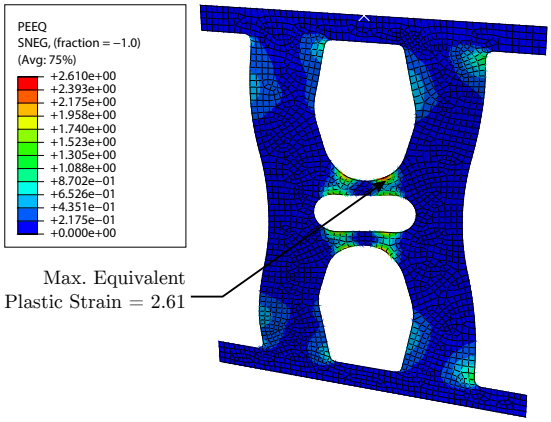

(d) 0.40-0.20-1

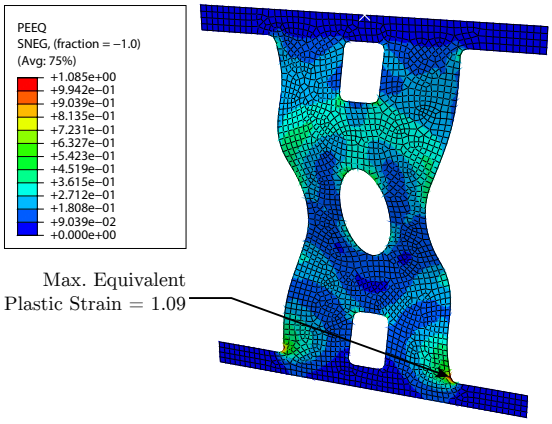

(e) 0.40-0.30-1

Figure 9.7: Final distribution of the equivalent plastic strain for $\overline{Vol}(\mathbf{x}) = 0.40Vol$

9.4 Conclusions from cyclic FE analyses

In this chapter, it was shown that the optimized topologies can resist buckling through larger cycles of inelastic deformation than the conventional shapes i.e. ring shaped and butterfly shaped structural fuses.

We can also state that the objective function bias $\overline{V_Y}/\overline{V_B}$ is a clear control on how large the inelastic deformations are before buckling. In other words, the objective function bias has a direct influence on how fast the fuse looses its ideal behavior i.e. full hysteresis loops and no strength or stiffness degradation.

Also, the optimized topologies demonstrate a better energy dissipation capacity than the conventional fuses. Moreover, the majority of the optimized shapes are at least as good as the ring shaped and butterfly shaped structural fuses in terms of equivalent viscous damping.

However, the main drawback are the larger values of equivalent plastic strains that the optimized topologies present compared to the conventional topologies. This problems needs to be examined and mitigated in future research.

Chapter 10

Conclusions

A structural shear fuse is a thin steel plate that dissipates energy by converting global displacements into local yielding mechanisms. However, its small thickness makes it prone to buckling related phenomena such as: pinched hysteretic response, strength degradation or stiffness degradation. To reduce the out-of-plane deformations when a steel shear fuse is subjected to large in-plane drift angles, this report proposes a topology optimization procedure based on evolutionary algorithms. The main goal is to find a better distribution of material that enhances the buckling resistant performance of a steel shear fuse.

The objectives of the research study were:

1. Find an appropriate objective function that quantifies how prone a shape is to buckle.
2. Implement the objective function in a genetic algorithm to optimize a square plate with constant thickness.
3. Analyze the monotonic and cyclic responses of the optimized topologies.

The following sections summarize the conclusions from the main phases that were completed to obtain a set of steel shear fuses that yield in shear load before presenting large out-of-plane displacements.

10.1 Objective function

The objective function proposed in this study relies on the concept that a fuse will resist buckling and exhibit a stable hysteretic response if its shear yield strength is sufficiently smaller than its shear buckling capacity. However, this condition has to be implemented in such a way that the fuses with negligible shear strength are not considered as the best candidates during each generation. Taking into account the above statements, Eq. 10.1 shows the objective function used to characterize how prone a topology is to buckle.

$$\begin{aligned} \underset{\mathbf{x}}{\text{minimize}}: \quad & f(\mathbf{x}) = \frac{V_Y'}{\phi\sqrt{V_Y^2 + V_B^2}} \\ \text{subject to}: \quad & \overline{Vol}(\mathbf{x}) = \Delta Vol \end{aligned} \tag{10.1}$$

Where:

$\mathbf{x}$	: Binary input vector representing the topology,
V_B	: Elastic shear buckling load,
V_Y	: Shear yield load,
$\overline{Vol}(\mathbf{x})$	: Volume of the input vector,
V_Y'	: Normalizing shear load,
ϕ	: Penalty function,
Δ	: Volume fraction,
Vol	: Volume of the full domain.

The key aspects that made this objective function well suited for a topology optimization routine using genetic algorithms are the following:

1. The objective function only depends on the shear yield load V_Y, which is obtained from a geometrically linear but material nonlinear plane-stress analysis and the shear buckling load V_B, which is calculated using a linear buckling analysis. Both are computationally efficient.

2. Although V_Y may not be an accurate yield load in presence of buckling and V_B may not be an accurate buckling load in presence of yielding, the ratio V_Y/V_B is interpreted as the propensity of a structural fuse to yield before buckling.

3. The ratio V_Y/V_B controls the amount of yielding in a structural fuse before it buckles. Although the only condition for this ratio is $V_Y/V_B < 1$, the range $0.1 \leq V_Y/V_B \leq 0.3$ is studied in this project.

4. As shown in Eq. 10.2, the penalty function ϕ is used to enforce the evolution of topologies towards shapes with a specific objective function bias $\overline{V_Y}/\overline{V_B}$. Additionally, this penalty function allows us to determine the upper limit for $\overline{V_Y}/\overline{V_B}$, i.e. the threshold value for which a topology starts to exhibit buckling related effects in its monotonic and hysteretic response.

$$\phi = \exp\left[-50(V_Y/V_B - \overline{V_Y}/\overline{V_B})^2\right] \tag{10.2}$$

5. The radial component of the objective function $\sqrt{V_Y^2 + V_B^2}$ penalize those topologies with a small shear or buckling strength. Hence, while keeping the objective function bias constant, the genetic algorithm will show preference for those topologies with larger shear strength.

6. The V_Y' term normalizes the objective function so that values are comparable regardless of units or scale.

10.2 Genetic algorithm as an optimization tool

Before running the optimization routine, a sensitivity analysis was conducted to investigate the influence of the selection, repair and mutation operators on the behavior of the genetic algorithm. Considering a square domain of 28 *in.* by 28 *in* with thickness $t = 0.50$ *in.*, a mesh of 32 by 32 elements, five independent initial populations, 40 generations, a volume

fraction of $\overline{Vol}(\mathbf{x}) = 0.40Vol$ and an objective function bias equal to $\overline{V_Y}/\overline{V_B} = 0.2$, the influence of the genetic operators on the optimization algorithm was qualitative and quantitative examined. Based on the evolution of the average objective function, convergence rate and fraction of admissible topologies we concluded that:

- The Exponential Ranking selection with $c = 0.80$ outperformed the other selection schemes, giving an averaged objective function value of $\overline{f}(\mathbf{x}) = 0.81$ and 69% of topologies being admissible at the end of the 40th generation.
- There was not sufficient evidence to conclude which mutation and repair operators are the best, so the decision of using a Mutation operator with $p = 0.05$ and $\alpha = 0.10$ together with a Repair algorithm with $\alpha = 0.90$ is based on previous studies.

Using the results from the sensitivity analysis, the topology optimization of a structural fuse with a square domain of 28 *in.* by 28 *in* and thickness $t = 0.50$ *in.* was performed. The combination of three different volume fractions $\overline{Vol}(\mathbf{x}) = (0.30Vol, 0.40Vol, 0.50Vol)$, three different objective function bias $\overline{V_Y}/\overline{V_B} = (0.10, 0.20, 0.30)$, and two independent initial populations resulted in a total of eighteen optimization runs. The main conclusions derived from these analysis are summarized in the following paragraph.

- Smaller values for the prescribed volume fraction resulted in fewer admissible topologies during the optimization algorithm. Although the repair algorithm was activated, a smaller target volume makes it more difficult to find topologies with a load path and without disconnected structural components.
- As part of its yielding mechanism, an optimized topology generally consists of solid elements connected by horizontal or vertical links. The width of these links is related to the objective function bias $\overline{V_Y}/\overline{V_B}$ used during the optimization routine. A smaller objective function bias produces a shape with weaker links, localizing the plastic deformations in small regions of material. In contrast, a larger value of $\overline{V_Y}/\overline{V_B}$ produces shapes with stronger links, spreading the plastic deformations to broader regions.

- The fact that in the majority of cases, two independent initial populations produced two different final topologies indicates that the genetic algorithm was not able to find a global optimum solution. Hence, when referring to each of the shapes obtained in this research, the term optimized topology as opposed to optimum topology should be employed.

- If we need to scale the optimized topologies, and it is desirable to keep a constant V_Y/V_B ratio, we have to apply the same scale factor to the width, height and thickness of the fuse.

10.3 Monotonic and cyclic response of the optimized topologies

Finite element models of nine optimized topologies were created using Abaqus. These optimized topologies cover all the scenarios in terms of the volume fraction $\overline{Vol}(\mathbf{x}) = \Delta Vol$, and the objective function bias $\overline{V_Y}/\overline{V_B}$.

The pushover analysis was conducted up to a lateral displacement equivalent to 9% drift. By analyzing the monotonic response of the finite elements model of each optimized topology, the following conclusions were drawn:

- Regardless of the volume fraction, a well localized yielding mechanism will be obtained if the optimization algorithm uses an objective function bias of $\overline{V_Y}/\overline{V_B} \leq 0.20$. For values of $\overline{V_Y}/\overline{V_B} > 0.20$ the inelastic deformations start to spread through the entire topology.

- Although the average yield drift is 0.64% for all the optimized topologies, a larger initial stiffness is associated with larger values of $\overline{V_Y}/\overline{V_B}$. Nevertheless, the optimized topologies would have the same stiffness if they are scaled to have the same strength.

- The highest post-yield stiffening corresponds to those topologies optimized with an objective function bias equal to $\overline{V_Y}/\overline{V_B} = 0.10$.

- Under monotonic loading, those topologies with an objective function bias $V_Y/V_B = 0.10$ do not exhibit strength degradation. Moreover, the maximum out-of-plane displacement at the end of the analysis is less than 1% the fuse's height. Although the topologies with an objective function bias $V_Y/V_B = 0.20$ do not present strength degradation either, the maximum out-of-plane displacement is larger than 1% the fuse's height when the drift is greater than 5%. On the other hand, those fuses that were optimized with $V_Y/V_B = 0.30$ show strength degradation after 2.5% drift. Also, the maximum out-of-plane displacement increases rapidly and in most cases becomes larger than 1% the fuse's height after reaching 2% drift.

- We conclude that under monotonic loading, the topology optimization is effective in resisting buckling up to 9% and 5% drift, if it uses an objective function bias equal to $\overline{V_Y}/\overline{V_B} = 0.10$ and $\overline{V_Y}/\overline{V_B} = 0.20$, respectively.

To have a better representation of the actual response of each topology under an seismic event, each finite element model was subjected to a cyclic displacement protocol illustrated in Figure 9.1. The conclusions derived from this analysis are listed as follows:

- An optimized structural fuse subjected to cyclic loading will have a full hysteretic response with negligible strength or stiffness degradation up to 9% and 5% drift, if it was optimized using an objective function bias equal to $\overline{V_Y}/\overline{V_B} = 0.10$ and $\overline{V_Y}/\overline{V_B} = 0.20$, respectively.

- Although all the optimized topologies have a larger energy dissipation capacity than the ring shaped and butterfly shaped structural fuses, the largest dissipated energy density corresponds to an objective function bias of $\overline{V_Y}/\overline{V_B} = 0.30$.

- In terms of equivalent viscous damping, those optimized topologies with an objective function bias equal to $\overline{V_Y}/\overline{V_B} = (0.10, 0.20)$ behave as good as the ring shaped fuse.

- The largest values of equivalent plastic strain are present in those fuses optimized with an objective function bias of $\overline{V_Y}/\overline{V_B} = 0.10$. Hence, we can conclude that smaller values of $\overline{V_Y}/\overline{V_B}$ increase the probability of premature fracture in the optimized topology.

10.4 Recommendations for further research

Although the original objective of this project was successfully accomplished, the additional research needs that emerged throughout this study are summarized as follows:

- Perform a mesh sensitivity analysis to find the adequate mesh resolution after which refining the mesh does not produce major changes in the final optimized topology. However, this analysis should also take into account that changes in the final distribution of material could be attributed to the stochastic nature of genetic algorithms. Hence, besides looking for changes in the final geometry, a more general criterion for the sensitivity analysis could be based on the variation of the first buckling mode or the variation in the yielding mechanism of the optimized structural fuse.

- Optimize a structural fuse with an aspect ratio $h/w \neq 1$, where h and w are the height and width of the domain, respectively. This analysis would be useful to investigate how the yielding mechanism varies as a function of the aspect ratio.

- Using parallel computing for the optimization routine becomes somehow imperative since increasing the number of elements for the input vector implies larger initial populations, more generations and more time to perform the finite element analysis.

- Although the most straightforward solution to reduce the effective plastic strains would be increase the width of the links where the plastic hinges form, a more detailed study should be conducted. One possible solution could be perform the optimization algorithm considering an objective function bias in the range $0.20 < \overline{V_Y}/\overline{V_B} < 0.30$.

Also, to reduce the effective plastic strains we could do a parametric analysis of the main geometric features of those optimized topologies with $\overline{V_Y}/\overline{V_B} = 0.20$.

References

AISC (2016). "Seismic provision for structural steel buildings." *ANSI/AISC 341-16*.

ASCE (2010). "Minimum design loads for buildings and other structures." *ASCE/SEI 7-10*.

Baker, J. E. (1987). "Reducing bias and inefficiency in the selection algorithm." In "Proceedings of the second international conference on genetic algorithms," vol. 206. pp. 14–21.

Berman, J. and Bruneau, M. (2003). "Plastic analysis and design of steel plate shear walls." *Journal of Structural Engineering*, 129(11), 1448–1456.

Blickle, T. and Thiele, L. (1995). "A comparison of selection schemes used in genetic algorithms."

Chapman, C. D., Saitou, K. and Jakiela, M. J. (1994). "Genetic algorithms as an approach to configuration and topology design." *Journal of mechanical design*, 116(4), 1005–1012.

Chopra, A. K. (2017). "Dynamics of structures: theory and applications to earthquake engineering." *Earthquake Engineering*.

Clifton, C., Bruneau, M., MacRae, G., Leon, R., Fussell, A. et al. (2011). "Steel building damage from the christchurch earthquake series of 2010/2011." *SESOC Journal*, 24(2), 27.

De Matteis, G., Brando, G. and Mazzolani, F. M. (2012). "Pure aluminium: An innovative material for structural applications in seismic engineering." *Construction and Building Materials*, 26(1), 677–686.

De Matteis, G., DAgostino, F. and Brando, G. (2014). "Experimental tests on steel buckling inhibited shear panels." *Open Construction and Building Technology Journal*, 8(1), 279–288.

Deng, K., Pan, P., Li, W. and Xue, Y. (2015). "Development of a buckling restrained shear panel damper." *Journal of Constructional Steel Research*, 106(1), 311 – 321.

Deng, K., Pan, P., Sun, J., Liu, J. and Xue, Y. (2014). "Shape optimization design of steel shear panel dampers." *Journal of Constructional Steel Research*, 99, 187–193.

Driver, R. G., Kulak, G. L., Kennedy, D. L. and Elwi, A. E. (1998). "Cyclic test of four-story steel plate shear wall." *Journal of Structural Engineering*, 124(2), 112–120.

Eatherton, M. R., Ma, X., Krawinkler, H., Mar, D., Billington, S., Hajjar, J. F. and Deierlein, G. G. (2014). "Design concepts for controlled rocking of self-centering steel-braced frames." *Journal of Structural Engineering*, 140(11), 04014082.

Egorova, N., Eatherton, M. R. and Maurya, A. (2014). "Experimental study of ring-shaped steel plate shear walls." *Journal of Constructional Steel Research*, 103, 179–189.

Fortney, P. J., Shahrooz, B. M. and Rassati, G. A. (2007). "Large-scale testing of a replaceable fuse steel coupling beam." *Journal of structural engineering*, 133(12), 1801–1807.

Ghabraie, K., Chan, R., Huang, X. and Xie, Y. M. (2010). "Shape optimization of metallic yielding devices for passive mitigation of seismic energy." *Engineering Structures*, 32(8), 2258–2267.

He, H., Wang, X. and Zhang, X. (2016). "Energy-dissipation performance of combined low yield point steel plate damper based on topology optimization and its application in structural control." *Advances in Materials Science and Engineering*, 2016.

Jakiela, M. J., Chapman, C., Duda, J., Adewuya, A. and Saitou, K. (2000). "Continuum structural topology design with genetic algorithms." *Computer Methods in Applied Mechanics and Engineering*, 186(2-4), 339–356.

Kelly, J. M., Skinner, R. and Heine, A. (1972). "Mechanisms of energy absorption in special devices for use in earthquake resistant structures." *Bulletin of NZ Society for Earthquake Engineering*, 5(3), 63 – 88.

Liu, Y. and Shimoda, M. (2013). "Shape optimization of shear panel damper for improving the deformation ability under cyclic loading." *Structural and Multidisciplinary Optimization*, 48(2), 427–435.

Ma, X., Borchers, E., Pena, A., Krawinkler, H. and Deierlein, G. (2010). "Design and behavior of steel shear plates with openings as energy-dissipating fuses." *John A. Blume Earthquake Engineering Center Technical Report,(173)*.

Madeira, J. A., Rodrigues, H. and Pina, H. (2005). "Multi-objective optimization of structures topology by genetic algorithms." *Advances in Engineering Software*, 36(1), 21–28.

Madeira, J. A., Rodrigues, H. and Pina, H. (2006). "Multiobjective topology optimization of structures using genetic algorithms with chromosome repairing." *Structural and Multidisciplinary Optimization*, 32(1), 31–39.

McKenna, F., Fenves, G., Scott, M. et al. (2000). "Open system for earthquake engineering simulation." *University of California, Berkeley, CA*.

Pezeshk, S. and Camp, C. V. (2002). "State of the art on the use of genetic algorithms in design of steel structures." *Recent advances in optimal structural design*, 55–80.

Popov, E. P. and Engelhardt, M. D. (1988). "Seismic eccentrically braced frames." *Journal of Constructional Steel Research*, 10, 321–354.

Sigmund, O. (2001). "A 99 line topology optimization code written in matlab." *Structural and multidisciplinary optimization*, 21(2), 120–127.

Sigmund, O. (2011). "On the usefulness of non-gradient approaches in topology optimization." *Structural and Multidisciplinary Optimization*, 43(5), 589–596.

Simulia (2014). "Abaqus version 6.14 documentation." *Dassault Systems*.

Taylor, R. L. (2013). "Feap version 8.4 user manual." *University of California at Berkeley*.

Wang, S., Tai, K. and Wang, M. Y. (2006). "An enhanced genetic algorithm for structural topology optimization." *International Journal for Numerical Methods in Engineering*, 65(1), 18–44.

Xu, Y. H., Li, A. Q., Zhou, X. D. and Sun, P. (2011). "Shape optimization study of mild steel slit dampers." In "Advanced Materials Research," vol. 168. Trans Tech Publ, pp. 2434–2438.

Appendix A

Eigen buckling analysis using OpenSees

This appendix explains the reasons why OpesSees was not used to calculate the elastic buckling load of a structural fuse. First, we present the variables involved in the eigen-value problem, then we describe how to get these variables from the OpenSees finite element models, and finally we explain why this process may not be suited to calculate the elastic buckling load.

As we recall from Section 3.2, the elastic buckling load can be found by solving the eigen-value problem $([K_M] + \lambda_{crit}[K_G])\{\delta U\} = \{0\}$, where $[K_M]$ is the material stiffness matrix, $[K_G]$ is the geometric stiffness matrix, λ_{crit} is the lowest positive eigen-value, and $\{\delta U\}$ is the corresponding eigen-vector.

Considering the geometry and boundary conditions illustrated in Figure 4.5, a general description of the OpenSees finite element model is presented in the following paragraph.

1. The domain is discretized using square shell MITC4 elements with thickness equal to $t = 0.50\ in.$ Also, the "fiber" section approach is used to perform the through-thickness numerical integration. Finally, the material is modeled as elastic isotropic

with a Young's modulus of $E = 29000\ ksi$, and Poisson's ratio equal to $\nu = 0.3$.

2. We use a geometric transformation command to perform a coordinate transformation from the basic system to the global coordinate system.

3. The reference load $\{F\}_{ref}$, is evenly distributed among all the nodes corresponding to the top edge of the fuse.

4. After defining the geometry, boundary conditions and analysis options, we include the `PrintA` command to get the current tangent stiffness matrix. Finally, we run the input file using OpenSees.

Given the fact that OpenSees only computes the current tangent stiffness matrix $[K_T]$, the eigen-value problem has to be solved in three steps:

1. Run the OpenSees finite element model and get the material stiffness matrix $[K_M]$, by considering a linear elastic material with a linear transformation of coordinates. Under the previous assumptions, the current tangent stiffness matrix $[K_T]_{lin}$ provided by OpenSess would be equal to the material stiffness matrix $[K_M]$.

2. Run the OpenSees finite element model and get the tangent stiffness matrix $[K_T]_{cor}$, by considering a linear elastic material with a corotational transformation of coordinates. In this case, the tangent stiffness matrix can be expressed as $[K_T]_{cor} = [K_M] + [K_G]_{cor}$.

3. Use MATLAB to calculate the geometric stiffness matrix $[K_G]_{cor} = [K_T]_{cor} - [K_T]_{lin}$ and solve the eigen-value problem to get the elastic buckling load $\{F\}_{crit} = \lambda_{crit}\{F\}_{ref}$.

However, the elastic buckling load calculated with the above described procedure was unrealistic, and not even close to those values obtained from the Abaqus and FEAP finite element models. Hence, we can conclude that the unsatisfactory results provided by OpenSees may be due that the corotational transformation does not work properly with shell MITC4 elements.

Appendix B

Summary of the Results of Topology Optimization

This appendix provides information regarding necessary input information for the genetic algorithm such as initial population and objective function equation. Additionally, the output generated by each optimization routine i.e. the optimized topologies are also illustrated.

B.1 Initial population

The following figures illustrate a subset of five initial topologies corresponding to a volume fraction equal to $\overline{Vol}(\mathbf{x}) = 0.30Vol$ and $\overline{Vol}(\mathbf{x}) = 0.50Vol$. These shapes are used to enrich the initial population during the optimization algorithms.

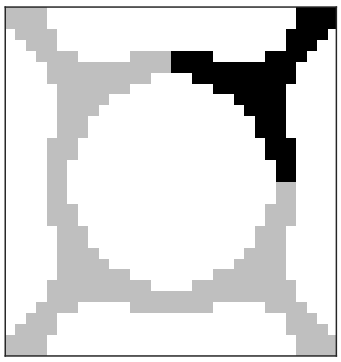

(a) Ring-shaped fuse (Egorova et al., 2014)

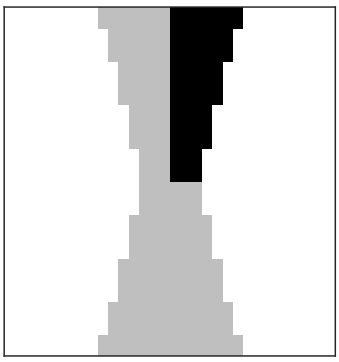

(b) Butterfly fuses (Ma et al., 2010)

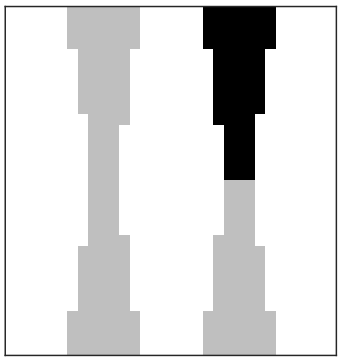

(c) Butterfly fuses (Ma et al., 2010)

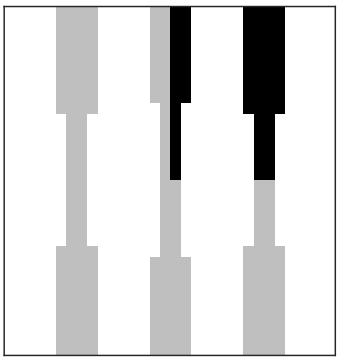

(d) Butterfly fuses (Ma et al., 2010)

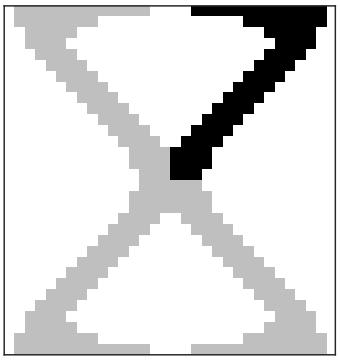

(e) Compliance minimization problem (Sigmund, 2001)

Figure B.1: Subset of initial topologies for $\overline{Vol}(\mathbf{x}) = 0.30Vol$

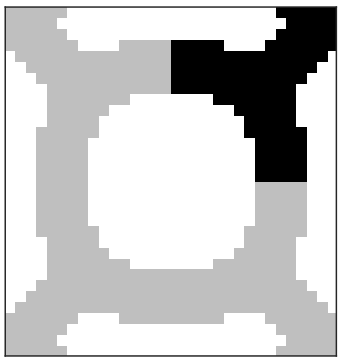

(a) Ring-shaped fuse (Egorova et al., 2014)

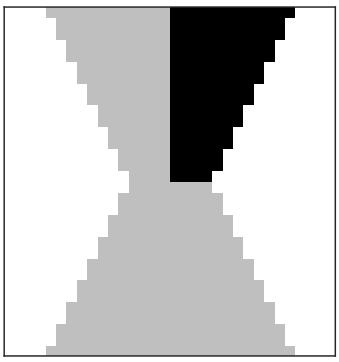

(b) Butterfly fuses (Ma et al., 2010)

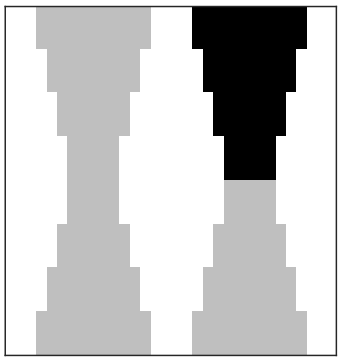

(c) Butterfly fuses (Ma et al., 2010)

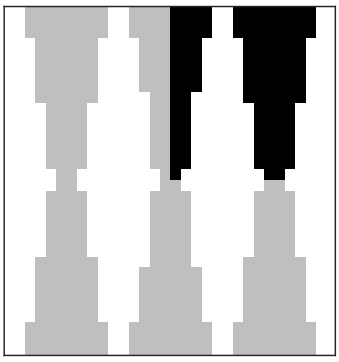

(d) Butterfly fuses (Ma et al., 2010)

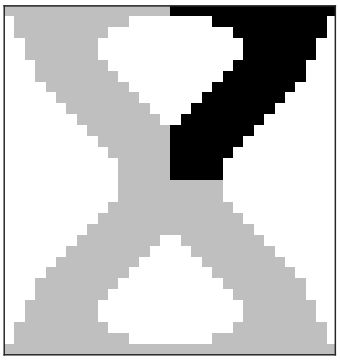

(e) Compliance minimization problem (Sigmund, 2001)

Figure B.2: Subset of initial topologies for $\overline{Vol}(\mathbf{x}) = 0.50Vol$

B.2 Objective functions

The following table summarizes all the objective functions used during each optimization routine. These objective functions are the results of varying the volume fraction $\overline{Vol}(\mathbf{x}) = \Delta Vol$, and the objective function bias $\overline{V_Y}/\overline{V_B}$.

Table B.1: Objective functions $f(\mathbf{x})$ for $\overline{Vol}(\mathbf{x}) = 0.30Vol$

$\overline{V_Y}/\overline{V_B}$	$f(\mathbf{x})$
0.1	$\dfrac{210}{\sqrt{3}\exp\left[-50(V_Y/V_B - 0.1)^2\right]\sqrt{V_Y^2 + V_B^2}}$
0.2	$\dfrac{210}{\sqrt{3}\exp\left[-50(V_Y/V_B - 0.2)^2\right]\sqrt{V_Y^2 + V_B^2}}$
0.3	$\dfrac{210}{\sqrt{3}\exp\left[-50(V_Y/V_B - 0.3)^2\right]\sqrt{V_Y^2 + V_B^2}}$

Table B.2: Objective functions $f(\mathbf{x})$ for $\overline{Vol}(\mathbf{x}) = 0.40Vol$

$\overline{V_Y}/\overline{V_B}$	$f(\mathbf{x})$
0.1	$\dfrac{280}{\sqrt{3}\exp\left[-50(V_Y/V_B - 0.1)^2\right]\sqrt{V_Y^2 + V_B^2}}$
0.2	$\dfrac{280}{\sqrt{3}\exp\left[-50(V_Y/V_B - 0.2)^2\right]\sqrt{V_Y^2 + V_B^2}}$
0.3	$\dfrac{280}{\sqrt{3}\exp\left[-50(V_Y/V_B - 0.3)^2\right]\sqrt{V_Y^2 + V_B^2}}$

Table B.3: Objective functions $f(\mathbf{x})$ for $\overline{Vol}(\mathbf{x}) = 0.50Vol$

$\overline{V_Y}/\overline{V_B}$	$f(\mathbf{x})$
0.1	$\dfrac{350}{\sqrt{3}\exp\left[-50(V_Y/V_B - 0.1)^2\right]\sqrt{V_Y^2 + V_B^2}}$
0.2	$\dfrac{350}{\sqrt{3}\exp\left[-50(V_Y/V_B - 0.2)^2\right]\sqrt{V_Y^2 + V_B^2}}$
0.3	$\dfrac{350}{\sqrt{3}\exp\left[-50(V_Y/V_B - 0.3)^2\right]\sqrt{V_Y^2 + V_B^2}}$

B.3 Genetic algorithm results

In this section the result from each optimization routine consists in a set of four figures where the first one shows the evolution of the objective function corresponding to the best topology during each iteration. The second figure illustrates the fraction of admissible topologies as a fraction of the initial population and how it evolves during the optimization process. Finally, the last two figures are the optimized topologies at the end of the $400th$ generation corresponding for each of the two initial populations.

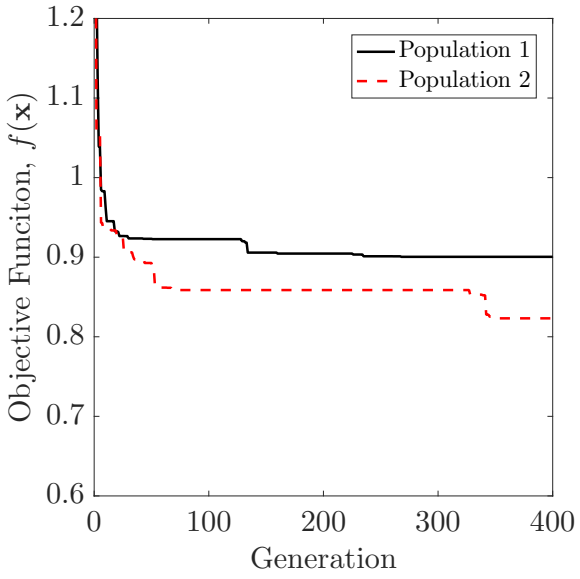

(a) Evolution of the objective function

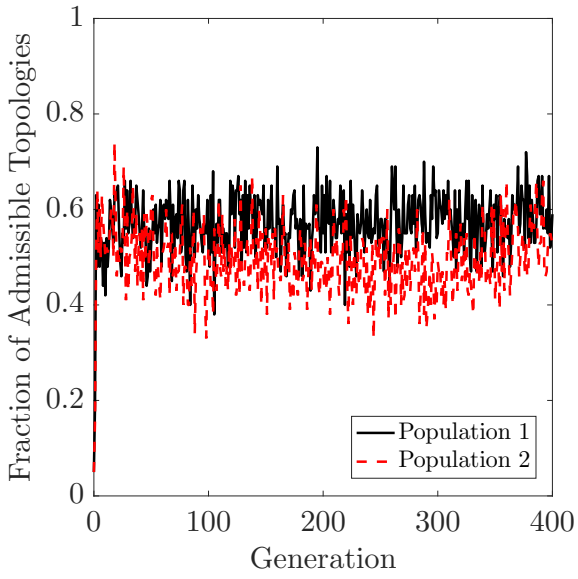

(b) Fraction of admissible topologies

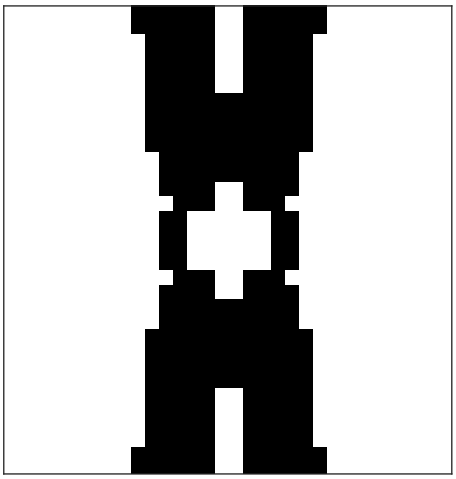

(c) Final optimized topology - Population 1

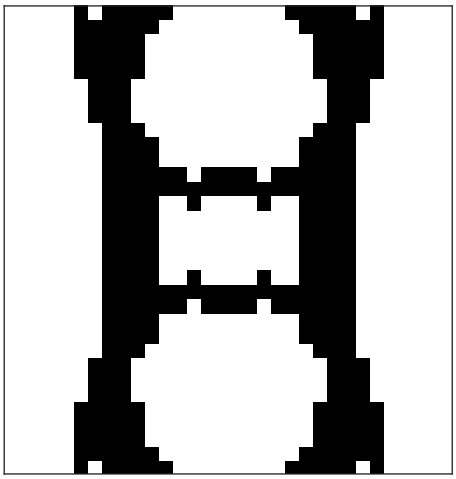

(d) Final optimized topology - Population 2

Figure B.3: Genetic algorithm results for $\overline{Vol}(\mathbf{x}) = 0.30Vol$ and $\overline{V_Y}/\overline{V_B} = 0.10$

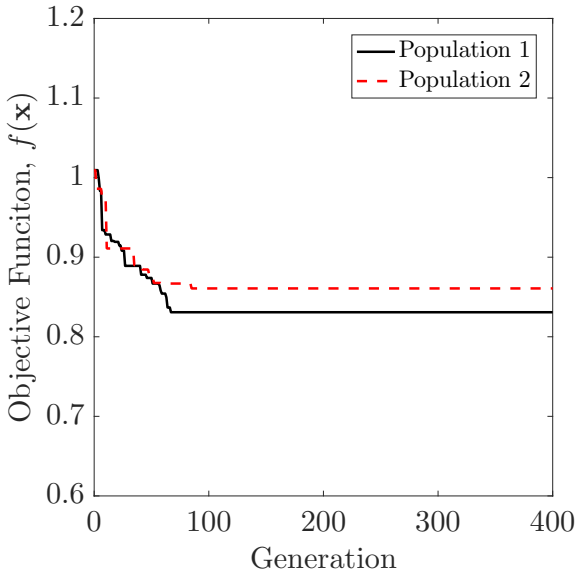

(a) Evolution of the objective function

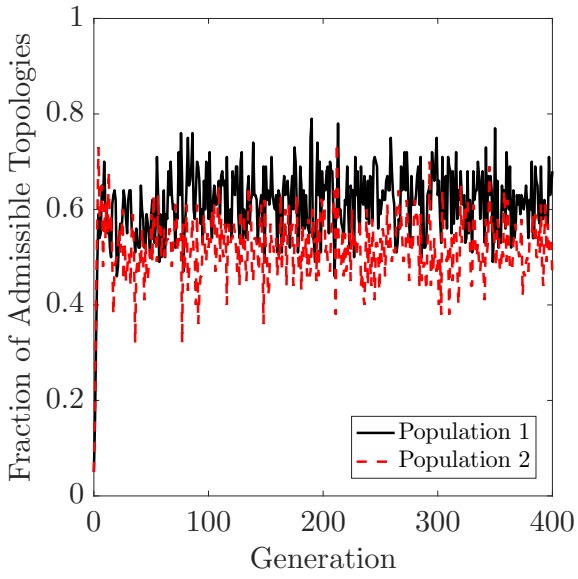

(b) Fraction of admissible topologies

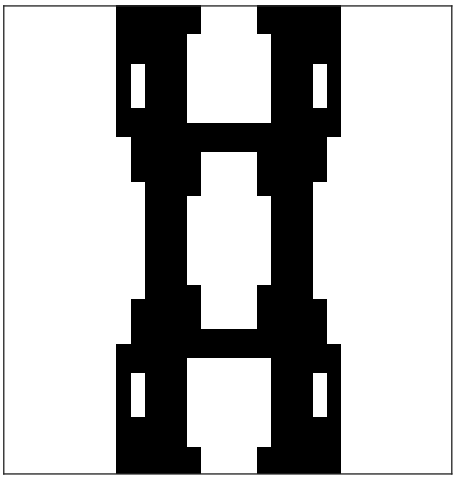

(c) Final optimized topology - Population 1

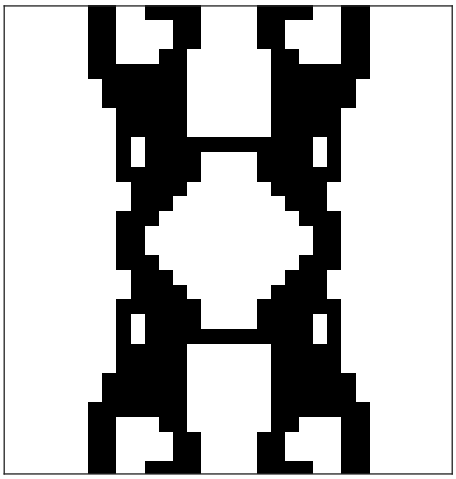

(d) Final optimized topology - Population 2

Figure B.4: Genetic algorithm results for $\overline{Vol}(\mathbf{x}) = 0.30Vol$ and $\overline{V_Y}/\overline{V_B} = 0.20$

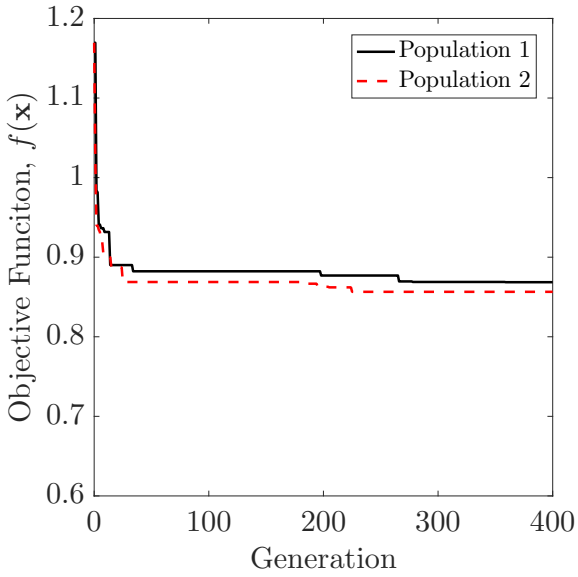

(a) Evolution of the objective function

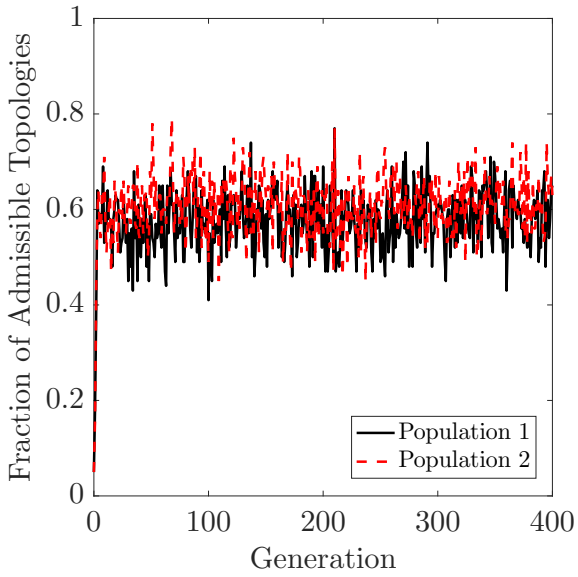

(b) Fraction of admissible topologies

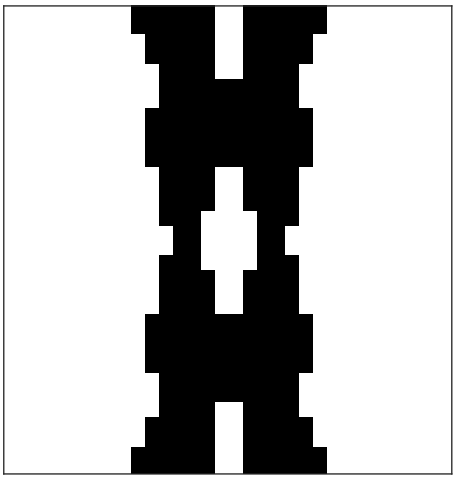

(c) Final optimized topology - Population 1

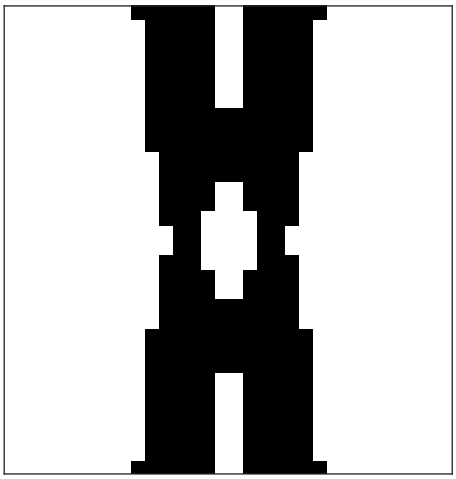

(d) Final optimized topology - Population 2

Figure B.5: Genetic algorithm results for $\overline{Vol}(\mathbf{x}) = 0.30Vol$ and $\overline{V_Y}/\overline{V_B} = 0.30$

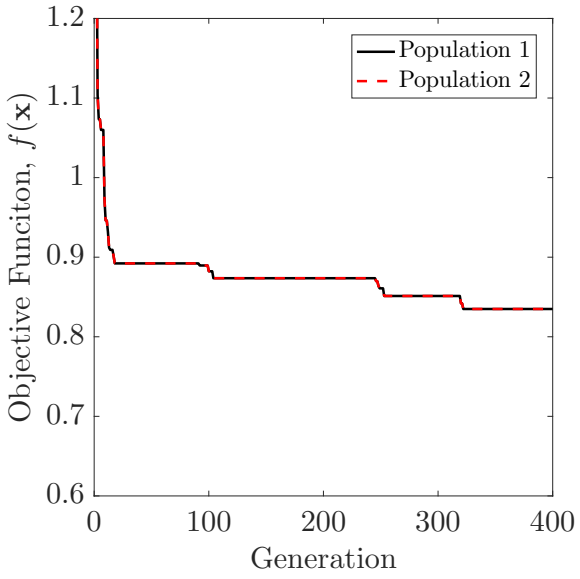

(a) Evolution of the objective function

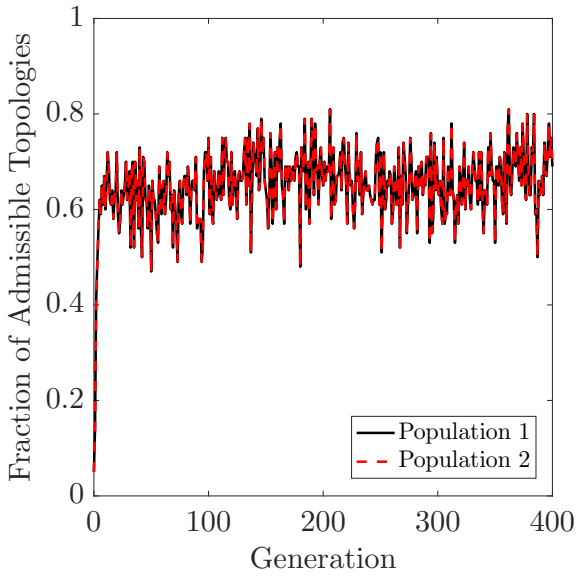

(b) Fraction of admissible topologies

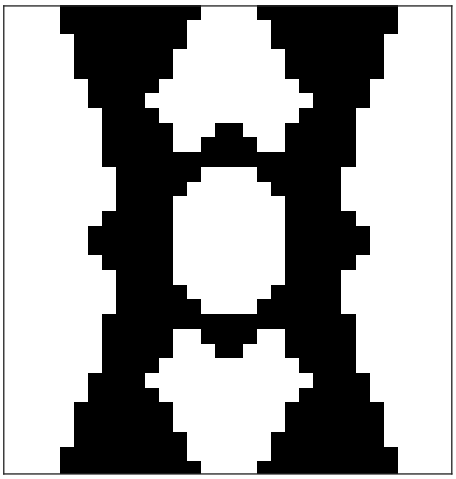

(c) Final optimized topology - Population 1

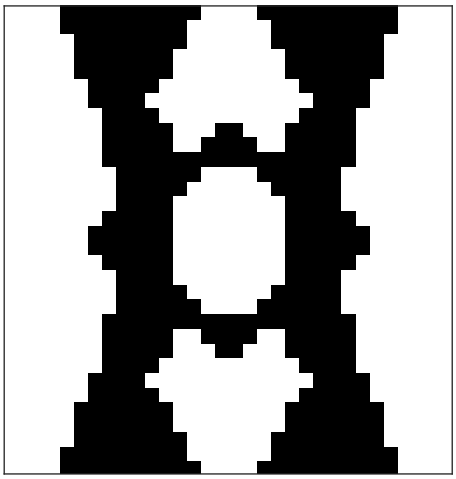

(d) Final optimized topology - Population 2

Figure B.6: Genetic algorithm results for $\overline{Vol}(\mathbf{x}) = 0.40Vol$ and $\overline{V_Y}/\overline{V_B} = 0.10$

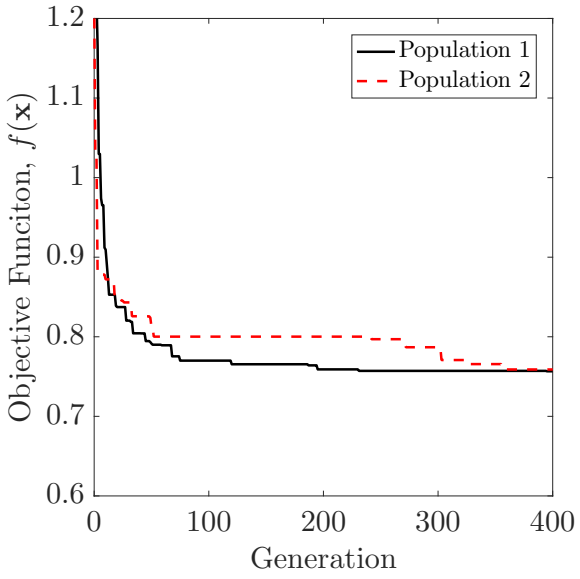

(a) Evolution of the objective function

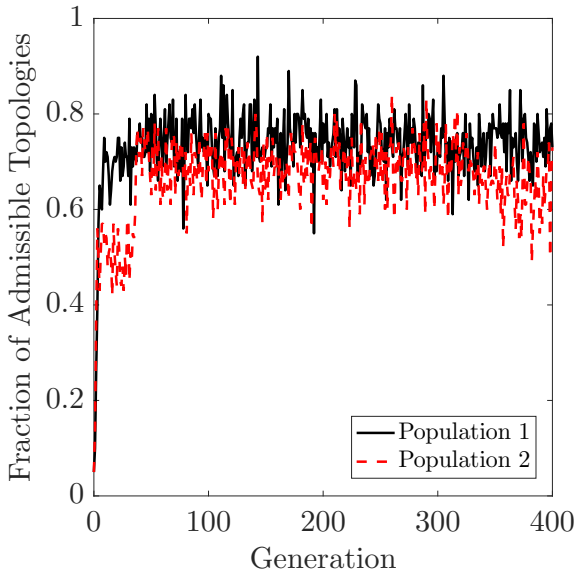

(b) Fraction of admissible topologies

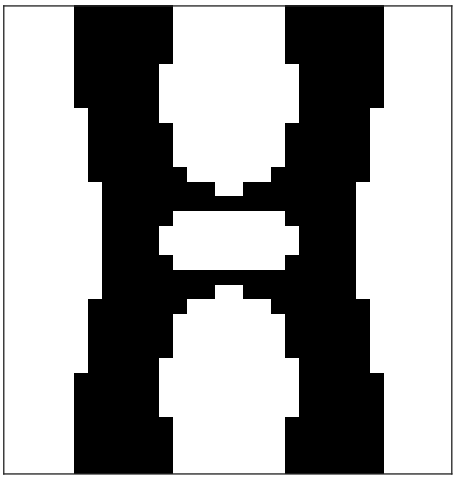

(c) Final optimized topology - Population 1

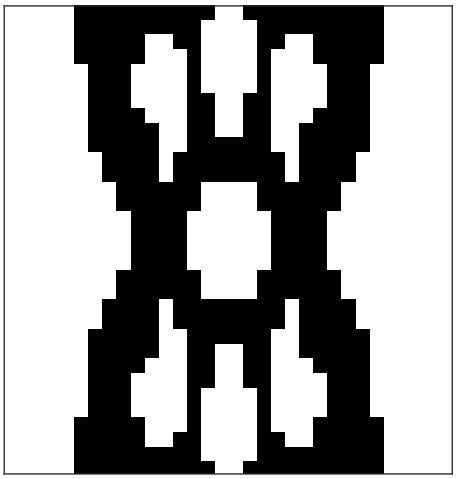

(d) Final optimized topology - Population 2

Figure B.7: Genetic algorithm results for $\overline{Vol}(\mathbf{x}) = 0.40Vol$ and $\overline{V_Y}/\overline{V_B} = 0.20$

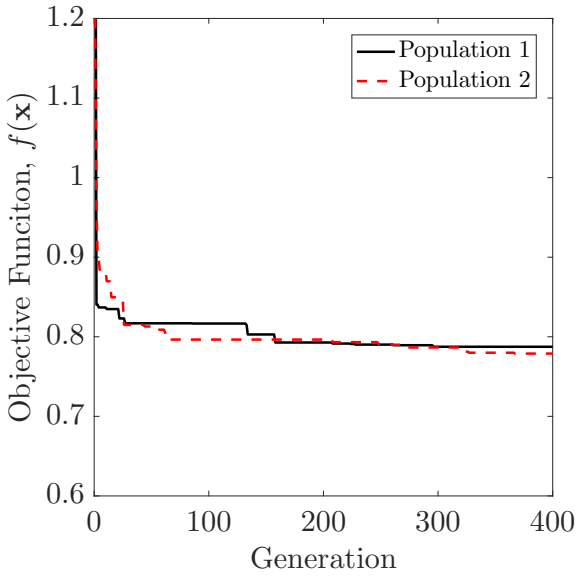

(a) Evolution of the objective function

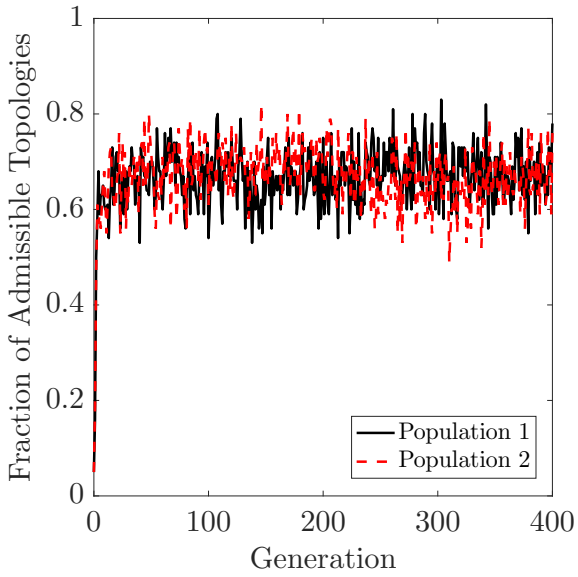

(b) Fraction of admissible topologies

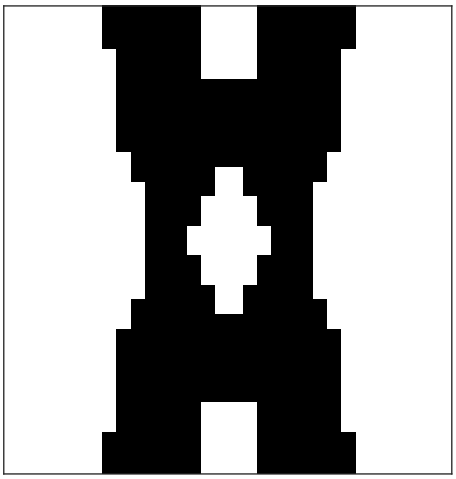

(c) Final optimized topology - Population 1

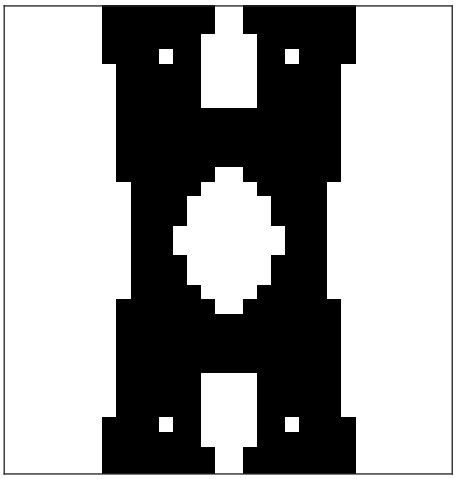

(d) Final optimized topology - Population 2

Figure B.8: Genetic algorithm results for $\overline{Vol}(\mathbf{x}) = 0.40Vol$ and $\overline{V_Y}/\overline{V_B} = 0.30$

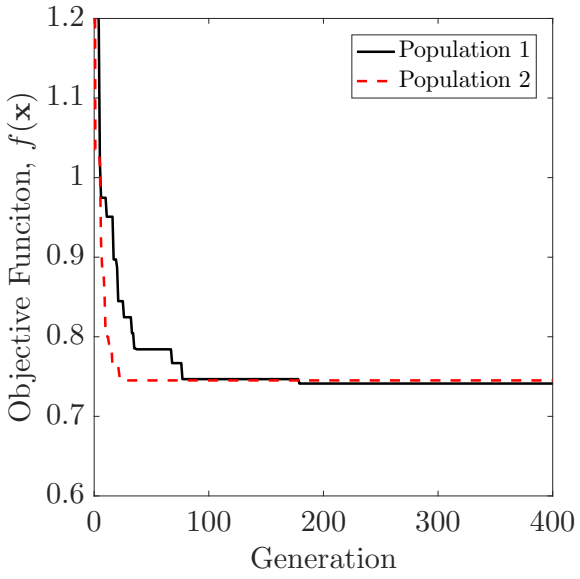

(a) Evolution of the objective function

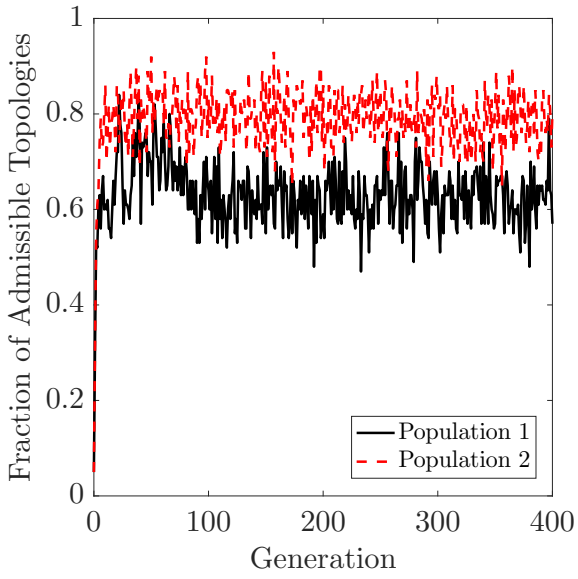

(b) Fraction of admissible topologies

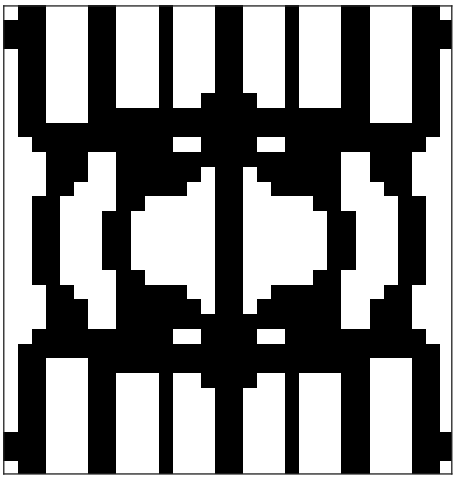

(c) Final optimized topology - Population 1

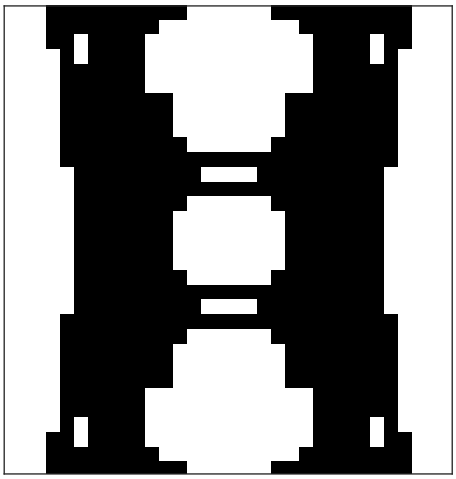

(d) Final optimized topology - Population 2

Figure B.9: Genetic algorithm results for $\overline{Vol}(\mathbf{x}) = 0.50Vol$ and $\overline{V_Y}/\overline{V_B} = 0.10$

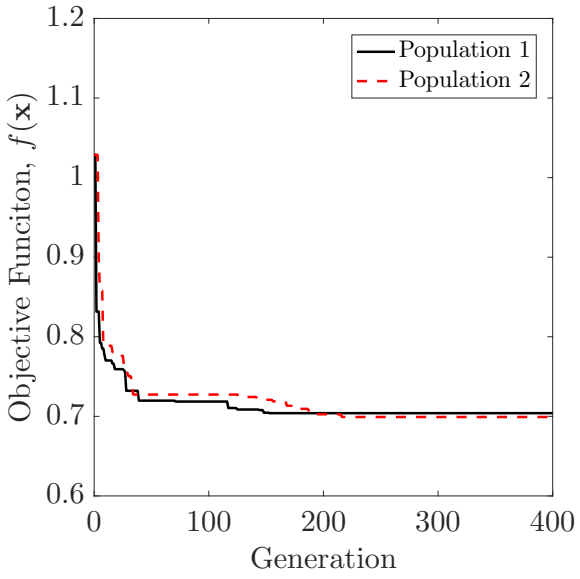

(a) Evolution of the objective function

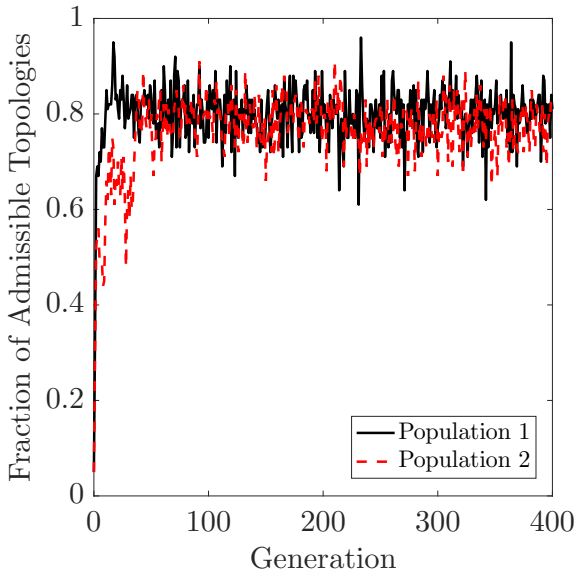

(b) Fraction of admissible topologies

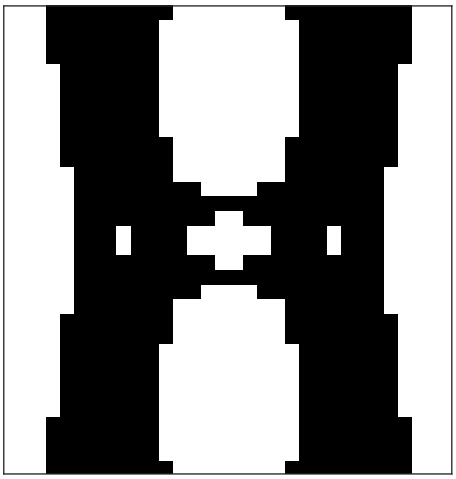

(c) Final optimized topology - Population 1

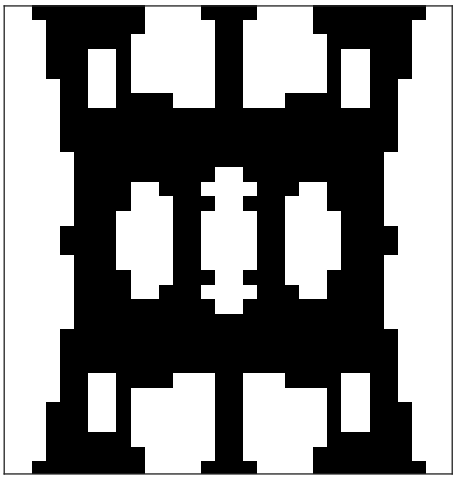

(d) Final optimized topology - Population 2

Figure B.10: Genetic algorithm results for $\overline{Vol}(\mathbf{x}) = 0.50Vol$ and $\overline{V_Y}/\overline{V_B} = 0.20$

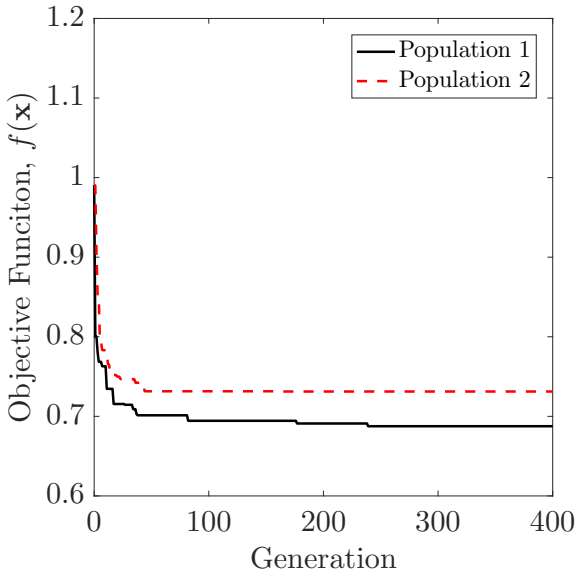

(a) Evolution of the objective function

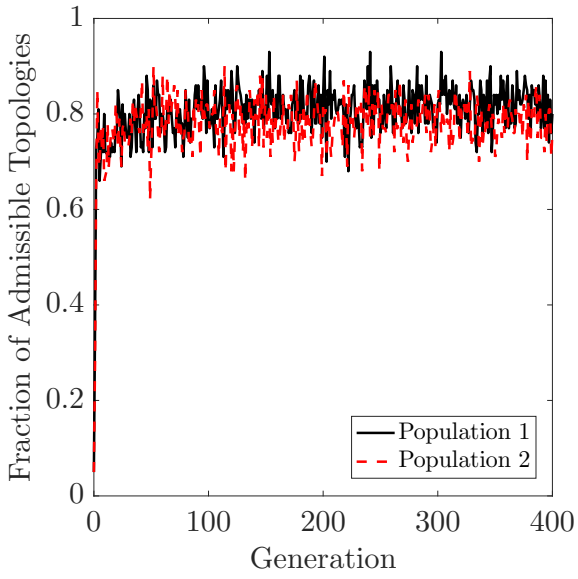

(b) Fraction of admissible topologies

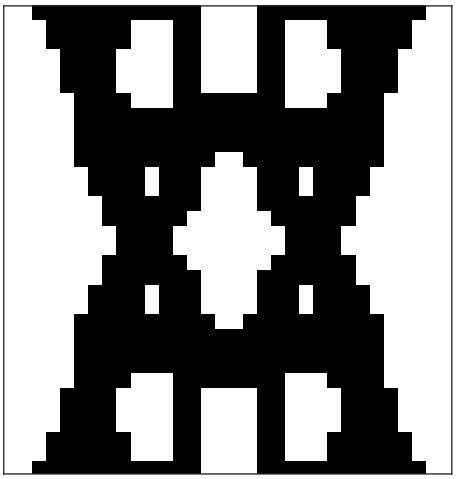

(c) Final optimized topology - Population 1

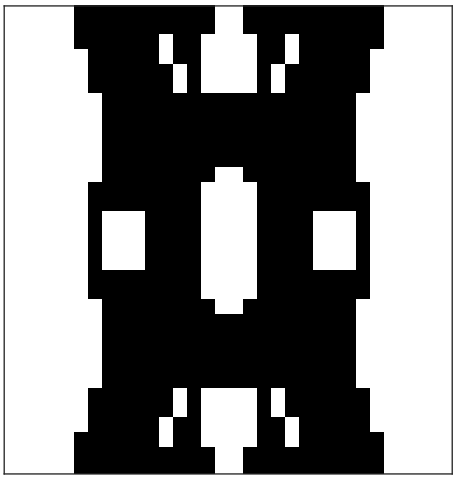

(d) Final optimized topology - Population 2

Figure B.11: Genetic algorithm results for $\overline{Vol}(\mathbf{x}) = 0.50Vol$ and $\overline{V_Y}/\overline{V_B} = 0.30$

B.4 Shear yield force and shear buckling load for each optimized topology

The following table summarizes the shear yield load V_Y, shear buckling load V_B, and its corresponding objective function $f(\mathbf{x})$ value for all the optimized topologies.

Table B.4: Numerical results from the optimization process using genetic algorithms

$\overline{Vol}(\mathbf{x})$	$\overline{V_Y}/\overline{V_B}$	Population	V_B (kips)	V_Y (kips)	$f(\mathbf{x})$
$0.30Vol$	0.10	1	134.57	12.32	0.90
		2	146.55	14.85	0.82
	0.20	1	143.24	28.22	0.83
		2	139.25	26.32	0.86
	0.30	1	133.66	40.30	0.87
		2	135.64	40.54	0.86
$0.40Vol$	0.10	1	194.64	22.46	0.83
		2	194.64	22.46	0.83
	0.20	1	209.67	41.42	0.76
		2	209.05	41.28	0.76
	0.30	1	196.64	60.08	0.79
		2	198.88	59.43	0.78
$0.50Vol$	0.10	1	271.27	27.10	0.74
		2	274.89	33.09	0.75
	0.20	1	282.72	54.36	0.70
		2	283.36	56.95	0.70
	0.30	1	281.41	84.85	0.69
		2	265.97	83.24	0.73

Appendix C

Geometric Interpretation of Topologies

In this appendix the smoothed interpretation of nine optimized topologies is drawn using a grid as background to avoid the graphical saturation due to excessive drawing annotations. This figures can be used to replicate or modify the geometry of each optimized topology used in this study.

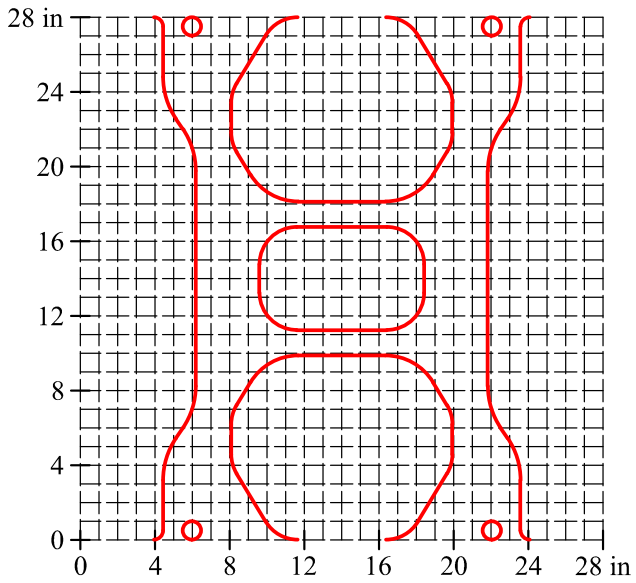

Figure C.1: Optimized topology for the case 0.30-0.10-2

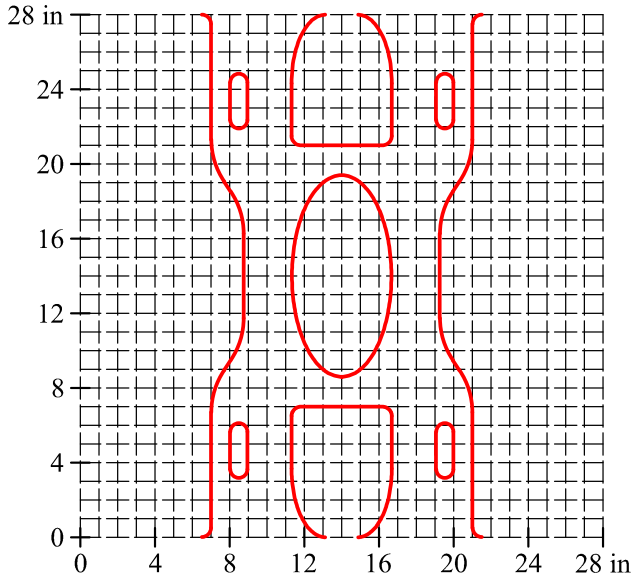

Figure C.2: Optimized topology for the case 0.30-0.20-1

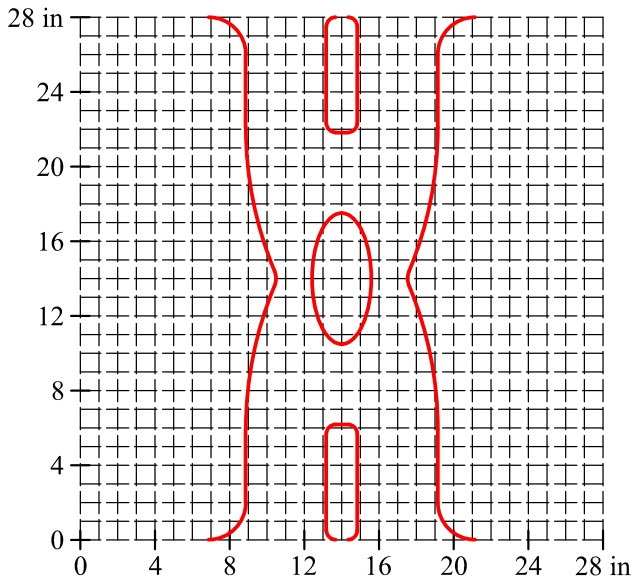

Figure C.3: Optimized topology for the case 0.30-0.30-2

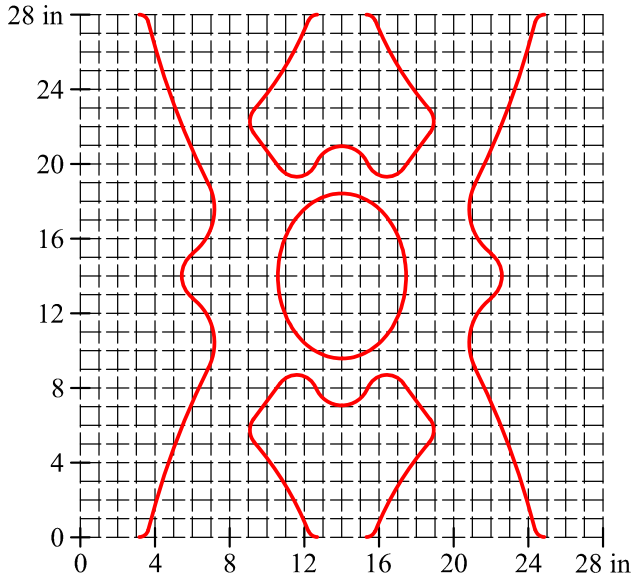

Figure C.4: Optimized topology for the case 0.40-0.10-1

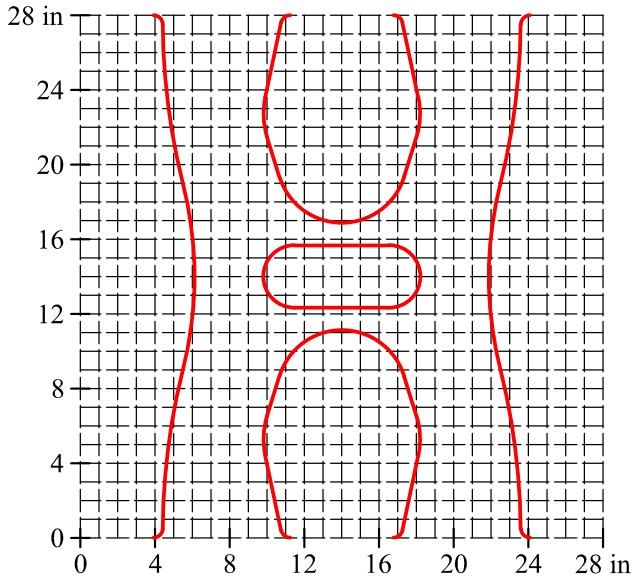

Figure C.5: Optimized topology for the case 0.40-0.20-1

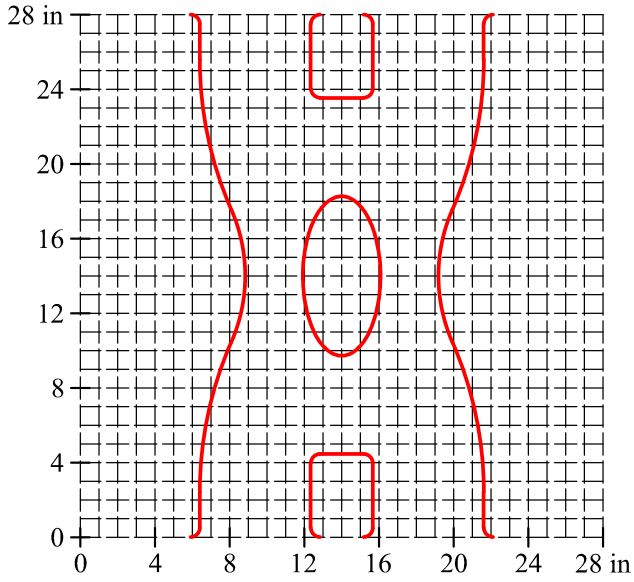

Figure C.6: Optimized topology for the case 0.40-0.30-1

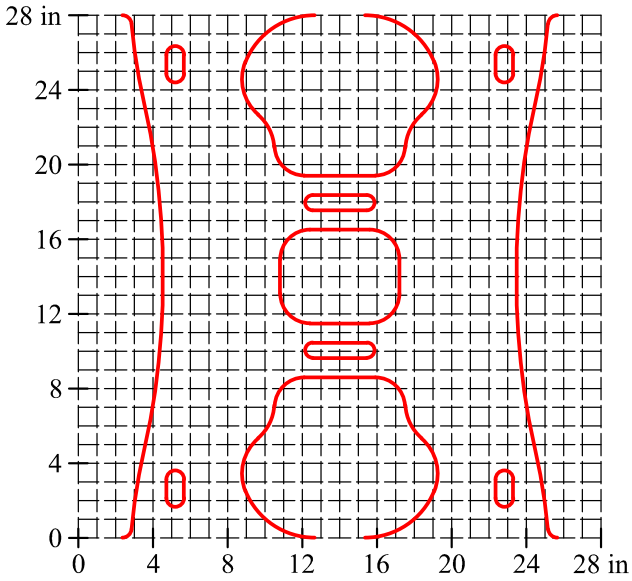

Figure C.7: Optimized topology for the case 0.50-0.10-2

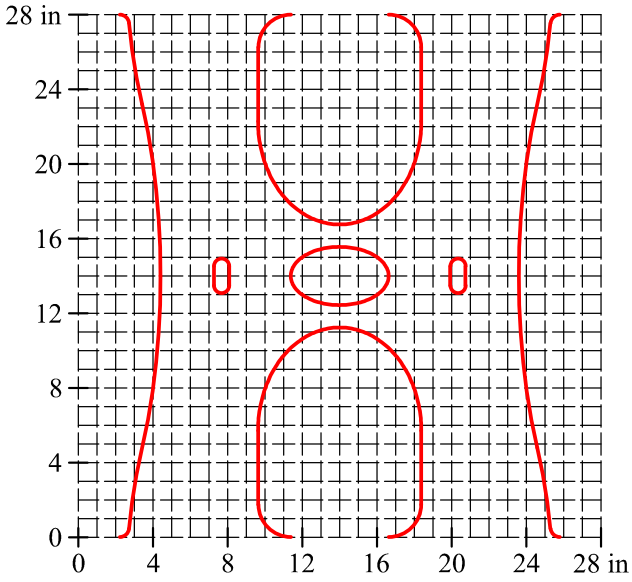

Figure C.8: Optimized topology for the case 0.50-0.20-1

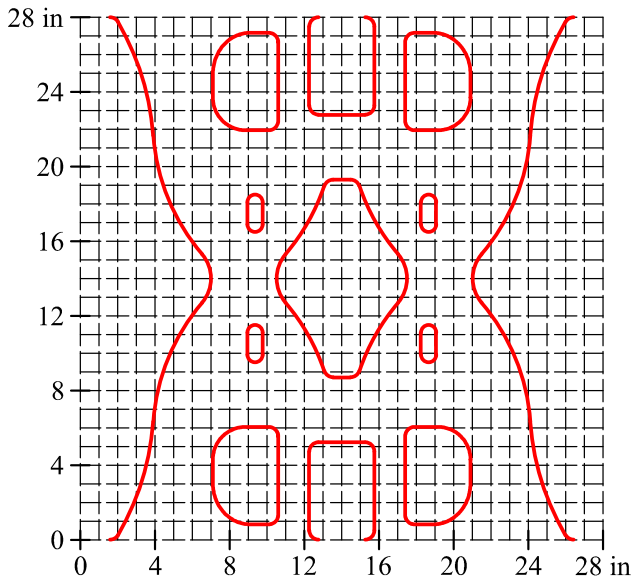

Figure C.9: Optimized topology for the case 0.50-0.30-1

Appendix D

Pushover Analysis

All the output data generated throughout monotonic pushover analysis is presented in this appendix. The buckling modes obtained from a linear buckling analysis, the yielding mechanism, the pushover curve and the evolution of the out-of-plane displacement for a set of nine optimized topologies are summarized.

D.1 Buckling shapes

The first two buckling modes and its corresponding critical buckling load obtained from a linear buckling analysis is presented for a subset of optimized topologies. The contour plot which has a maximum and minimum value of 1 and -1 respectively, represents the out-of-plane displacements associated with the buckling shape.

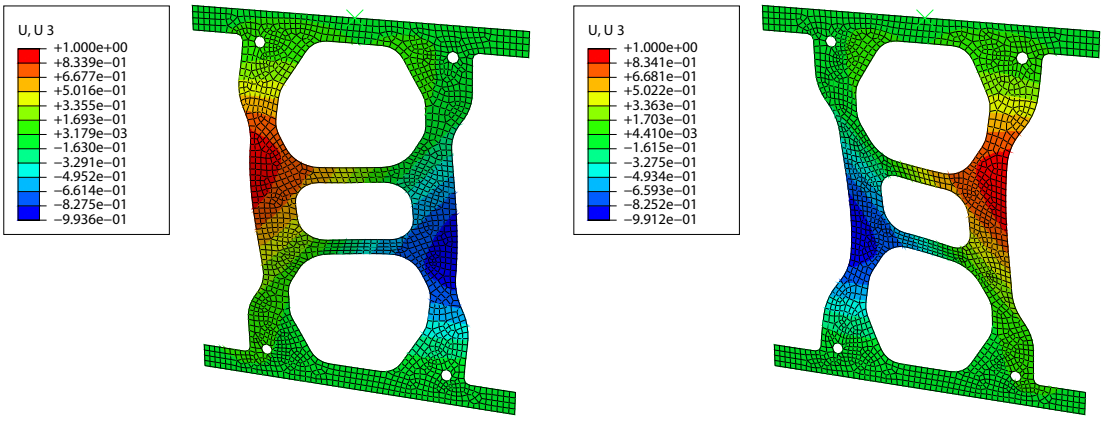

(a) Buckling Shape 1 - $V_B = 128\,kips$ (b) Buckling Shape 2 - $V_B = -128\,kips$

Figure D.1: Buckling shapes for Topology 0.30-0.10-2

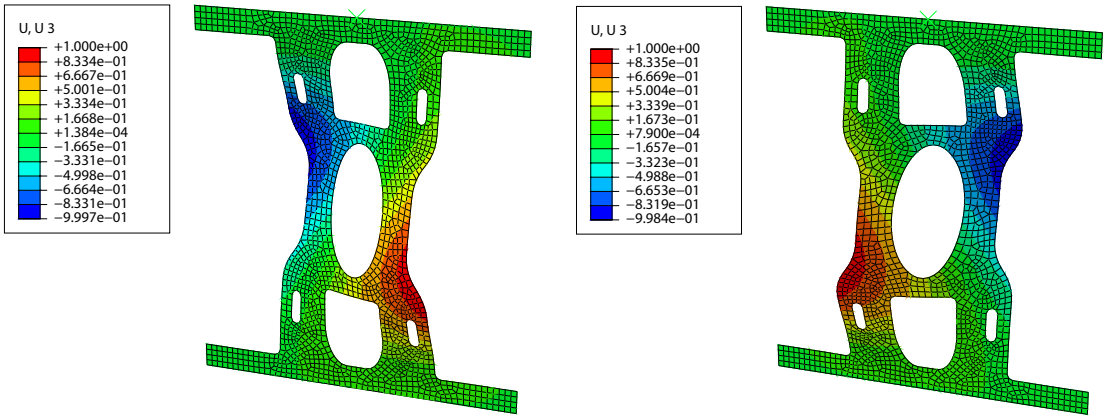

(a) Buckling Shape 1 - $V_B = 125\,kips$ (b) Buckling Shape 2 - $V_B = -125\,kips$

Figure D.2: Buckling shapes for Topology 0.30-0.20-2

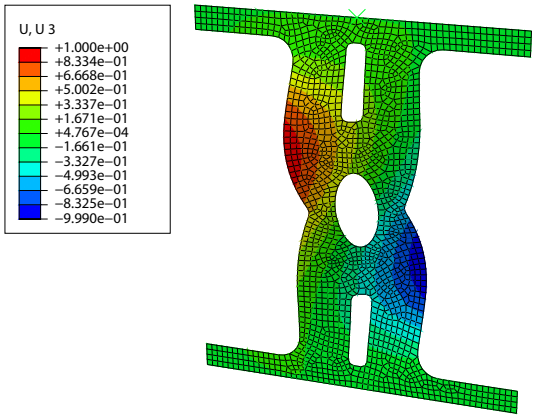

(a) Buckling Shape 1 - $V_B = 120\,kips$

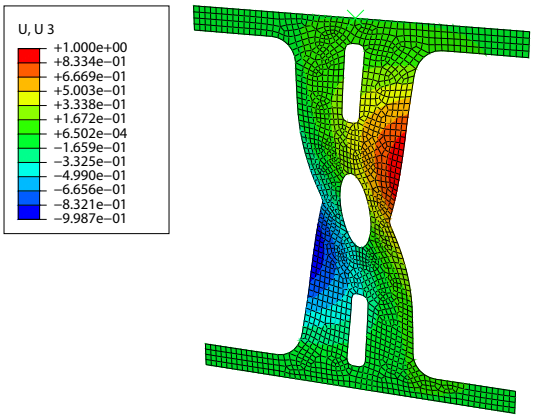

(b) Buckling Shape 2 - $V_B = -120\,kips$

Figure D.3: Buckling shapes for Topology 0.30-0.30-2

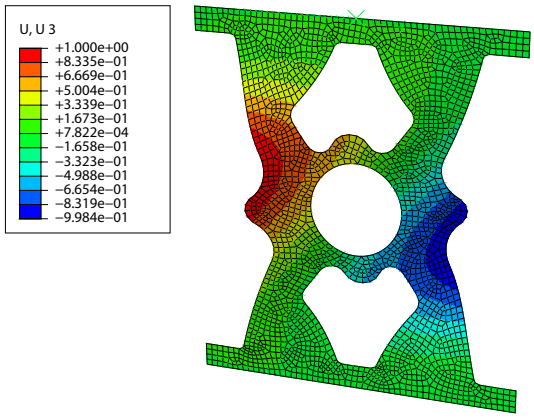

(a) Buckling Shape 1 - $V_B = 172\,kips$

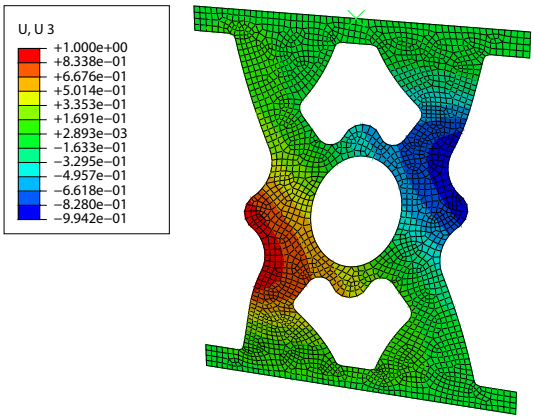

(b) Buckling Shape 2 - $V_B = -172\,kips$

Figure D.4: Buckling shapes for Topology 0.40-0.10-1

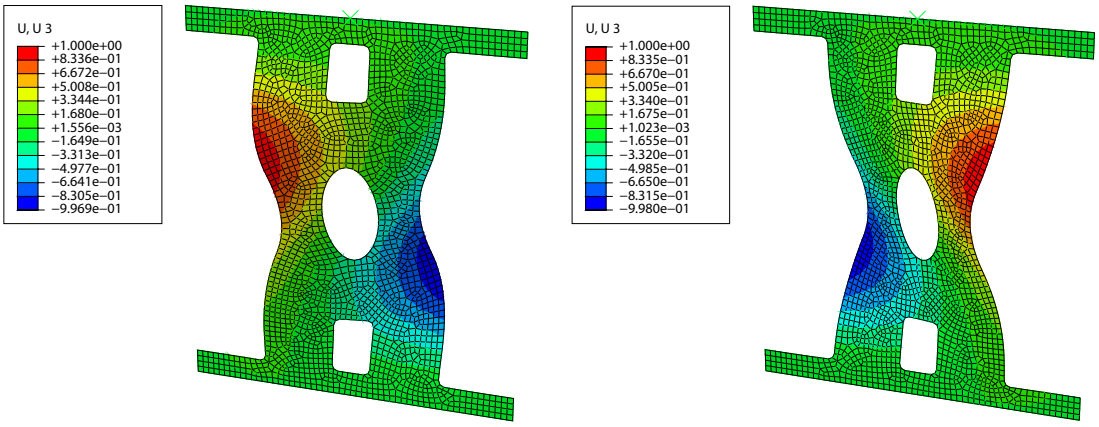

(a) Buckling Shape 1 - $V_B = 178\,kips$ (b) Buckling Shape 2 - $V_B = -178\,kips$

Figure D.5: Buckling shapes for Topology 0.40-0.30-1

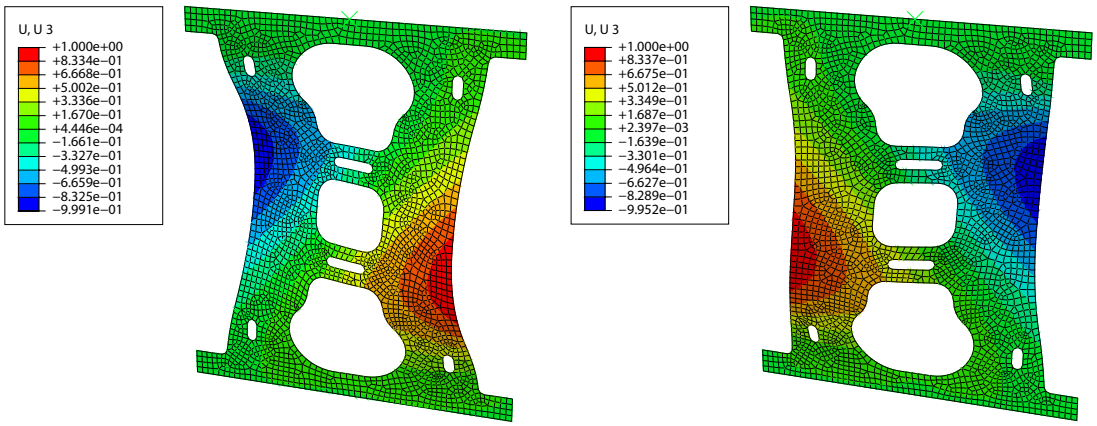

(a) Buckling Shape 1 - $V_B = 237\,kips$ (b) Buckling Shape 2 - $V_B = -237\,kips$

Figure D.6: Buckling shapes for Topology 0.50-0.10-2

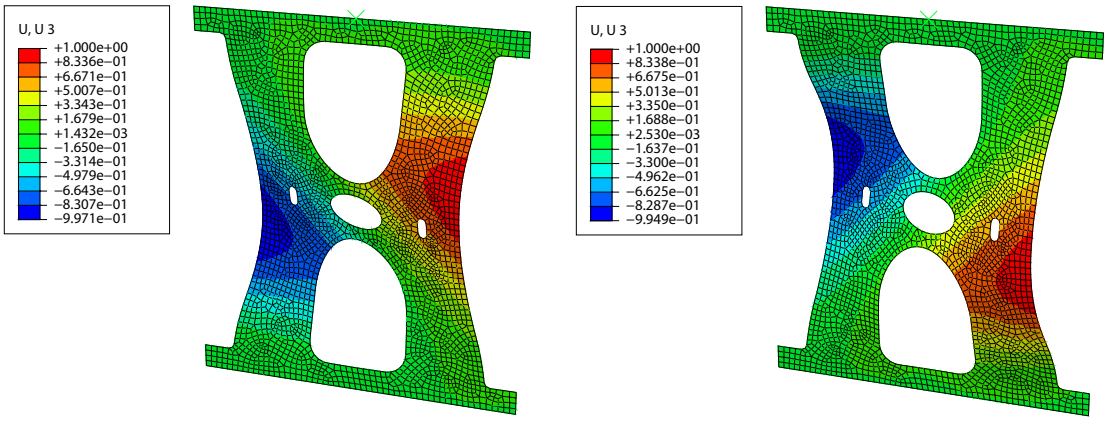

(a) Buckling Shape 1 - $V_B = 235\,kips$ (b) Buckling Shape 2 - $V_B = -235\,kips$

Figure D.7: Buckling shapes for Topology 0.50-0.20-1

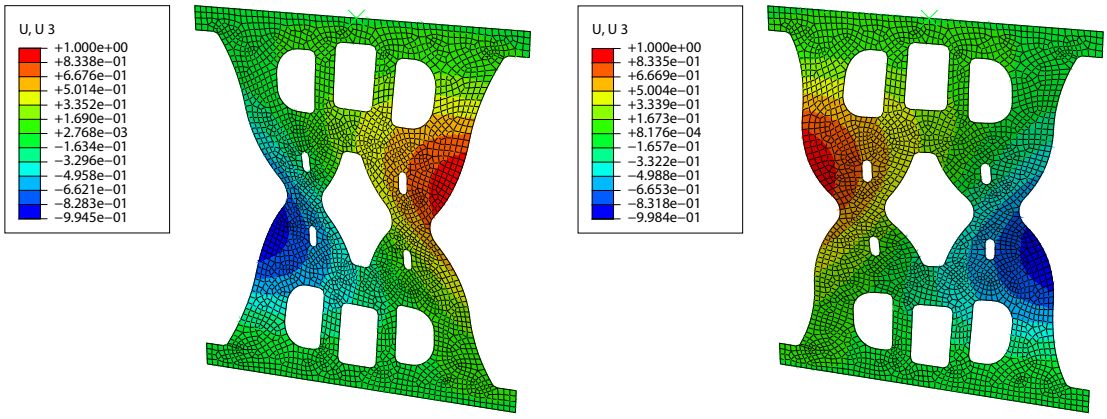

(a) Buckling Shape 1 - $V_B = 255\,kips$ (b) Buckling Shape 2 - $V_B = -255\,kips$

Figure D.8: Buckling shapes for Topology 0.50-0.30-1

D.2 Yielding Mechanisms

This yielding mechanisms for all the optimized topologies is represented as a contour plot of the von Mises stress. Those regions where the von Mises stress exceeds $F_Y = 50\ ksi$ are considered part of the yielding mechanism.

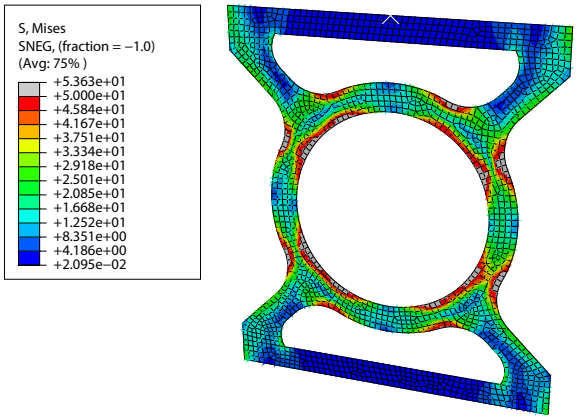

(a) Ring Shaped

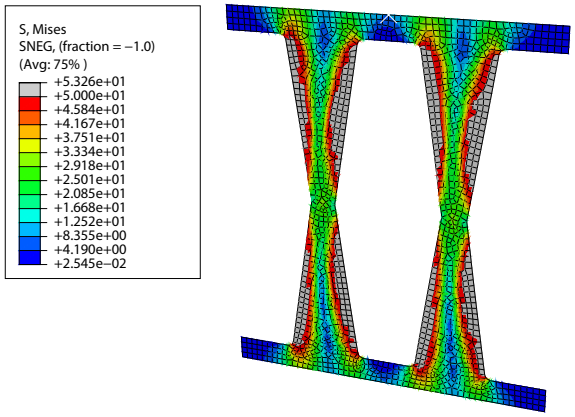

(b) Butterfly Shaped

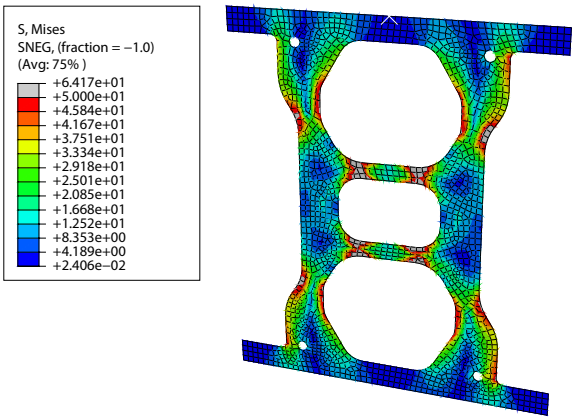

(c) 0.30-0.10-2

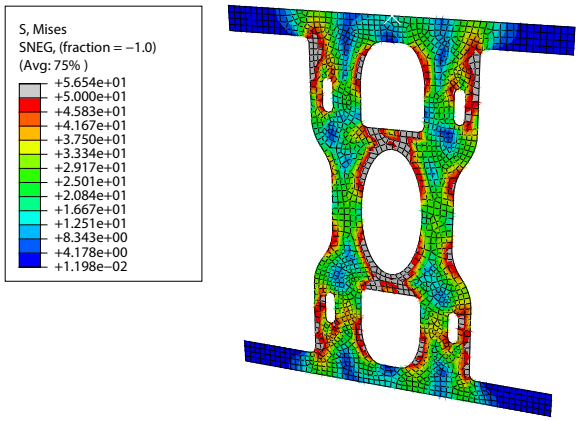

(d) 0.30-0.20-2

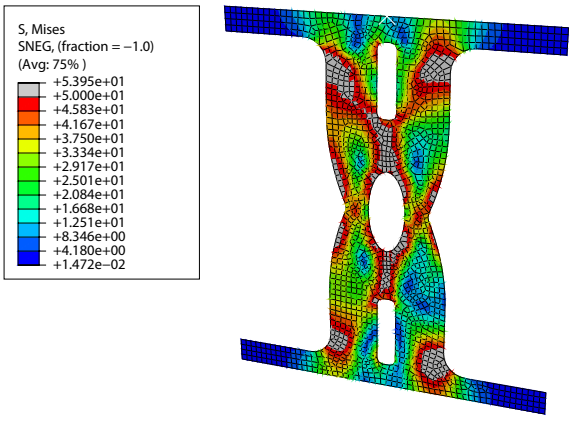

(e) 0.30-0.30-2

Figure D.9: Von Mises stresses at $\delta = \delta_Y$ for $\overline{Vol}(\mathbf{x}) = 0.30Vol$

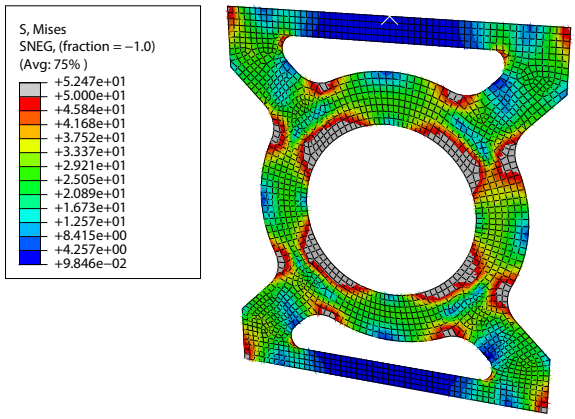

(a) Ring Shaped

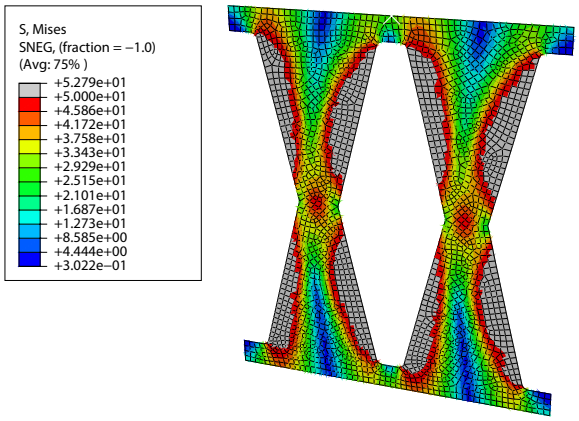

(b) Butterfly Shaped

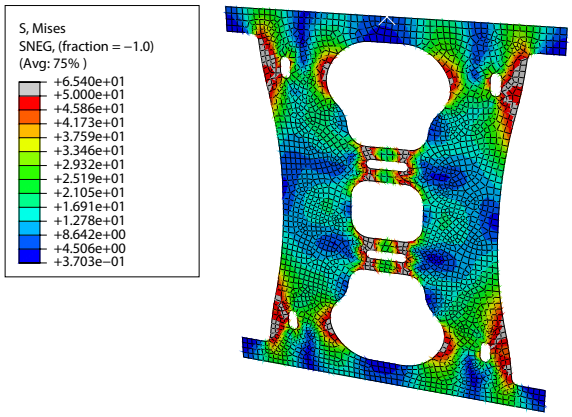

(c) 0.50-0.10-2

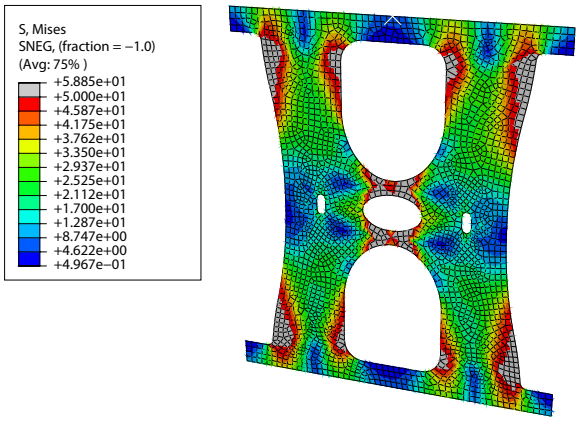

(d) 0.50-0.20-1

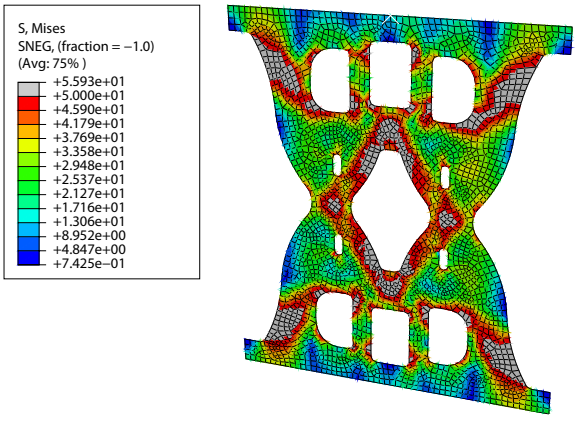

(e) 0.50-0.30-1

Figure D.10: Von Mises stresses at $\delta = \delta_Y$ for $\overline{Vol}(\mathbf{x}) = 0.50Vol$

D.3 Pushover curves

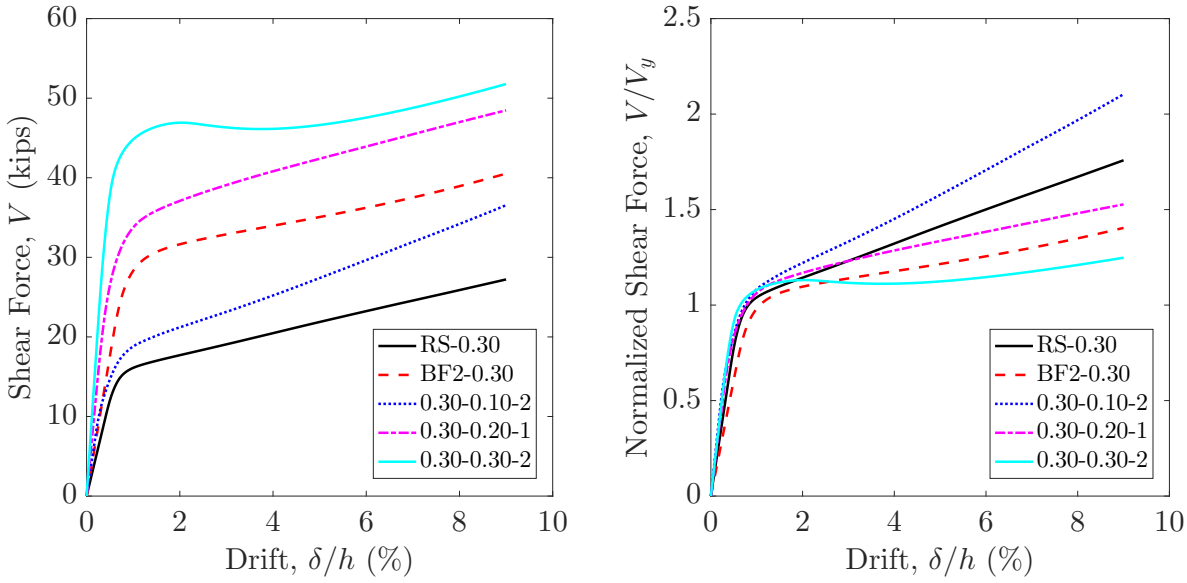

(a) Topology: ΔVol - $\overline{V_Y}/\overline{V_B}$ - Population

(b) Topology: ΔVol - $\overline{V_Y}/\overline{V_B}$ - Population

Figure D.11: Monotonic pushover analysis response for $\overline{Vol}(\mathbf{x}) = 0.30Vol$

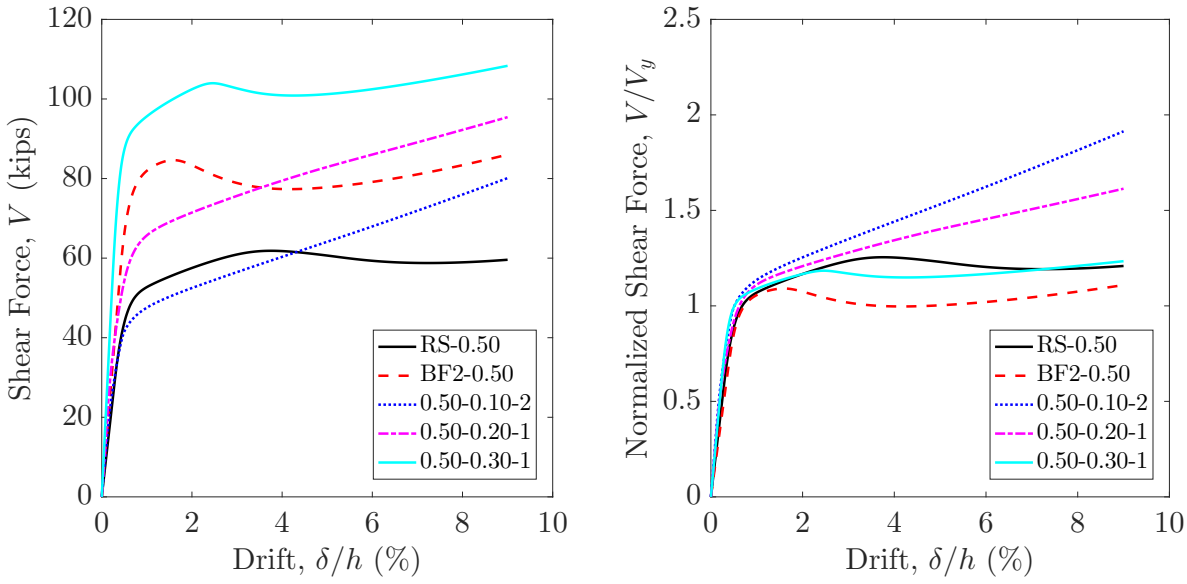

(a) Topology: ΔVol - $\overline{V_Y}/\overline{V_B}$ - Population

(b) Topology: ΔVol - $\overline{V_Y}/\overline{V_B}$ - Population

Figure D.12: Monotonic pushover analysis response for $\overline{Vol}(\mathbf{x}) = 0.50Vol$

D.4 Out of plane displacements

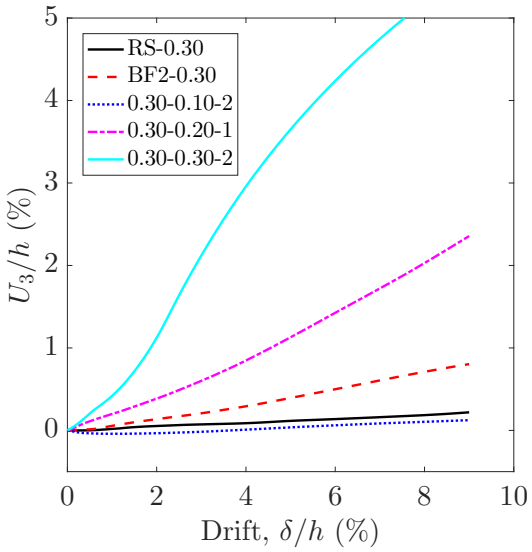

Figure D.13: Evolution of the U_3 displacement component - Topology: ΔVol - $\overline{V_Y}/\overline{V_B}$ - Population

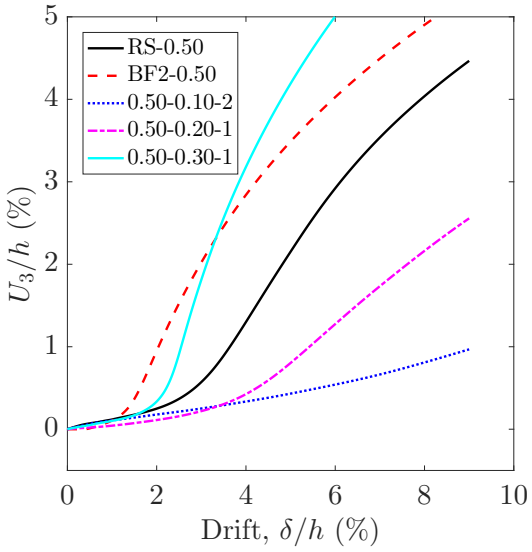

Figure D.14: Evolution of the U_3 displacement component - Topology: ΔVol - $\overline{V_Y}/\overline{V_B}$ - Population

Appendix E

Cyclic Analysis

In this appendix the results from the cyclic analysis such as: the hysteretic response, the backbones curves, the evolution of the dissipated energy, the equivalent viscous damping and the distribution of the equivalent plastic strains are summarized for those topologies with volume fraction different than $\overline{Vol}(\mathbf{x}) = 0.40Vol$.

E.1 Cyclic response

The cyclic response of the optimized topologies is presented in the following figures. The main observation from these set of cyclic responses is that the objective function bias plays an important role in the shape of the hysteresis loop, i.e. a greater value of $\overline{V_Y}/\overline{V_B}$ will induce a pinched hysteretic response in the optimized topology.

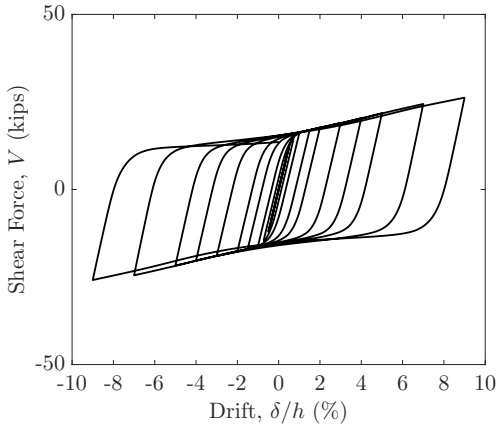

(a) Ring Shaped

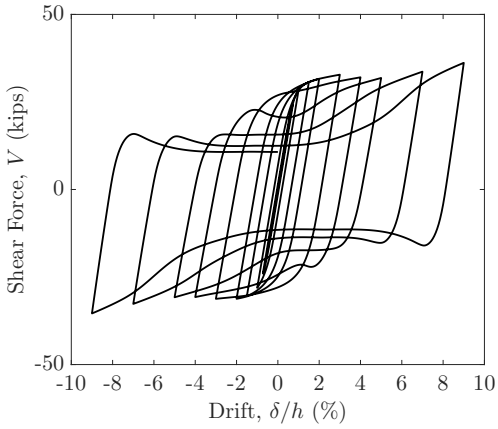

(b) Butterfly Shaped

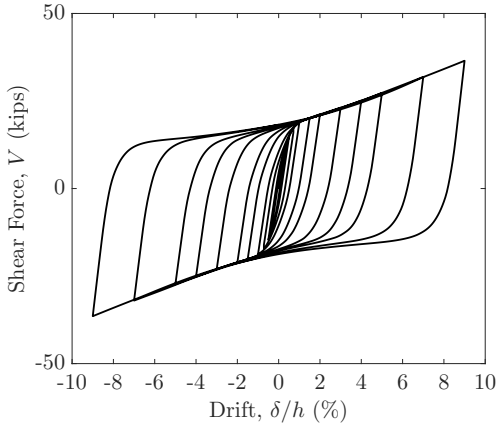

(c) 0.30-0.10-2

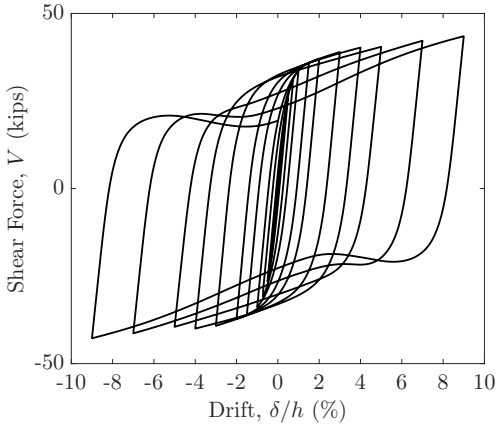

(d) 0.30-0.20-1

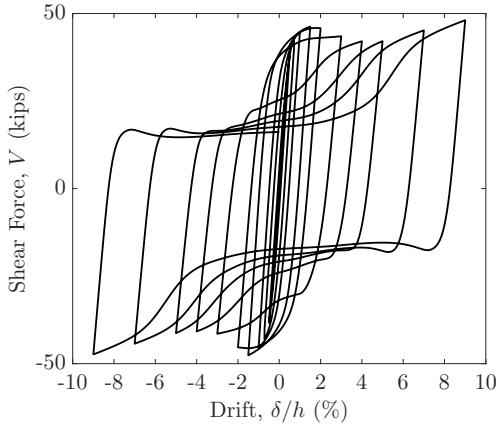

(e) 0.30-0.30-2

Figure E.1: Hysteretic behavior of the topologies with $\overline{Vol}(\mathbf{x}) = 0.30Vol$

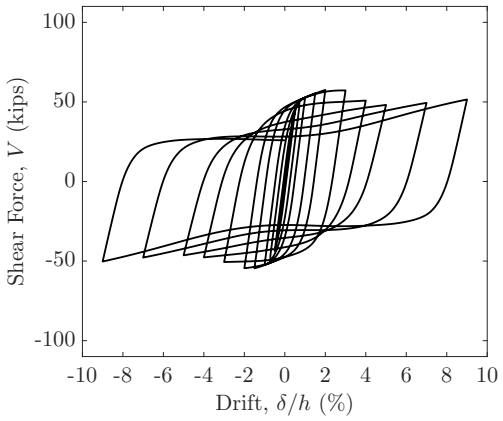

(a) Ring Shaped

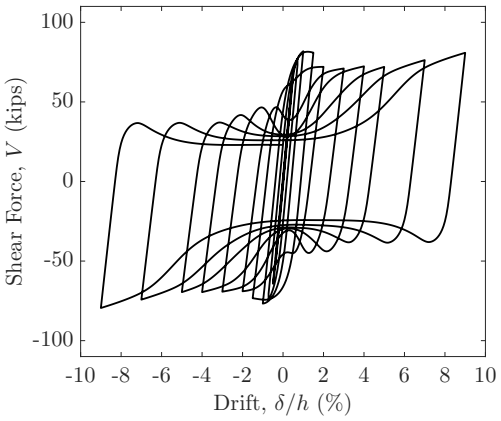

(b) Butterfly Shaped

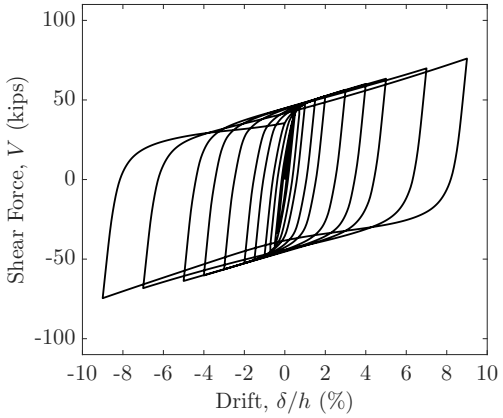

(c) 0.50-0.10-2

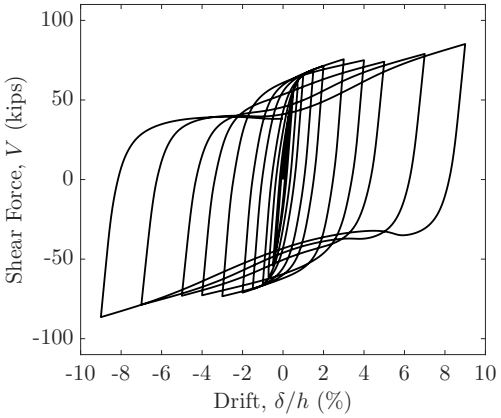

(d) 0.50-0.20-1

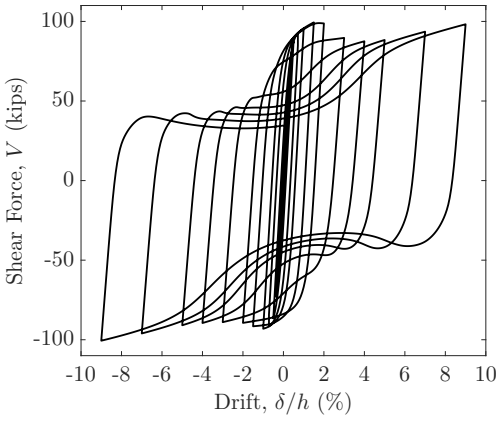

(e) 0.50-0.30-1

Figure E.2: Hysteretic behavior of the topologies with $\overline{Vol}(\mathbf{x}) = 0.50Vol$

E.2 Backbone curves

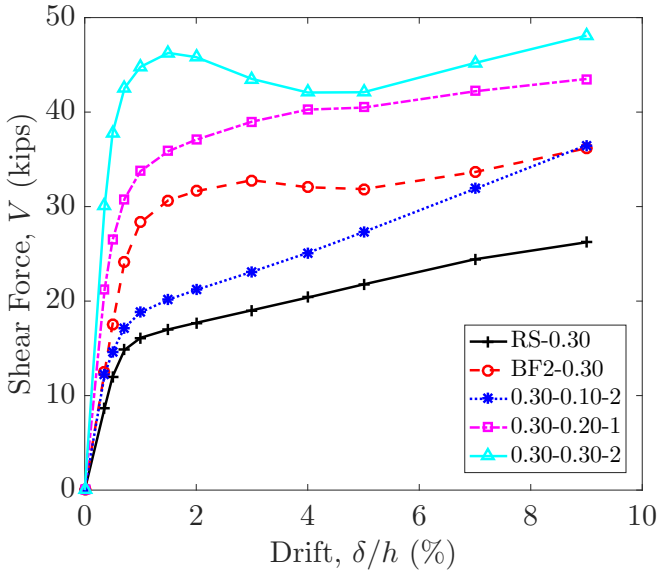

Figure E.3: Backbone curves - Topology: ΔVol - $\overline{V_Y}/\overline{V_B}$ - Population

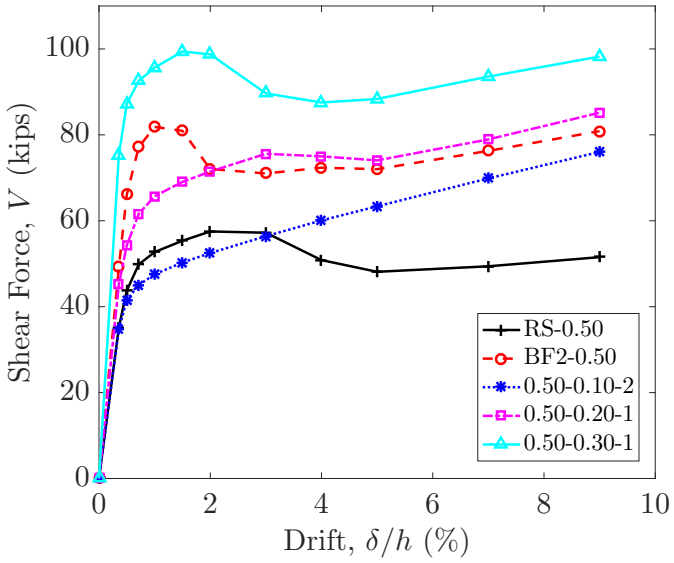

Figure E.4: Backbone curves - Topology: ΔVol - $\overline{V_Y}/\overline{V_B}$ - Population

E.3 Energy dissipation

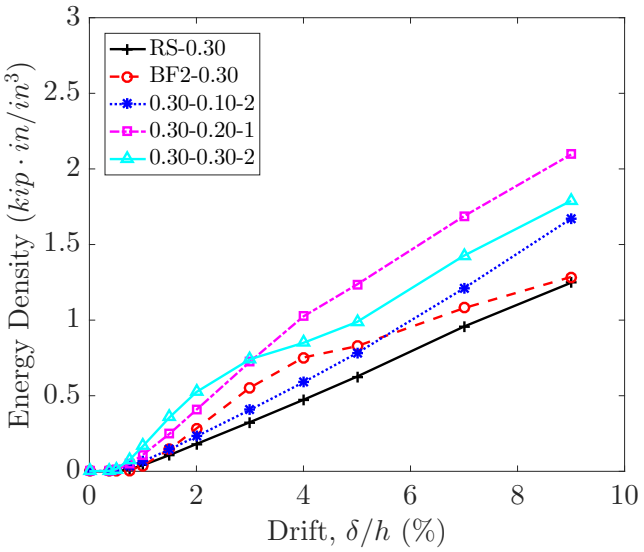

(a) Topology: ΔVol - $\overline{V_Y}/\overline{V_B}$ - Population

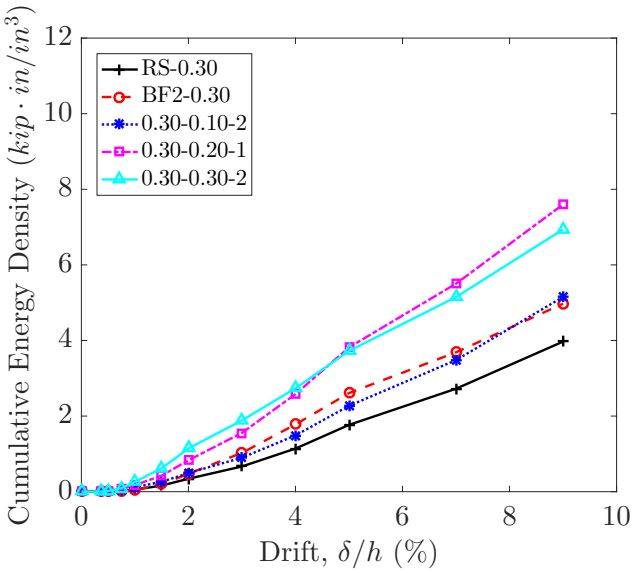

(b) Topology: ΔVol - $\overline{V_Y}/\overline{V_B}$ - Population

Figure E.5: Dissipated energy per unit volume for $\overline{Vol}(\mathbf{x}) = 0.30Vol$

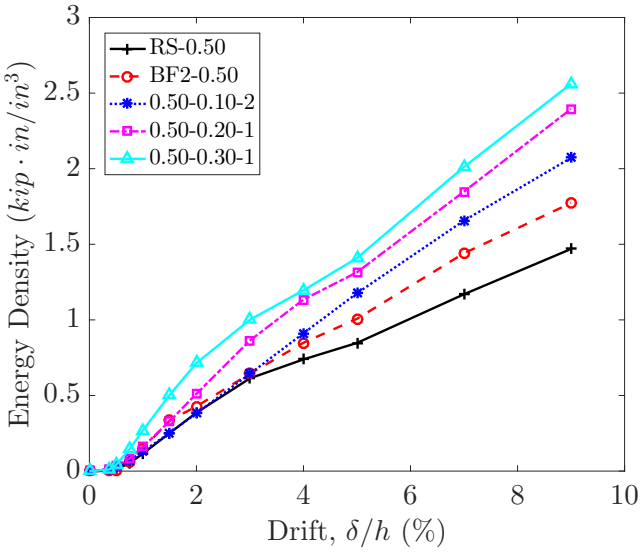

(a) Topology: ΔVol - $\overline{V_Y}/\overline{V_B}$ - Population

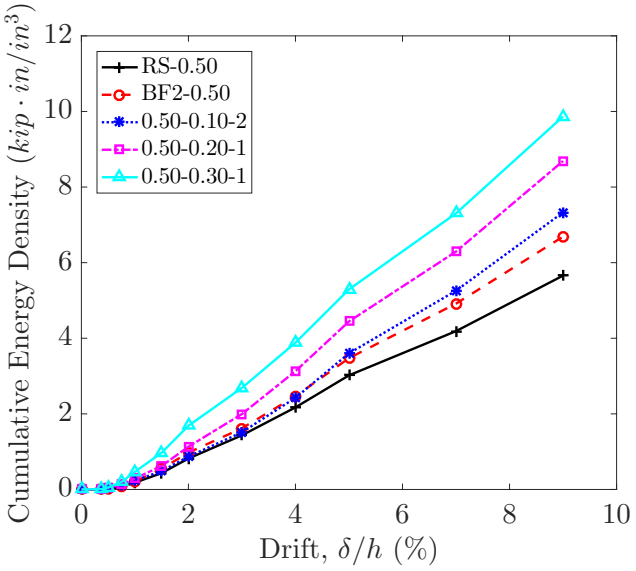

(b) Topology: ΔVol - $\overline{V_Y}/\overline{V_B}$ - Population

Figure E.6: Dissipated energy per unit volume for $\overline{Vol}(\mathbf{x}) = 0.50Vol$

E.4 Equivalent viscous damping

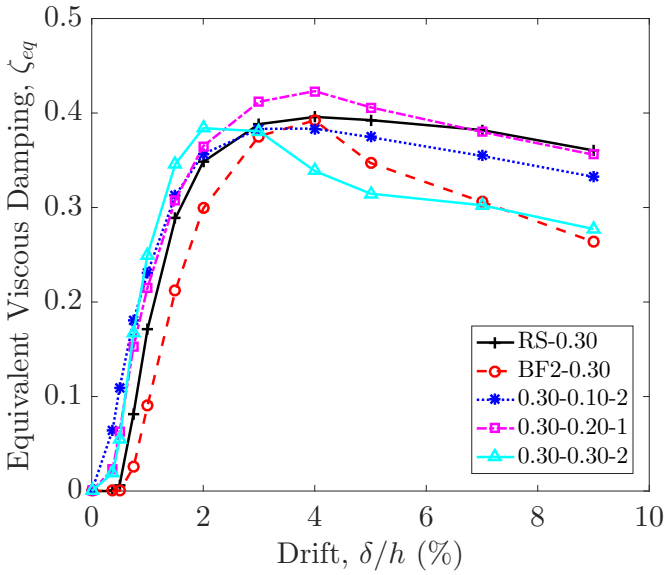

Figure E.7: Equivalent viscous damping - Topology: ΔVol - $\overline{V_Y}/\overline{V_B}$ - Population

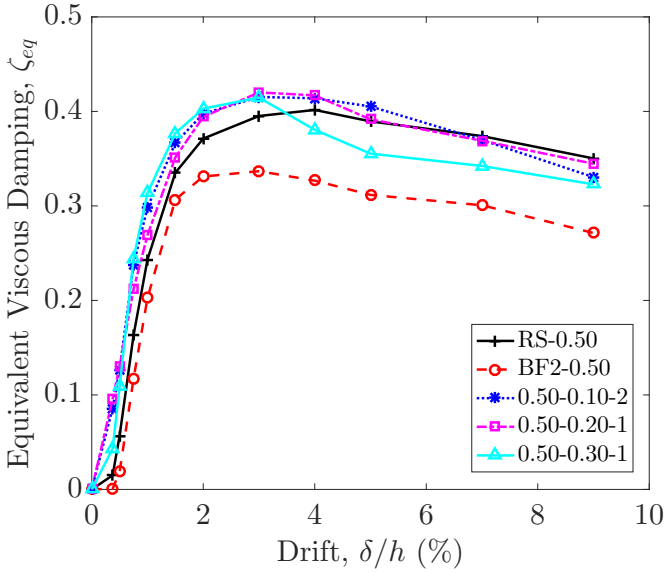

Figure E.8: Equivalent viscous damping - Topology: ΔVol - $\overline{V_Y}/\overline{V_B}$ - Population

E.5 Equivalent plastic strains

The following figures show the distribution of the equivalent plastic strains as a contour plot projected in the deformed topologies at the end of the cyclic analysis for all those shapes with a volume fraction different than $\overline{Vol}(\mathbf{x}) = 0.40Vol$.

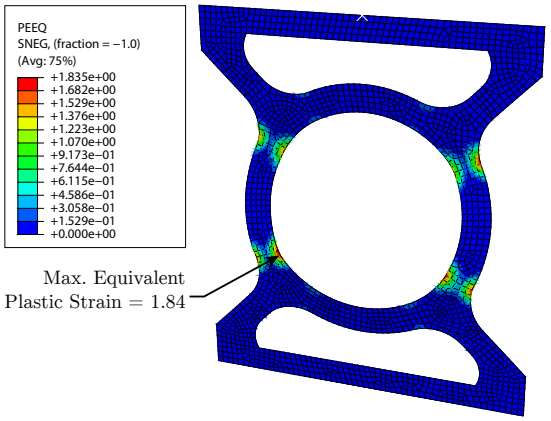

(a) Ring Shaped

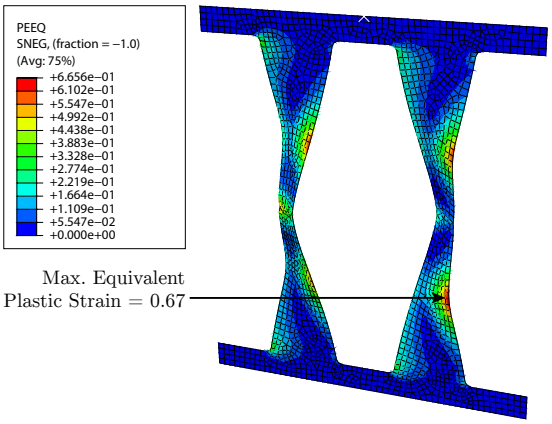

(b) Butterfly Shaped

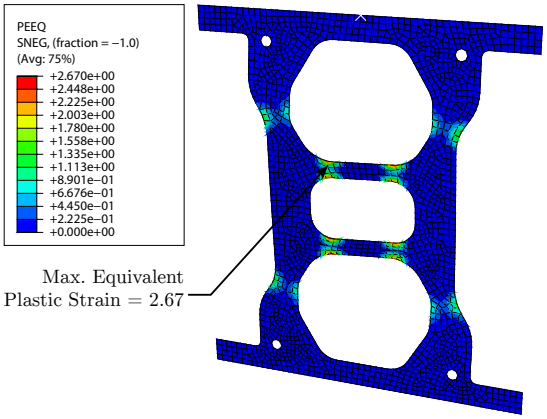

(c) 0.30-0.10-2

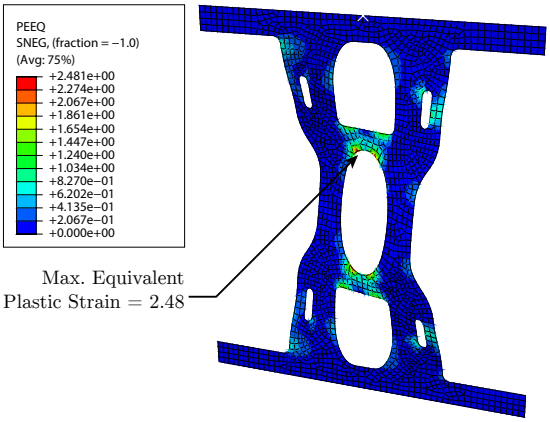

(d) 0.30-0.20-2

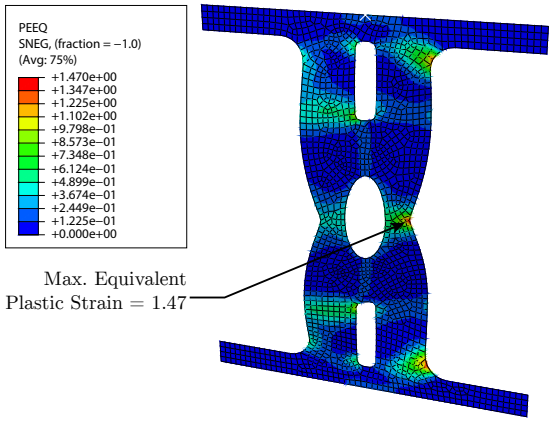

(e) 0.30-0.30-2

Figure E.9: Final distribution of the equivalent plastic strain for $\overline{Vol}(\mathbf{x}) = 0.30Vol$

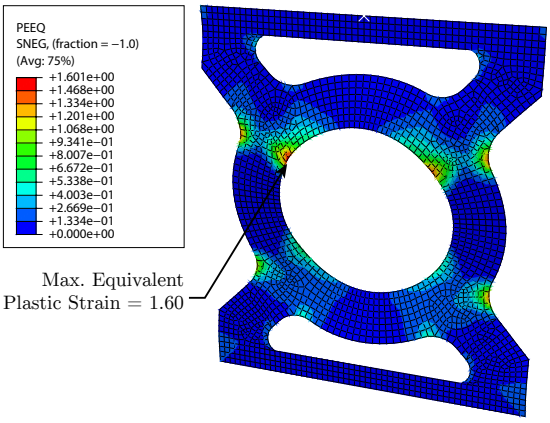

(a) Ring Shaped

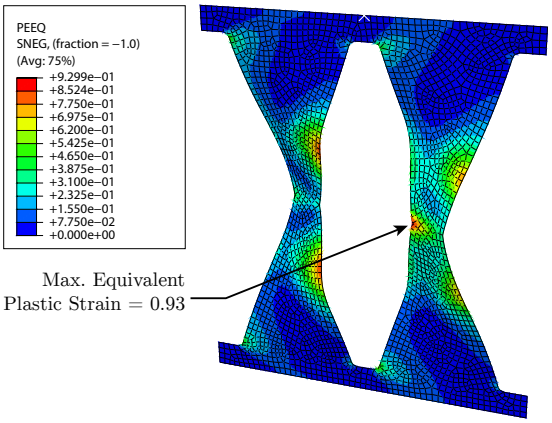

(b) Butterfly Shaped

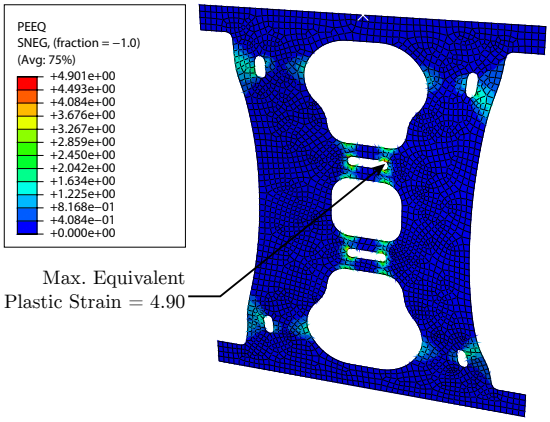

(c) 0.50-0.10-2

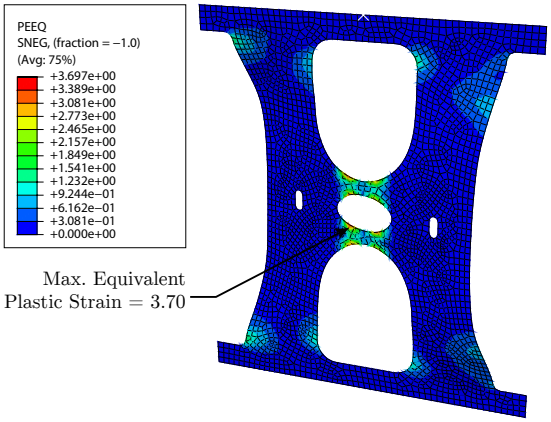

(d) 0.50-0.20-1

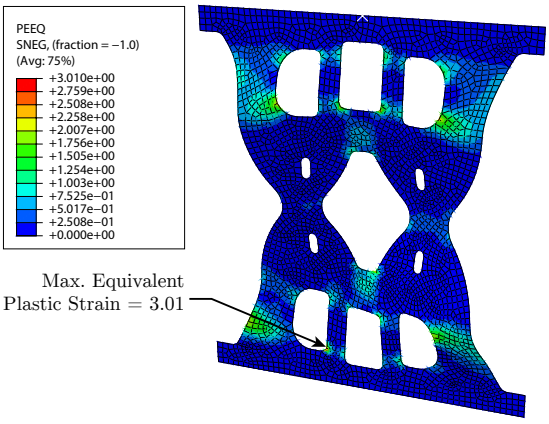

(e) 0.50-0.30-1

Figure E.10: Final distribution of the equivalent plastic strain for $\overline{Vol}(\mathbf{x}) = 0.50Vol$